

Enriching WLANs with Advanced Sensing and Networking Applications

By

YUNZE ZENG  
DISSERTATION

Submitted in partial satisfaction of the requirements for the degree of

DOCTOR OF PHILOSOPHY

in

Computer Science

in the

OFFICE OF GRADUATE STUDIES

of the

UNIVERSITY OF CALIFORNIA

DAVIS

Approved:

---

Prof. Prasant Mohapatra, Chair

---

Prof. S. Felix Wu

---

Prof. Xin Liu

Committee in Charge

2018

Copyright © 2018 by

Yunze Zeng

*All rights reserved.*

*Dedicated to my parents, for their unwavering and unconditional support.*

## CONTENTS

List of Figures . . . . .	viii
List of Tables . . . . .	xii
Abstract . . . . .	xiii
<b>1 Introduction</b>	<b>1</b>
1.1 Research Scope and Overview . . . . .	1
1.2 Main Approaches and Methodology . . . . .	2
1.3 Outline . . . . .	6
<b>2 Understanding the Latest WLANs: Performance Characterization of 802.11ac Networks</b>	<b>7</b>
2.1 Introduction . . . . .	7
2.2 Overview of 802.11ac and Experiment Setup . . . . .	9
2.2.1 What is new in 802.11ac? . . . . .	9
2.2.2 Experiment Setup . . . . .	11
2.3 Performance Characterization . . . . .	12
2.3.1 Performance of an Isolated 802.11ac Link . . . . .	13
2.3.2 Characteristics of (MCS x SS) . . . . .	13
2.3.3 Performance Characterization in Indoor Environment . . . . .	15
2.4 Energy Efficiency of 802.11ac . . . . .	16
2.4.1 Idle Listening - A Dominant Factor . . . . .	16
2.4.2 Impact of Rate & Channel Width Adaptation: . . . . .	19
2.4.3 Channel Width vs. Spatial Streams . . . . .	21
2.5 Interference Characterization . . . . .	22
2.5.1 Throughput Anomalies with Heterogeneous Channel Widths . . . . .	23
2.5.2 802.11ac Channel Access Procedure . . . . .	24
2.5.3 CCA Thresholds . . . . .	26
2.6 Dynamic Channel Width Access . . . . .	28
2.6.1 Enhanced RTS/CTS Protocol . . . . .	28
2.6.2 Sharing or Dividing 80 MHz . . . . .	29
2.6.3 80 MHz Channel Interference Pattern . . . . .	30
2.7 Related Work . . . . .	31

2.8	Summary . . . . .	32
<b>3</b>	<b>Understanding Sensing Methodology: Energy Expenditure Estimation with Wearable Sensors</b>	<b>33</b>
3.1	Introduction . . . . .	33
3.2	Related Work . . . . .	36
3.2.1	EEE Using Body Sensors . . . . .	36
3.2.2	EEE Using Smartphones . . . . .	36
3.2.3	Barometer Sensor and Its Application . . . . .	36
3.3	Methodology . . . . .	37
3.3.1	Logistics . . . . .	37
3.3.2	Basic Features . . . . .	37
3.3.3	Derived Features . . . . .	38
3.3.4	Calorimetry equations . . . . .	39
3.3.5	Instruments . . . . .	39
3.4	Prediction Models . . . . .	39
3.4.1	Linear Regression . . . . .	40
3.4.2	Artificial Neural Networks . . . . .	40
3.5	Experiments and Results . . . . .	41
3.5.1	Impact of Calorimetry equations . . . . .	43
3.5.2	Impact of barometer sensor . . . . .	43
3.5.3	Influence of Feature Vectors . . . . .	43
3.5.4	Comparison with other products . . . . .	44
3.6	Summary and Future Work . . . . .	45
<b>4</b>	<b>Enabling Sensing Application through 2.4/5 GHz-based WLANs</b>	<b>47</b>
4.1	Fine-grained Device Motion Recognition through WiFi Signals . . . . .	47
4.1.1	Introduction . . . . .	47
4.1.2	Related Work . . . . .	48
4.1.3	CSI and Motion . . . . .	49
4.1.4	APsense . . . . .	53
4.1.5	Discussion and Conclusions . . . . .	57

4.2	Analyzing Shopper's Behavior through WiFi Signals . . . . .	57
4.2.1	Introduction . . . . .	57
4.2.2	Motivation . . . . .	59
4.2.3	Understanding Shopper's Behavior . . . . .	60
4.2.4	Analyzing Shopper's Behavior Using CSI . . . . .	62
4.2.5	Related Work . . . . .	66
4.2.6	Potential and Limitations . . . . .	67
4.2.7	Summary . . . . .	67
<b>5</b>	<b>Enriching WLANs with Device-free WiFi-based Person Identification System in Smart Spaces</b>	<b>69</b>
5.1	Introduction . . . . .	69
5.2	Related Work . . . . .	72
5.3	Overview of WiWho . . . . .	73
5.3.1	Usage Scenarios and Design Goals . . . . .	73
5.3.2	Central Idea and Challenges . . . . .	74
5.3.3	System Overview . . . . .	75
5.4	Measurement based Feasibility Study . . . . .	76
5.4.1	Detecting Gait from CSI . . . . .	76
5.4.2	Difference in CSI-based Gait for Two People . . . . .	78
5.4.3	Consistency of CSI-based Gait over Time . . . . .	78
5.5	CSI Preprocessing and Walking Detection . . . . .	79
5.5.1	CSI Preprocessing . . . . .	79
5.5.2	Walking Detection . . . . .	80
5.6	Person Identification using CSI-based Gait . . . . .	82
5.6.1	Constructing CSI Features . . . . .	83
5.6.2	Analyzing Person's Steps . . . . .	83
5.6.3	Analyzing Person's Walk . . . . .	85
5.6.4	Person Identification using CSI-based Gait . . . . .	86
5.7	Performance Evaluation . . . . .	87
5.7.1	Implementation and Experiments . . . . .	87
5.7.2	Walking Detection Validation . . . . .	89

5.7.3	Person Identification with Different Group sizes . . . . .	90
5.7.4	Step Analysis vs. Walk Analysis . . . . .	91
5.7.5	Robustness with Different Walking Lengths . . . . .	92
5.8	Discussion and Limitations . . . . .	93
5.9	Summary . . . . .	94
<b>6</b>	<b>Enriching WLANs with MU-MIMO-aware AP Selection System</b>	<b>95</b>
6.1	Introduction . . . . .	95
6.2	Background . . . . .	98
6.2.1	IEEE 802.11ac Background . . . . .	98
6.2.2	Enterprise Wi-Fi Networks . . . . .	98
6.3	A Measurement Study . . . . .	99
6.3.1	Platform and Methodology . . . . .	99
6.3.2	Correlated Wireless Channels . . . . .	99
6.3.3	Heterogeneous Bandwidth Clients . . . . .	101
6.3.4	Load Balancing . . . . .	102
6.4	Design . . . . .	103
6.4.1	MU-MIMO Performance Inference . . . . .	103
6.4.2	Client and AP Profiling . . . . .	107
6.4.3	AP Selection Model . . . . .	109
6.4.4	Discussion . . . . .	112
6.5	Implementation . . . . .	112
6.6	Evaluation . . . . .	112
6.6.1	Performance in Representative Settings . . . . .	113
6.6.2	Larger Scale Field Trials . . . . .	116
6.6.3	Trace Driven Simulations . . . . .	117
6.7	Related Work . . . . .	118
6.8	Summary . . . . .	119
<b>7</b>	<b>Enabling Sensing Application through 60 GHz-based WLANs</b>	<b>121</b>
7.1	Introduction . . . . .	121
7.2	Related Work . . . . .	123

7.3	System Design . . . . .	125
7.3.1	60GHz Communication Platform . . . . .	125
7.3.2	System Overview . . . . .	126
7.4	60 GHz-based Human Finding and Activity Analysis . . . . .	126
7.4.1	Activity Analysis . . . . .	130
7.5	60GHz-based Vital Signs Monitoring . . . . .	132
7.5.1	Breathing and Heart Rates . . . . .	132
7.5.2	Impact of Incident Angle . . . . .	133
7.6	Evaluation . . . . .	136
7.6.1	Reflection Loss based Human Finding . . . . .	136
7.6.2	Accuracy of Vital Sign Monitoring . . . . .	137
7.7	Summary . . . . .	140
<b>8</b>	<b>Conclusions</b>	<b>141</b>

## LIST OF FIGURES

1.1	Research Scope . . . . .	3
2.1	FCC 5GHz unlicensed band channel map. There are 25 20 MHz bands, 12 40 MHz bands, 6 80 MHz bands and 2 160 MHz bands in this band. . . . .	9
2.2	802.11ac MCS index table. The table is simplified to have only 10 values and the spacial streams information is not indicated in this table. . . . .	10
2.3	Testbed of 18 802.11ac nodes used for the experiments. We use this 18 nodes to do the experiments for the indoor characterization only. The outdoor measurement, energy efficiency and interference cases are not included in this figure. . . . .	11
2.4	Throughput comparison between 802.11ac and 802.11n . . . . .	12
2.5	Throughput with different MCS values when SS = 3 . . . . .	13
2.6	Maximum throughput when SS = 1, 2 or 3 (MCS value labeled on top of each bar) . . .	14
2.7	The aggregate throughput for each AP using 80 MHz and 40 MHz channel widths . . .	15
2.8	Power consumption samples with idle to active threshold line for different channel widths. The power measurement sampling rate is 50Hz. . . . .	17
2.9	Comparison of dynamic power consumption between different channel widths (with 1 Mbps receiving rate constantly) on smartphone . . . . .	18
2.10	Power consumption of the most energy efficient setting in different channel widths at different source rates . . . . .	19
2.11	Comparison of per megabit energy cost between different channel widths . . . .	20
2.12	Comparison of percentage increase in power consumption with increasing SS or increasing channel width . . . . .	21
2.13	Indoor setup of 2 links and a sniffer . . . . .	22
2.14	Link 1 is operating in 80 MHz fixed channel width and Link 2 is operating on 40/20 MHz width. When Link 2's primary channel is the same as that of Link 1, both link share the medium proportionally (Case 1 or Case 5). On the other hand, when Link 2's primary channel falls within secondary channels of Link 1, severe degradation of throughput is observed for Link 1. . . . .	23
2.15	Different physical carrier sensing time and CCA methods in primary channel and secondary channels cause the 80 MHz link to continuously back off . . . . .	26

2.16 E-RTS/CTS protocol . . . . .	27
2.17 RTS-CTS packets captured by sniffer . . . . .	29
2.18 Throughput comparison of 4 cases where two links (Case-1): share 80MHz with same primary channel, (Case-2): share 80MHz with different primary channel, (Case-3): divide 80 MHz into adjacent 40MHz channels, (Case-4): divide 80 MHz into non-adjacent 40MHz channels . . . . .	30
2.19 Two 802.11ac links - comparison of interference pattern between two cases, case 1 when both links operate on 80 MHz and case 2 when both links operate on 40 MHz. . . . .	31
3.1 Plot of EEE using ANN and Linear Regression with actual EE values for one individual using raw accelerometer output . . . . .	41
3.2 Plot of EEE using ANN and Linear Regression with actual EE values for one individual using all FVs . . . . .	42
3.3 Overall absolute EE comparison of COSMED and ANN with Nike+, Fitbit and Calorimetry equation . . . . .	46
4.1 Different type of hand motions studied in APsense . . . . .	50
4.2 Density Distribution of CSI amplitude in each subcarrier for a 30s trace where client is different motions. The x axis is the subcarrier index from 1 to 30 and the y axis is the CSI amplitude. . . . .	51
4.3 Comparison between different CSI features for different types of motions . . . . .	52
4.4 APsense Architecture . . . . .	54
4.5 TP Rate comparison with different time window sizes . . . . .	56
4.6 Correlation between sensor and CSI features . . . . .	57
4.7 Shopper's states transition diagram . . . . .	59
4.8 Experiment layout . . . . .	61
4.9 CSI profiles when a shopper performs different activities . . . . .	62
4.10 Performance around the entrance (W is "walk" and S is "stand") (In the confusion matrix: A is "walk outside", B is "walk at entrance", C is "walk inside", D is "stand at entrance" and E is "no person") . . . . .	65
4.11 Performance inside the store (in the confusion matrix: A is "walk fast", B is "walk slowly", C is "stand" and D is "no person") . . . . .	66

5.1	System architecture of WiWho . . . . .	75
5.2	Comparison between CSI Amplitude and on-body accelerometer readings while a person is walking . . . . .	76
5.3	Comparison between the CSI-based gait of 2 people . . . . .	77
5.4	Comparing CSI-based gait for different people over time . . . . .	78
5.5	Channel impulse response showing distant multipath . . . . .	79
5.6	Comparison of FFT energy in a 6s window between different activities . . . . .	81
5.7	Comparison of FFT coefficients for different activities . . . . .	82
5.8	Selected features for step and walk analysis . . . . .	85
5.9	Experiment layouts and device setup . . . . .	87
5.10	TP rate and FP rate of walking detection . . . . .	88
5.11	The confusion matrix of walk detection with 0.6 second detection time. W is walking, S is sitting, T is standing and N is without person . . . . .	89
5.12	The accuracy and FP rate for person in identification with different group sizes . . . . .	90
5.13	The confusion matrix of person identification with 6 people . . . . .	91
5.14	The performance with different feature calculation methods and different group size at different locations . . . . .	92
5.15	The accuracy of identification for different group sizes with different walking lengths . . . . .	93
6.1	Client association in enterprise Wi-Fi. . . . .	96
6.2	Network topology for the case study setting. . . . .	99
6.3	a) V correlation, b, c) Packet-Error-Rate, d) throughput for clients in our case study settings. . . . .	100
6.4	MAPS architecture. . . . .	104
6.5	MAPS' CSI profiling. . . . .	105
6.6	Signal spatial distribution for stable and dynamic channels. . . . .	108
6.7	MAPS and DenseAP performance in representative settings. MAPS performs similar to Oracle. . . . .	113
6.8	Throughput and fairness comparison of MAPS, Oracle and DenseAP. . . . .	115
7.1	60 GHz transmitter and receiver system setup . . . . .	124
7.2	60 GHz transmitter and receiver system setup . . . . .	125

7.3	Reflection loss for different types of objects . . . . .	127
7.4	Reflection profile of a room . . . . .	128
7.5	The experiment layout and human finding analysis . . . . .	130
7.6	RSS profile for walking activity analysis . . . . .	131
7.7	Raw RSS of the reflected signal and extracted breathing and heart beats . . . . .	132
7.8	Experiment setup of evaluating different incident angles . . . . .	133
7.9	Impact of incident angle . . . . .	134
7.10	Experiment setup in office and home . . . . .	135
7.11	Accuracy of object/human classification with varying dwell time (number of RSS samples)	136
7.12	Accuracy of breathing rate and heart rate of 7 participants at three different incident angles	138
7.13	Impact of distance apart and robustness to different postures . . . . .	138

## LIST OF TABLES

2.1 Throughput (Mbps) of a link when channel width = 80MHz, MCS = 6, 7, 8 or 9, and SS = 1 . . . . .	14
2.2 Throughput (Mbps) comparison between 802.11ac at 80 MHz and 802.11n at 40 MHz in indoor environment . . . . .	15
2.3 Throughput (Mbps) of different clients when multiple APs simultaneously transmit . . . . .	16
2.4 Detailed power consumption of QCA9880 when operating on different channel widths . . . . .	17
2.5 CCA Thresholds(dBm) . . . . .	26
3.1 EEE (Cal) and step counts using commercial devices (Nike+ Fuelband and Fitbit one) . . . . .	34
3.2 Regression Results . . . . .	40
3.3 Impact of Calorimetry Equation (CE) on ANN performance . . . . .	42
3.4 Impact of barometer values on EEE prediction using ANN . . . . .	43
3.5 Relative Computational Time of FV extraction step (relative to accelerometer data) . . . . .	44
3.6 Understanding trade-off between computational requirements and accuracy for EEE using ANN . . . . .	45
4.1 APsense Motion Recognition Results at Different Locations - TP Rate . . . . .	55
4.2 Detailed Analysis for Combined Locations Case . . . . .	56
4.3 Shopper's behavior around the entrance . . . . .	60
4.4 Shopper's behavior inside the store . . . . .	60
5.1 Time window features . . . . .	84
5.2 Characteristics of 6 volunteers . . . . .	91
6.1 Per-client and aggregate (across APs) downlink UDP throughput (Mbps), when C3 connects to AP1, AP2. . . . .	101
6.2 Per-client and aggregate downlink UDP throughput (Mbps) and fairness, for heterogeneous width clients. . . . .	102
6.3 CSI correlation for case study setting. . . . .	114
6.4 Average throughput for varying number of clients. . . . .	118

## ABSTRACT

### **Enriching WLANs with Advanced Sensing and Networking Applications**

The increasing popularity of WLANs has brought connectivity to every aspect of our modern life. The richness of wireless signals provides us with the high performance of Internet access. However, current functionality supported by WLANs is only limited to give us Internet access. With the massive deployment of wireless access points and other networking infrastructures, we need to seek new ways to enable more intelligent services and applications to enrich the functionality of existing WLANs. This thesis is focusing on how to reuse current WLANs infrastructure to build novel sensing and advanced networking applications. Inspired by various wearable sensing platforms, we bring the context and human activity sensing capability to WLANs by enabling sensing through RF signals. We leverage fine-grained wireless signal information and use machine learning techniques to enrich the functionality of traditional WLANs.

In this thesis, we present different ways to enrich WLANs. We start with a performance characterization of the latest WLANs to identify the problem and motivate our work. We then introduce the sensing methodology using the application we developed for wearable platforms. We bring sensing capability to WLANs by building a fine-grained device motion recognition application. Furthermore, we extend the scope to analyze human behavior in a shopping mall purely based on WiFi signals. We solve a fundamental problem of person identification in a device-free manner using WiFi signals. We also enrich WLANs with smart networking applications by designing an MU-MIMO-aware access point selection system. In the end, we move to the future WLANs with 60 GHz, and develop human sensing, activity monitoring and vital signs monitoring applications using 60 GHz WLANs.

# **Chapter 1**

## **Introduction**

### **1.1 Research Scope and Overview**

With the rapid development of wireless technologies and mobile computing abilities, modern Wireless Local Area Networks (WLANs) and mobile computing platforms (e.g., smartphone and wearables) are seeking new opportunities to enrich their functionality beyond the traditional ways. With next-generation WLANs(e.g., IEEE 802.11ac and 802.11ad), the throughput of wireless transmission can achieve as high as 1.3 Gbps and 7 Gbps while operating in 5 GHz and 60 GHz frequency bands respectively. Previous research has been focusing on increasing the network throughput and reducing the latency. With great success in recent research, current WLANs can satisfy most of mobile/laptop applications, and the major bottleneck of current home/office network performance comes from the Internet service provider instead of WLANs. In order to provide ubiquitous and gigabit wireless connectivity, major Access Point (AP) vendors provide high-density network deployment, where a large number of APs potentially supporting more clients operate in the same Radio Frequency (RF) coverage zone. With the massive deployment of APs and other infrastructure, more intelligent services and applications are needed to enrich the functionality of current WLANs. However, we are facing many new challenges in leveraging the existing wireless infrastructure to provide advanced services and applications. Substantial progress in WiFi-based indoor localization has proven that pervasiveness of WiFi can be exploited beyond its traditional use of Internet access to enable a variety of sensing applications. This sensing capability can fundamentally change the way we design WLANs based solutions and further add a new dimension to WLANs services and applications. Along this way, we are treating WLANs as a novel sensing platform which uses RF signal as a "sensor" to detect and sense the environment as well as human activities.

Meanwhile, in recent years, we have witnessed a remarkable proliferation of intelligent mobile wire-

less devices such as smartphones and wearable devices. Recent advancements in hardware technology have shown that it is possible to embed a variety of sensors (e.g., accelerometer, barometer) on small wearable devices (e.g., smartwatch). Building on top of these wearable devices, many personalization and customization applications can be developed to sense user context and provide rich services. Inspired by the way wearable devices utilize and analyze various sensor data in order to build intelligent wearable applications, we pursue a similar way to treat RF signal data in WLANs. Both WLANs and wearables can be regarded as different sensing platforms, and they are mutually interdependent. The WLAN-based approach enables the ability to sense from the infrastructure and environment. However, the wearable-based approach is to sense the context from the user side. Leveraging different sensing techniques and analytical methods, the research works presented in this thesis focus on how to enrich the functionality of WLANs beyond their traditional usage.

Starting from the characterization of next-generation WLANs, we have identified the issues remaining from the network perspective which further motivate our goal of enriching functionality beyond Internet access. Inspired by the sensing applications (e.g., energy expenditure estimation using body sensors) we developed for wearable platforms, we bring the sensing capability to the wireless APs and develop several convenient RF sensing applications on commodity WiFi APs. Then, we use concrete examples to illustrate the novel applications we build on top of existing WLANs from advanced sensing and networking perspectives. We further enable millimeter wave (e.g., 60 GHz WLANs) sensing and develop applications for the next-generation WLANs.

## 1.2 Main Approaches and Methodology

The research scope of this thesis can be concluded in Fig. 1.1, in which the green boxes are the works which are included in the thesis and the red boxes are not. This thesis will cover detailed steps, approaches, and methodology to achieve the goal of enriching the functionality of WLANs. The major contributions are as follows,

- **Understanding the latest WLANs: performance characterization of 802.11ac networks**

In order to better understand state-of-the-art WLANs, we present a detailed characterization of IEEE 802.11ac using real experiments. 802.11ac is the latest WLAN standard that is rapidly being adopted due to its potential to deliver very high throughput. The throughput increase in 802.11ac can be attributed to three factors - larger channel width (80/160 MHz), support for denser modulation (256 QAM) and increased number of spatial streams for MIMO. We provide an experimental

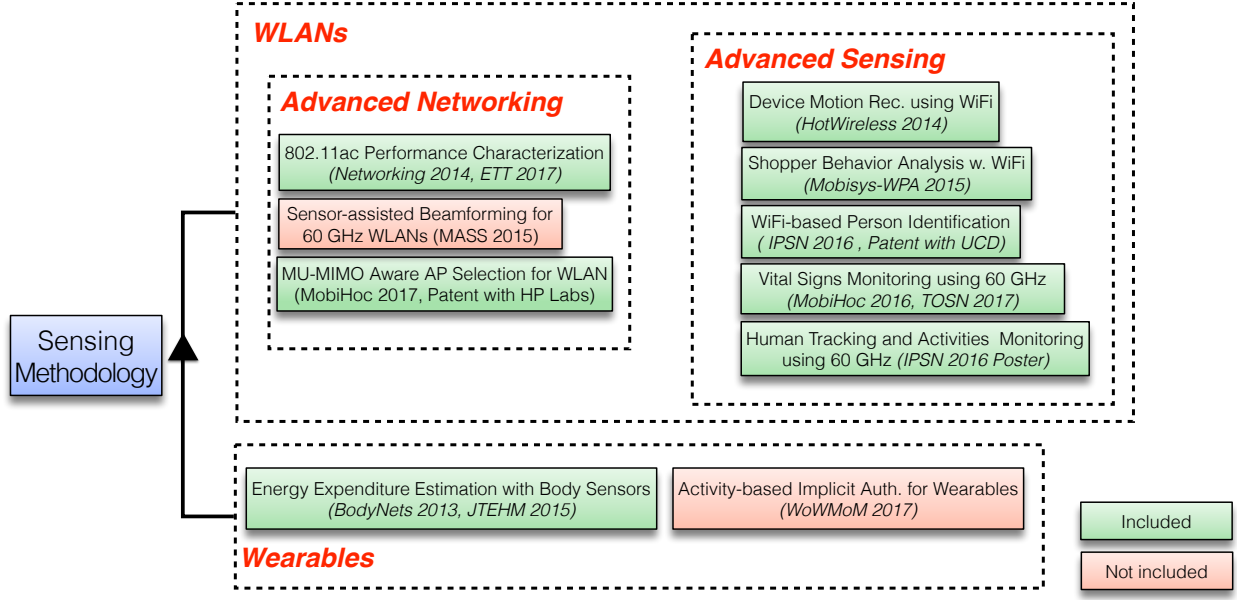


Figure 1.1. Research Scope

evaluation of these factors and their impact using a real 802.11ac testbed. Our findings provide numerous insights on benefits and challenges associated with using 802.11ac in practice. With such findings, although there are various performance issues in current WLANs, we feel that the considerable throughput gain can satisfy most usage scenarios. It motivates our direction of diversifying and enriching the functionality of next-generation WLANs services.

- **Understanding sensing methodology: energy expenditure estimation with wearable sensors**

We start of understanding sensing methodology by using wearable sensors to conduct Energy Expenditure Estimation (EEE) which is an essential step in tracking personal activities, and preventing chronic diseases such as obesity, diabetes and, cardiovascular diseases. Accurate and online EEE utilizing small wearable sensors is a difficult task, primarily because most existing schemes work offline or using heuristics. In this work, we focus on accurate EEE for tracking ambulatory activities (e.g., walking, standing, climbing upstairs or downstairs) of a typical smartphone user. We used existing smartphone sensors (e.g., accelerometer and barometer sensor), sampled at low frequency, to detect EEE accurately. Using artificial neural networks, a machine learning technique, we build a generic regression model for EEE that yields up to 89% correlation with actual energy expenditure. Using barometer data, in addition to accelerometry is found to significantly improve EEE performance (up to 15%). We compare our results against state-of-the-art Calorime-

try Equations (CE) and consumer electronics devices (Fitbit and Nike + Fuel Band). We were able to demonstrate the superior accuracy achieved by our algorithm. This work also gives us the inspiration of our following work to bring sensing capability to WLANs.

- **Enabling sensing application through 2.4/5 GHz-based WLANs**

Recent WiFi standards use Channel State Information (CSI) feedback for better MIMO and rate adaptation. CSI provides detailed information about current channel conditions for different sub-carriers and spatial streams. In this work, we first show that CSI feedback from a client to the AP can be used to recognize different fine-grained motions of the client. We find that CSI can not only identify if the client is in motion or not, but also classify different types of motions. To this end, we propose APsense, a framework that uses CSI to estimate the sensor patterns of the client. APsense brings the sensing capability to the AP. It is observed that client's sensor (e.g., accelerometer) values are correlated to CSI values available at the AP. We show that using simple machine learning classifiers, APsense can classify different motions with accuracy as high as 90%.

Following the APsense framework, we then leverage CSI to detect human activities to enable a variety of sensing applications. Understanding shopper's behavior through physical analytics can provide crucial insights to the business owner in terms of the effectiveness of promotions, the arrangement of products, and the efficiency of services. However, analyzing shopper's behavior and browsing patterns is challenging. Since video surveillance cannot be used due to high cost and privacy concerns, it is necessary to design novel techniques that can provide an accurate and efficient view of shopper's behavior. We propose WiFi-based sensing of shopper's behavior in a retail store. Specifically, we show that profiling CSI of WiFi can accurately classify various states of a shopper such as standing near the entrance to view a promotion or walking quickly to proceed towards the intended item. We recognize a few representative states of shopper's behavior at the entrance and inside the store, and show how CSI-based profile can be used to detect that a shopper is in one of the states with very high accuracy ( $\approx 90\%$ ).

- **Enriching WLANs with device-free WiFi-based person identification system in smart spaces**

There has been a growing interest in equipping the objects and environment surrounding the user with sensing capabilities. Smart indoor spaces such as smart homes and offices can implement the sensing and processing functionality, relieving users from the need of wearing or carrying smart devices. Enabling such smart spaces requires device-free effortless sensing of user's identity and

activities. Device-free sensing using WiFi has shown great potential in such scenarios. However, fundamental questions such as person identification have remained unsolved. In this work, we present WiWho, a framework that can identify a person from a small group of people in a device-free manner using WiFi. We show that CSI used in recent WiFi can identify a person's steps and walking gait. The walking gait being a distinguishing characteristic for different people, WiWho uses CSI-based gait for person identification. We demonstrate how step and walk analysis can be used to identify a person's walking gait from CSI, and how this information can be used to identify a person. WiWho does not require a person to carry any device and is effortless since it only requires the person to walk for a few steps (e.g., entering a home or an office). We evaluate WiWho using experiments at multiple locations with a total of 20 volunteers and show that it can identify a person with an average accuracy of 92% to 80% from a group of 2 to 6 people. We also show that in most cases walking as few as 2-3 meters is sufficient to recognize a person's gait and identify the person. We also discuss the potential and challenges of WiFi-based person identification with respect to smart space applications.

- **Enriching WLANs with MU-MIMO-aware AP selection system**

Major Wi-Fi AP vendors worldwide seek to provide gigabit wireless connectivity, by densely deploying MU-MIMO capable APs, which can support multiple, concurrent data streams to a group of clients, connected to them. However, MU-MIMO gains can only be achieved if an AP can identify groups of clients with homogenous configurations and orthogonal wireless channels, where concurrent transmissions will not cause inter-client interference. Hence, MU-MIMO performance is fundamentally depending on how the clients are assigned to APs. Our experiments with 802.11ac commodity testbeds show that state-of-the-art client assignment algorithms are MU-MIMO oblivious and limit the MU-MIMO grouping opportunities in realistic settings. In this work, we leverage the enabled sensing capability to sense the current environment in order to design and implement MAPS, an MU-MIMO-Aware AP Selection algorithm that is 802.11-compliant and can boost network's MU-MIMO throughput gains. We verified MAPS' gains over legacy designs via extensive experiments with 802.11ac commodity testbeds.

- **Enabling sensing application through 60 GHz-based WLANs**

In the end, we move to the future generation of WLANs system (e.g., 60 GHz networks). We enable sensing ability to 60 GHz networks by proposing human sensing, activity monitoring and

vital signs monitoring using 60 GHz millimeter wave (mmWave). We discuss the benefits of using mmWave signals for the purpose over existing 2.4/5 GHz based techniques. We also identify related challenges of determining human's initial location and tracking, and demonstrate the feasibility of activity and vital signs monitoring. The major contribution of this work is focusing on how to use 60 GHz WLANs to monitor human vital signs. Continuous monitoring of human's breathing and heart rates is useful in maintaining better health and early detection of many health issues. Designing a technique that can enable contactless and ubiquitous vital sign monitoring is a challenging research problem. We present a system that uses 60 GHz millimeter wave (mmWave) signals for vital sign monitoring. We show that the mmWave signals can be directed to a human's body and the RSS of the reflections can be analyzed for accurate estimation of breathing and heart rates. Our system relies on a novel human finding procedure, where a human can be located within a room by reflection loss based object/human classification. We evaluate our system using a 60 GHz testbed in home and office environment and show that it provides the mean estimation error of 0.43 bpm (breathing rate) and 2.15 bpm (heart rate). Also, it can locate the human subject with 98.4% accuracy within 100 ms of dwell time on reflection.

### 1.3 Outline

The rest of the thesis is organized as follows. In Chapter 2 we present the performance characterization of the latest WLANs as a motivation of the following work to enrich WLANs. In Chapter 3 we understand the sensing methodology by designing energy expenditure estimation algorithm using wearable sensors. From Chapter 4 to Chapter 7 we present four accomplished work to enrich the functionality of WLANs with novel sensing and networking applications. Chapter 4 talks about enabling sensing capability through 2.4/5 GHz WLANs, where fine-grained device motion recognition and shopper's behavior analysis through WiFi signals are introduced. In Chapter 5 we design the first-of-its-kind device-free WiFi-based person identification system for smart spaces. In Chapter 6 we design and implement an MU-MIMO-aware intelligent AP selection system to boost the performance of the latest 802.11ac WLANs. In Chapter 7 we enable sensing capability through 60 GHz WLANs, where 60 GHz-based human sensing, activity monitoring and vital signs monitoring are introduced. Finally, we conclude in Chapter 8.

# **Chapter 2**

## **Understanding the Latest WLANs: Performance Characterization of 802.11ac Networks**

### **2.1 Introduction**

With the tremendous increase in wireless access networks traffic, 802.11n-based WLANs have become increasingly popular. The next generation WiFi standard, 802.11ac, [1–4] builds on top of 802.11n to create even faster and more scalable WLANs. With the higher throughput of 802.11ac, it is now possible to support more laptops and mobile devices from each AP as well as high data rate applications. Due to its potential of providing very high throughput, many of the leading smartphone and laptop manufacturers (Samsung Galaxy S4/S5 [5,6], Apple MacBook Air/pro [7,8], HTC One [9]) have already adapted 802.11ac. Compared to current 802.11n, the performance gains of 802.11ac are due to three enhancements - (i) larger channel width and dynamic channel width selection, (ii) denser modulation and (iii) support for more spatial streams (SS) and Multi-user MIMO. The first generation of 802.11ac products include the first two factors while supporting up to 4 SS.

This work provides a performance characterization of 802.11ac using experiments on a real testbed for both indoor and outdoor environment. 802.11ac is a Very High Throughput (VHT) amendment that has the potential to deliver a gigabit of throughput in WLANs. The newly introduced features also bring us new issues when we use them in real cases. To the best of our knowledge, this is the first work to present experimental evaluation and complete characterization of the standard. With larger channel width being one of the most significant changes in 802.11ac, the primary focus of our work is to find out pros and cons of utilizing larger channel widths. The observed throughput when an 802.11ac link is operating at 80 MHz channel width (with 256 QAM and 3 spatial streams) can reach up to 660 Mbps. With very high throughput as a known fact of 802.11ac, we center our study on two critical issues of

*energy efficiency* and *interference*, and provide novel insights on how larger channel width affects both of them. We have performed experiments on three different 802.11ac chipsets (on laptop and smartphone) to verify our results.

The primary goal of this work is to provide a detailed understanding of 802.11ac using experiments and to identify how current wisdom about network planning should be adapted to take complete benefit of it. We present a comprehensive study of energy efficiency of 802.11ac using measurements on a smartphone. This understanding can be useful to devise strategies whereby the choice of channel width, modulation and coding rate, and spatial streams can be optimized to minimize power consumption while achieving higher throughput. We also show that while a larger channel width can significantly improve the throughput, it gives rise to new kinds of fairness issues. We elaborate on the causes of these unfairnesses and point out solutions for them. The presented findings can be used to derive physical/MAC layer protection or scheduling mechanisms that can resolve the issues.

The main contributions of this work are as follows:

1. We provide the first testbed based performance characterization of 802.11ac in both indoor and outdoor environment with and without interference. We verify that 802.11ac increases the throughput by 91% compared to the best performance that 802.11n can achieve. We study various factors - modulation, SS and channel width - jointly and in isolation to characterize their impact on throughput. We find no performance improvement can be gained using 256 QAM beyond 10 meters, and the majority of the throughput increase is attributed to the larger channel width.
2. We characterize the power consumption of 802.11ac using measurements. We find that
  - ▶ idle mode power consumption when a radio is operating at larger channel width is much higher, which makes larger channel width a less energy efficient option overall, and
  - ▶ increasing SS is more energy efficient compared to doubling the channel width for achieving the same percentage increase in throughput.

The energy efficiency analysis shows how an optimal choice of channel width, SS and MCS can be made to meet the throughput requirement while lowering the energy consumption.

3. We identify new throughput and fairness anomalies that are introduced by using a larger channel width. We show
  - ▶ In heterogeneous channel width environment where different links operate at different channel

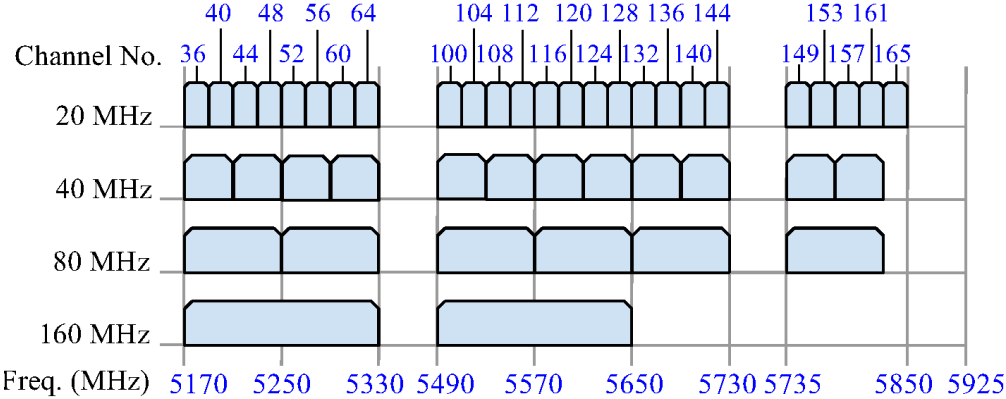


Figure 2.1. FCC 5GHz unlicensed band channel map. There are 25 20 MHz bands, 12 40 MHz bands, 6 80 MHz bands and 2 160 MHz bands in this band.

widths, competition to access the medium becomes increasing unfair which results in starvation of the larger channel width links. As an example, we show that when a 20 MHz link is operating in secondary channels of an 80 MHz 802.11ac link, the performance of the latter degrades severely.

We provide a detailed analysis of the throughput anomaly issues and outline possible solutions.

The work is organized as follows. We start out by providing an overview of new components of 802.11ac and our experiment setup in the following section. In Section 2.3, we benchmark different characteristics of 802.11ac in ideal conditions. We also consider realistic scenarios with interference using a multi-node indoor testbed. Section 2.4 presents energy efficiency characterization of 802.11ac. Interference characterization and details of how dynamic channel width selection in 802.11ac works are provided in Section 2.5, followed by the related work in Section 2.7 and conclusions in Section 2.8.

## 2.2 Overview of 802.11ac and Experiment Setup

In this section, we will give a brief overview about 802.11ac and highlight the new features it brings to us. Then, we will introduce the experiment devices and experiment layout we used in this work.

### 2.2.1 What is new in 802.11ac?

A brief description of mechanisms that are used by 802.11ac to achieve higher throughput is as following.

**Larger Channel Width:** One of the most significant changes in 802.11ac is that it operates in 5 GHz band only, and not in much more crowded 2.4 GHz band. It has an added support for 80 MHz and 160 MHz (optional) channel widths. Fig. 2.1 shows the 5 GHz spectrum for the United States along with non-overlapping channels for different channel widths. As we can see, 5 GHz band has 25 non-overlapping 20 MHz channels which provide us with a much larger band compared to 2.4 GHz.

MCS	Modulation	Coding
0	BPSK	1/2
1	QPSK	1/2
2	QPSK	3/4
3	16-QAM	1/2
4	16-QAM	3/4
5	64-QAM	2/3
6	64-QAM	3/4
7	64-QAM	5/6
8	256-QAM	3/4
9	256-QAM	5/6

Figure 2.2. 802.11ac MCS index table. The table is simplified to have only 10 values and the spacial streams information is not indicated in this table.

However, due to fragmentation, only a few 80 and 160 MHz channels are available. There can be at most 6 non-overlapping 80 MHz (or two 160 MHz) channels in this band. Also, some channels (such as 120, 124 and 128) can not be used to avoid interference with weather radar systems.

Even if an 802.11ac AP is using 80 MHz channel width, it still utilizes a 20 MHz channel inside the 80 MHz as a control channel. This channel is referred as the *primary channel*. Beacons and management frames are sent over the primary channel. The purpose of using the primary channel is twofold. First, it is used to determine the channel width (20, 40, 80 or 160) in real time depending on the current interference. As we will discuss in Section 2.5, an Enhanced RTS/CTS protocol is used for dynamic channel width selection. Second, 802.11a/n clients which are capable of operating at the maximum of 40/20 MHz channels can still receive the beacons and connect to an 802.11ac AP.

**Denser Modulation:** 802.11ac introduces support for 256 QAM and also simplifies the MCS index (only 10 values). Fig.2.2 lists the MCS values and their corresponding modulation and coding rates. MCS 8 and 9 utilize 256 QAM which is the highest constellation density currently supported by any 802.11 standards. In 802.11n, the MCS index was used to indicate both the modulation and coding scheme and SS. In 802.11ac, the MCS indices are simplified to indicate just the modulation and coding scheme.

**More MIMO:** 802.11ac supports up to 8 SS, although we only use 3 SS for our experiments. Support for multi-user MIMO, which enables a single AP to transmit to multiple clients simultaneously in the same channel, is also included but we do not include them in our study as none of the current 802.11ac products implement it.

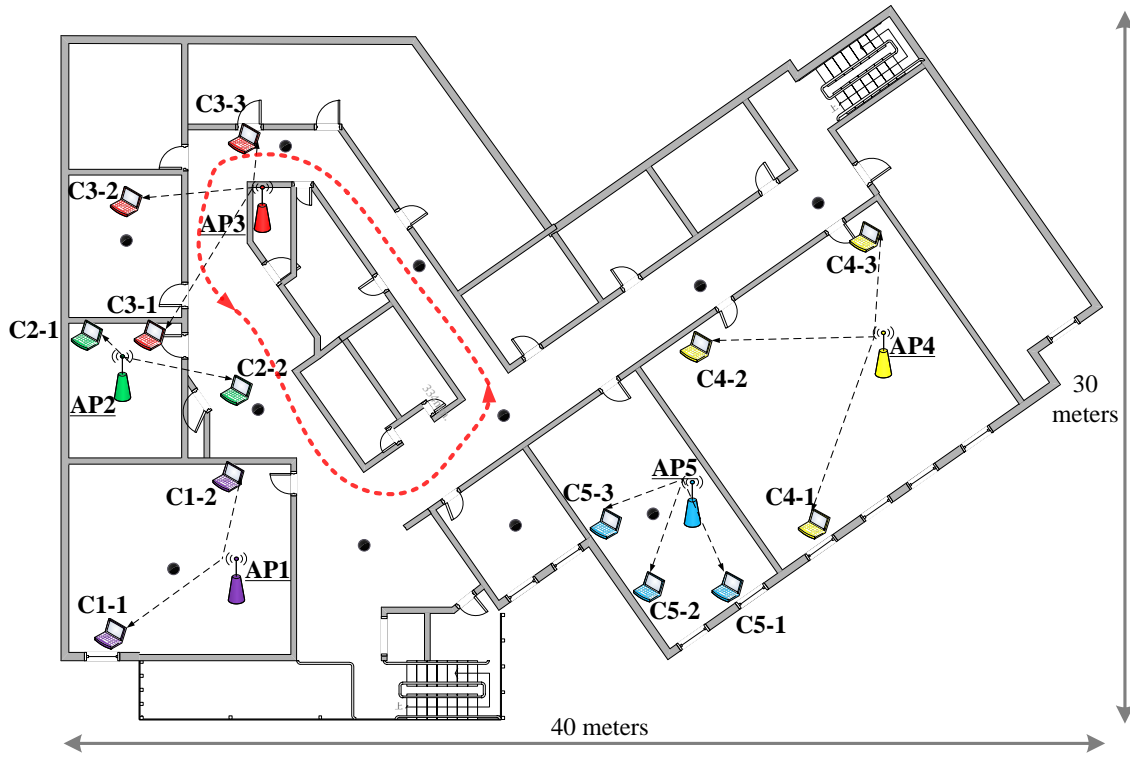


Figure 2.3. Testbed of 18 802.11ac nodes used for the experiments. We use this 18 nodes to do the experiments for the indoor characterization only. The outdoor measurement, energy efficiency and interference cases are not included in this figure.

## 2.2.2 Experiment Setup

We build our testbed using commercial 802.11ac hardware.

**Access Points:** We use ASUS-RT-AC66U router [10] as APs. The router is based on a Broadcom BCM4360 chipset which can support 80 MHz channel width, up to 256 QAM and 3x3:3 MIMO. We run a Linux distribution (AsusWRT-Merlin 3.0) on the routers.

**Clients:** We use three different 802.11ac chipsets in our experiments. Repeating the experiments for different hardware ensures that we do not end up profiling a specific hardware. Instead, we profile the issues of 802.11ac which are common across all hardware. The chipsets and platforms we use are as following:

1. Asus PCE-AC66 [11]: 3 SS, mini PCI-E on a laptop
2. Qualcomm Atheros QCA9880 in WLE900V5-18 NIC [12]: 3 SS, Ath10k Linux driver, mini PCI-E on laptop
3. Broadcom BCM4335: 1 SS, Samsung Galaxy S4 smartphone [5]

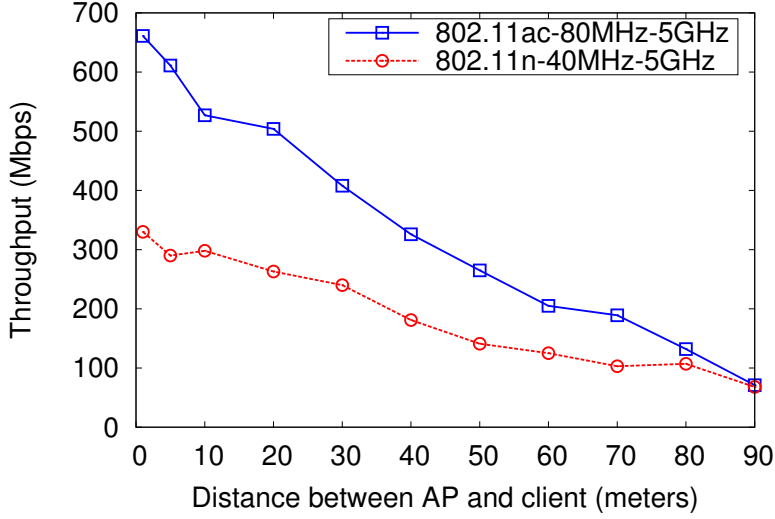


Figure 2.4. Throughput comparison between 802.11ac and 802.11n

In the LOS (Line-Of-Sight) scenario, one link (AP-client pair) was deployed on terrace of a university parking lot. The experiments were repeated on another parking lot for verification. These locations were chosen as they provided a LOS link for up to 100 m without any external interference in 5GHz. In the second scenario, a total of 18 nodes (5 APs and 13 clients) were deployed indoors in a university building (Fig.2.3) to create a more practical scenario of non-LOS links. Although campus WiFi network was operating in 5 GHz band, the activity was negligible, especially during night time when our experiments were carried out. Unless explicitly mentioned, all the experiments presented in this work were repeated 5-10 times for increased confidence in results. Each run of the experiment involves running Iperf for anywhere between 3 to 5 minutes.

In the next three sections, we characterize the throughput performance, energy efficiency and interference of 802.11ac-based WLANs. We start with more straightforward and apparent results and then proceed toward the complex and critical characterization.

### 2.3 Performance Characterization

In this section, we first analyze the performance of an 802.11ac link using Asus PCE-AC66 adapter on a laptop in ideal RF settings where there is a LOS link with no other interference. We use this to benchmark 802.11ac's performance, and later use it for comparison in more complex scenarios.

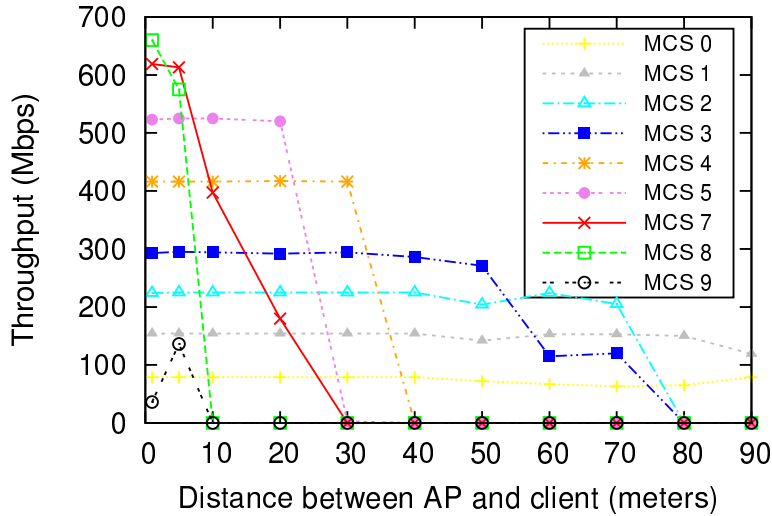


Figure 2.5. Throughput with different MCS values when SS = 3

### 2.3.1 Performance of an Isolated 802.11ac Link

In this experiment, we fix the location of the client on one end of the parking lot and move the AP away from the client. We create a downlink (AP to client) Iperf UDP flow which sends data at the maximum possible data rate. The measurements of throughput are presented in Fig.2.4. Here, 802.11ac is operating in 80 MHz channel with "auto" mode which means that the MCS value and number of SSs are chosen automatically. The best case throughput of 802.11ac is observed at 1 meter distance to be 661 Mbps. For comparison, at each distance, we repeat the experiments for 802.11n with 40 MHz channel width. Here, we use default rate adaptation to select the best MCS and SS combination. As shown in Fig.2.4, we found that operating in 80 MHz can improve the throughput by nearly 82% in first 30m, and 91% on an average across all distances (from 1m to 90m).

### 2.3.2 Characteristics of (MCS x SS)

**Denser Modulation:** 802.11ac introduces the use of 256 QAM (MCS 8 and 9 in Fig.2.2). To study how well the 256 QAM works in real-world, we fix SS=1. These settings are referred as 8x1 or 9x1 in the format of MCSxSS. For comparison with 64 QAM, we also study 7x1 and 6x1 settings. The throughput results are shown in Table 2.1. It is observed that 9x1 (256 QAM) gives up to 29% improvement over 7x1 (64 QAM). Also, higher coding rate (e.g., 5/6 for 9x1 and 7x1) improves the throughput by around 10% compared to lower coding rate (e.g., 3/4 used in 8x1 and 6x1).

Next, we fix the SS=3 and vary the MCS from 0 → 9. The results are shown in Fig.2.5. We see that although 256 QAM can achieve a significant increase in throughput, it is practically useless since MCS

Table 2.1. Throughput (Mbps) of a link when channel width = 80MHz, MCS = 6, 7, 8 or 9, and SS = 1

Distance	6x1	7x1	8x1	9x1
10m	228	252	297	325
20m	229	252	297	326
30m	223	252	297	325

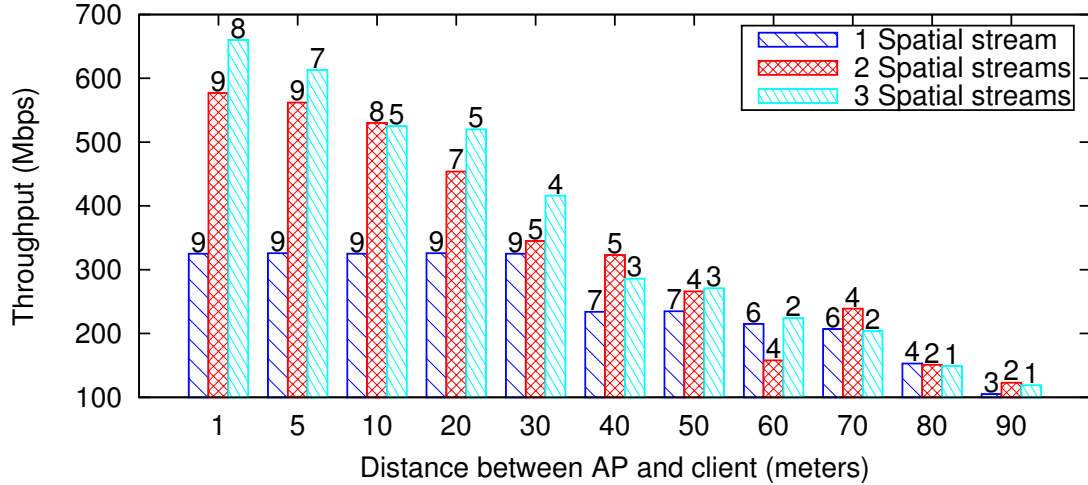


Figure 2.6. Maximum throughput when SS = 1, 2 or 3 (MCS value labeled on top of each bar)

8 and 9 yield no throughput beyond 10 meters even in LOS and zero interference environment.

**MCS x SS:** We repeat the experiments for all possible combinations of MCS x SS at each distance point, and the results are presented in Fig.2.6. For clarity, we only present 3 results for each distance showing the MCS value that achieves the maximum throughput when using 1, 2 and 3 SS. As we can see, adding an additional SS increases the throughput but the increase is not 100% except for the shorter distances.

An interesting observation from Fig.2.6 is that for many distances there exists combinations of MCS x SS that can yield comparable throughput. For example, at 10m distance, 8x2 and 5x3 achieve almost the same throughput. This is especially important as it shows that the choice of MCS x SS should not be clearly driven by achievable throughput, and other factors such as client's power consumption can also be considered.

*Findings:* We observed that newly introduced MCS 8 and 9 have limited usefulness in most practical cases. We also showed that many possible combinations of MCS x SS can achieve similar throughput. In such cases, the choice of MCS x SS can be based on other factors such as their power consumption.

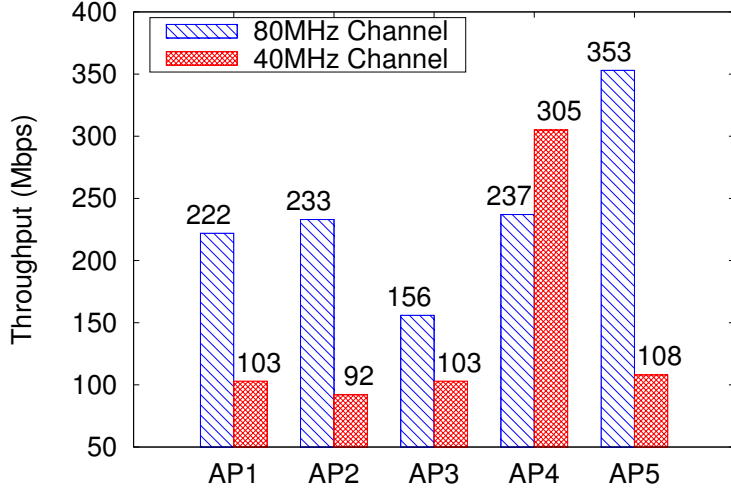


Figure 2.7. The aggregate throughput for each AP using 80 MHz and 40 MHz channel widths

### 2.3.3 Performance Characterization in Indoor Environment

Table 2.2. Throughput (Mbps) comparison between 802.11ac at 80 MHz and 802.11n at 40 MHz in indoor environment

	Standard	Avg	Max	Min
802.11ac	463	643	253	
802.11n	247	358	127	

We now characterize the performance of an 802.11ac link indoors in a university building. Note that the campus WiFi network was operating in 5 GHz band but the activity was negligible, especially during night time when our experiments were carried out. First, we fix the location of the AP at location AP2 in Fig. 2.3. We then vary the location of the client at 11 different locations (marked with black dots in Fig.2.3), and start downlink Iperf flow at the maximum rate. We observe the maximum measured throughput to be 643 Mbps, the minimum throughput of 253 Mbps while the average throughput is 463 Mbps. We also repeat the experiment for 802.11n, and the comparison is shown in Table.2.2 where we observe that 802.11ac almost doubles the average throughput comparing to 802.11n.

Next, to evaluate the impact of larger channel width on mobility, we move the client around the AP at walking speed for five minutes. The track of mobility is shown in Fig.2.3 with a red dotted line. The average throughput of three such experiments was observed to be 491 Mbps for 802.11ac with 80 MHz channel width. No significant impact of larger channel width is observed on throughput variation at walking speeds compared to the stationary cases. We repeat the same experiment using 802.11n with 40

Table 2.3. Throughput (Mbps) of different clients when multiple APs simultaneously transmit

Channel Width	C1-1	C1-2	C2-1	C2-2	C3-1	C3-2	C3-3	C4-1	C4-2	C4-3	C5-1	C5-2	C5-3
80MHz	112	110	117	116	54	52	50	80	76	81	117	120	116
40MHz	52	51	45	47	43	39	31	102	100	103	36	36	36

MHz channel width, and the average throughput is 223 Mbps.

We also create a scenario where a total of 18 nodes (5 APs and 13 clients) are deployed as shown in Fig.2.3. Here, a maximum of 3 clients connect to each AP. Each AP creates a downlink Iperf flow to each of its clients and sends packets to them simultaneously. We repeat the experiments for 80 and 40 MHz channel widths. The throughput measurements are presented in Fig.2.7 and Table.2.3. During the experiments of 80 MHz, (AP1, AP2, AP3) pick the same channel while (AP4, AP5) pick another non-overlapping channel. In the case of 40 MHz, (AP1, AP2, AP3, AP5) and AP4 operate on distinct channels. However, we tried multiple layout configurations, but no meaningful patterns in the throughput variation were found. The potential factors affecting the throughput could be the topology or how channels are shared/divided between different links. More experiments are required for a clear understanding and we leave it for the future work.

## 2.4 Energy Efficiency of 802.11ac

Energy efficiency has become a crucial design factor when building newer standards of communications for mobile devices. With more and more smartphones and laptops adapting 802.11ac, it is imperative to study the energy efficiency of 802.11ac.

To this end, we perform the experiments on two different 802.11ac chipsets, i.e. Atheros QCA9880 in a laptop and Broadcom BCM4335 in a smartphone. We use Monsoon power monitor [13] to bypass the power supply in both cases and measure the power consumption.

802.11ac is the first standard to introduce 80 MHz channel width for commercial use. To our knowledge, this is the first work to explore the trade-off between power consumption and throughput when using 80 MHz channel width.

### 2.4.1 Idle Listening - A Dominant Factor

First of all, we try to understand how utilizing different channel widths differs in terms of their resultant power consumption. For this, we perform an experiment on the laptop with QCA9880 where we fix Iperf's source rate  $S = 1$  Mbps, MCS = 7 and SS = 2. We then vary the channel width (20, 40 and 80 MHz) of the link. The results are presented in Table 2.4.

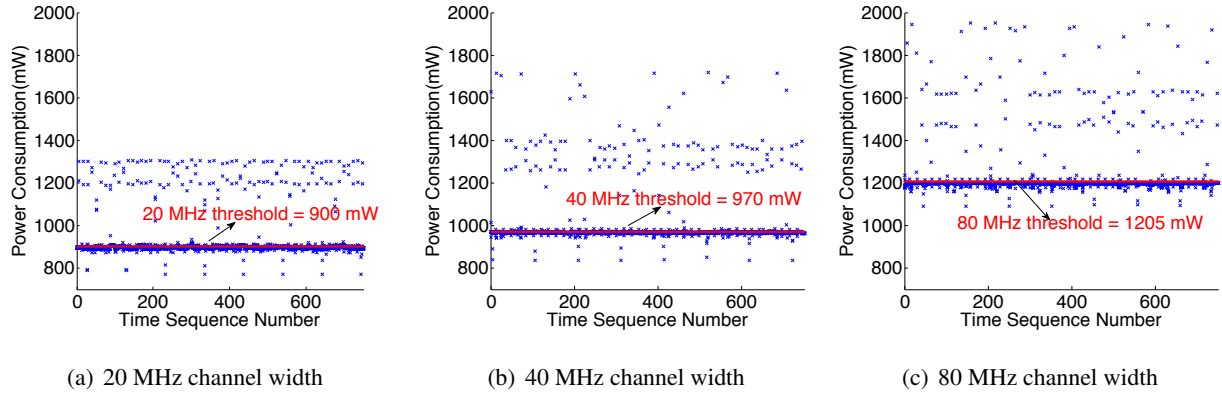


Figure 2.8. Power consumption samples with idle to active threshold line for different channel widths. The power measurement sampling rate is 50Hz.

Table 2.4. Detailed power consumption of QCA9880 when operating on different channel widths

CW (MHz)	P <sub>active</sub> (mW)	T <sub>active</sub> (%)	P <sub>idle</sub> (mW)	T <sub>idle</sub> (%)	P <sub>average</sub> (mW)
20	948.72	26	894.19	74	908.29
40	1119.02	9	966.55	91	979.31
80	1468.07	5	1196.12	95	1208.37

Average power consumption ( $P_{\text{average}}$ ) can be calculated using

$$P_{\text{average}} = P_{\text{active}} \cdot T_{\text{active}} + P_{\text{idle}} \cdot T_{\text{idle}} \quad (2.1)$$

where  $P_{\text{active}}$  and  $T_{\text{active}}$  are the average power consumption and the percentage of the time when the radio is active (sending or receiving);  $P_{\text{idle}}$  and  $T_{\text{idle}}$  are the average power consumption and the percentage of the time when the radio is idle. Here, we determine whether the radio is idle or not by analyzing power measurement samples. If a sample is below the pre-selected threshold, we consider it as an idle sample; otherwise we consider it as an active sample. The detail about how these thresholds are selected and the power samples distributions for 20 MHz, 40 MHz and 80 MHz channels are shown in Figure. 2.8(a), 2.8(b) and 2.8(c). From [14], we can get the theoretical way to calculate  $T_{\text{active}}$  (percentage of active time) as

$$T_{\text{active}} = \lambda_g \cdot T_L \quad (2.2)$$

where  $\lambda_g$  is the frame generation rate, and  $T_L = T_{\text{PLCP}} + (H + L)/R_{\text{PHY}}$  is the time required for transmitting a frame. Here,  $L$  is the frame size,  $H$  is the MAC layer overhead,  $R_{\text{PHY}}$  is determined by MCS, SS and channel width, and  $T_{\text{PLCP}}$  is the time for transmitting Physical Layer Convergence

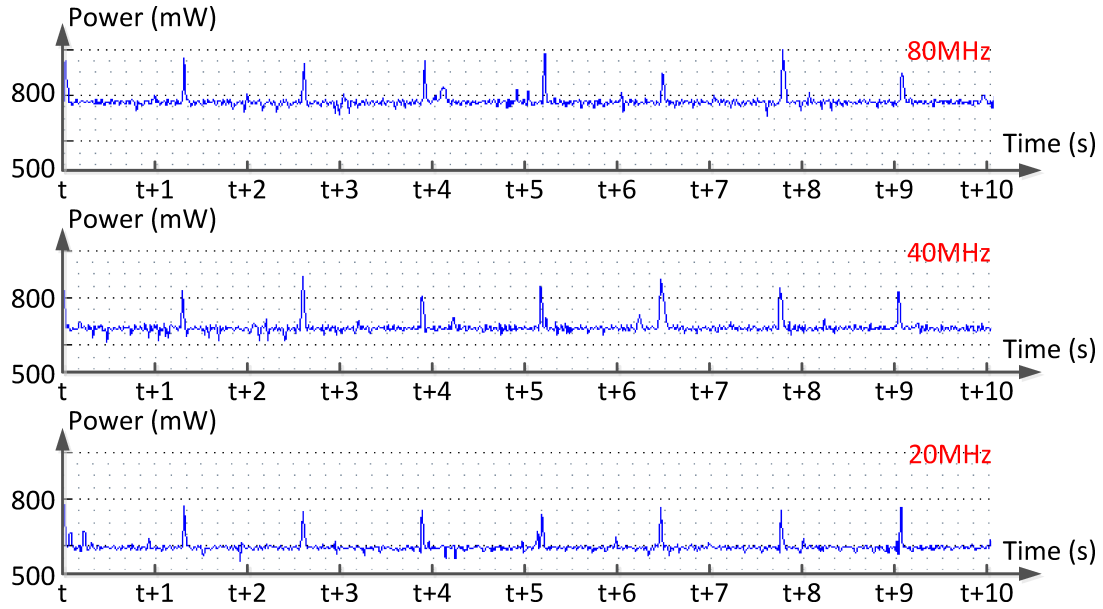


Figure 2.9. Comparison of dynamic power consumption between different channel widths (with 1 Mbps receiving rate constantly) on smartphone

Protocol (PLCP) preamble which is usually sent at a low PHY rate. However, the theoretical values calculated using Equation 2.2 are much lower than the values we get in Table 2.4. The reason is that 802.11ac requires RTS/CTS as a mandatory part to determine channel width and RTS/CTS frames are sent in an 802.11a Physical Protocol Data Unit (PPDU) format with 20 MHz which uses a low PHY rate [1,3]. In this way, the actual percentage of active time can be much higher than the theoretical value.

As we can see in Table 2.4,  $T_{\text{active}}$  decreases as expected when we increase the channel width. Also, as we expect,  $P_{\text{active}}$  increases since the same amount of data is being sent over a smaller time period when using larger channel widths.

What is surprising to see is that even though the radio spends more time in idle mode when operating at larger channel widths, the actual power consumption during the idle mode ( $P_{\text{idle}}$ ) is much higher. This results in an overall increase in power consumption ( $P_{\text{average}}$ ) even though the radio is idle majority of the time.

We repeat the same experiments for smartphone with the same settings except that it supports only one SS. Note that we consider the whole system's power consumption which includes both NIC and CPU for smartphone. Since it is a relatively more complicated system, we do not apply a threshold to smartphone's data. Instead, we have confirmed the idle listening power to be the smooth line between spikes in Fig. 2.9 by making the phone idle and measure its power. The results are shown in Fig. 2.9 where we observe the same phenomenon - idle listening at larger channel widths dominates the overall

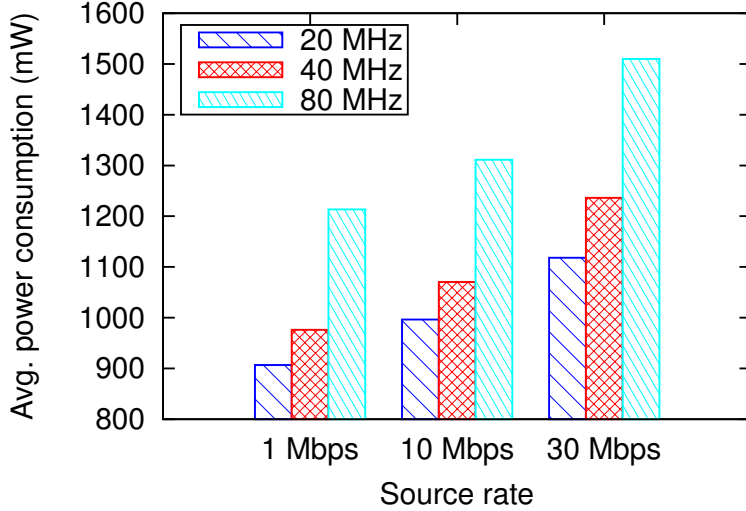


Figure 2.10. Power consumption of the most energy efficient setting in different channel widths at different source rates

power consumption. We observe that when receiving at the same data rate, using 80 MHz channel width consumes 14% more power compared to 40 MHz. Similarly, it consumes 12% more power when running at 40 MHz compared to operating at 20 MHz.

The "race to sleep" heuristic which is studied in [15] also holds true in our case although we do not consider the sleep state in this work. It is obvious that, for a given amount of data, a larger channel width would allow the transfer to complete faster and radio can return to sleep mode sooner, reducing the overall energy consumption. However, here we focus on comparison based on a given input rate as it is more useful in practical scenarios.

*Findings:* Since larger channel widths allow a radio to send/receive at faster rates, one might expect that overall power consumption will be reduced because the radio can spend more time in idle mode. Although this is true, the power consumption in idle mode is much higher at larger channel widths which in fact dominates the overall power consumption, making larger channel widths a less energy efficient option. It is necessary to devise intelligent power saving schemes that can reduce the power consumption of idle mode operations in larger channel widths.

#### 2.4.2 Impact of Rate & Channel Width Adaptation:

In practice, the physical layer data rate of the link is adapted based on the channel condition. Various rate control schemes are designed to adapt MCS x SS with the objective being maximization of the throughput [16–19]. Recent work such as [20, 21] have proposed rate adaptation schemes that try to minimize the energy consumption. Here, we seek the answer for a simple question: can joint rate

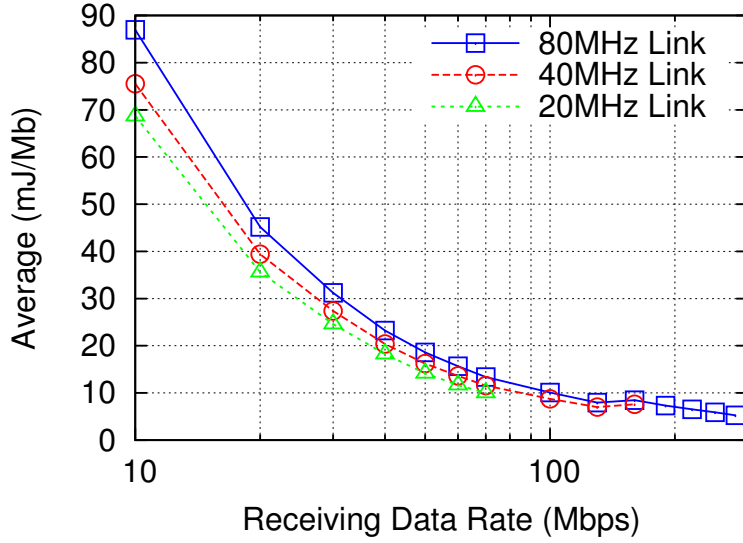


Figure 2.11. Comparison of per megabit energy cost between different channel widths

and channel width adaptation (finding CW x MCS x SS) yield additional energy benefits compared to performing just the energy-efficient rate adaptation (MCS x SS)?

To understand this, we perform a set of experiments where we try to find the most energy efficient MCS x SS combination using a brute-force approach. For each channel width, we try out all combinations of MCS ( $0 \rightarrow 9$ ) and SS ( $1 \rightarrow 3$ ) and find out the most energy efficient combination that can satisfy a given source rate. Since the source rate is fixed, power consumption results will be equivalent to energy results. We repeat the experiments for several different source rates, and the results are shown in Fig.2.10.

As we see in Fig. 2.10, the power consumption of the most energy efficient MCS x SS combination for a larger channel width is always higher than that of a smaller channel width. In the experiments, a higher MCS value (either 7 or 8) and one SS is observed to be the most energy efficient in most cases. This is in line with [15] which suggests that choice of higher MCS is more energy efficient.

These results show that a larger channel width consumes more power, and it is more energy efficient to use smaller channel width if the source rate can be satisfied by doing so.

We repeat the experiments for many different source rates on the smartphone and observe the same phenomenon where power consumption proportionally increases as the channel width increases. The results are presented in Fig. 2.11. Note that for a fair comparison at different source rates, we present the energy consumption values in Mega-Joule/Megabit (mJ/Mb) as a unit of comparison. Here, mJ/Mb can be calculated as  $mJ/Mb = (\text{Power consumption in mW}) / (\text{Goodput in Mbps})$ .

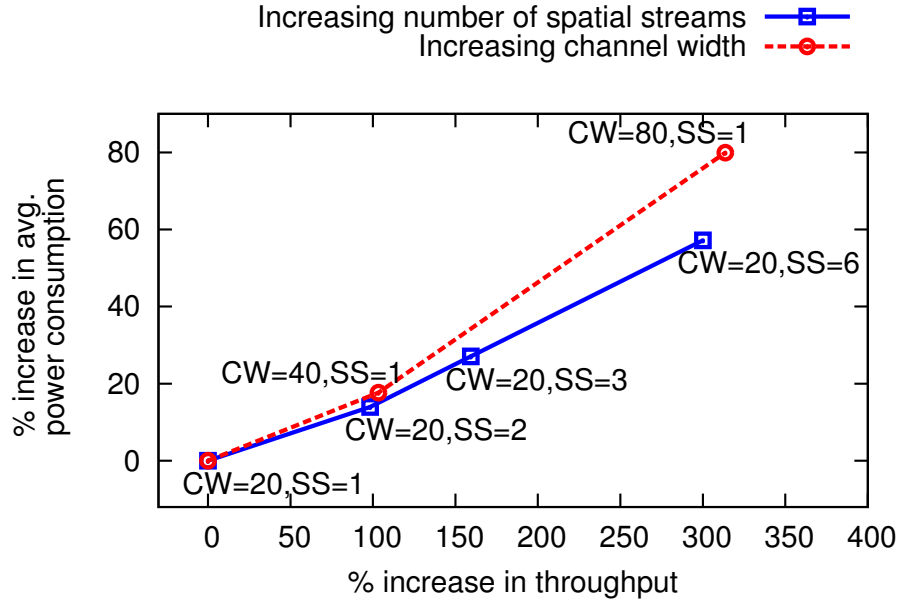


Figure 2.12. Comparison of percentage increase in power consumption with increasing SS or increasing channel width

*Findings:* For the throughput values that can be achieved with both larger and smaller channel widths, utilizing larger channel width consumes more power. Since the power consumption increases proportionally with channel width, no additional energy benefits can be achieved with joint channel width and rate adaptation.

**Control Message Overhead:** Since 802.11ac mandates the use of RTS/CTS (discussed in Section 2.6.1), one potential reason of this higher power consumption can be that 80 MHz width requires 4 times more RTS/CTS compared to 20 MHz. To verify if the power consumption is actually due to these added RTS/CTS overhead, we repeat the same experiments using 802.11n with RTS/CTS disabled. We observe that even in 802.11n, when smartphone uses 40 MHz, it also consumes more power compared to when operating in 20 MHz. This proves that additional power consumption is not due to increased overhead of RTS/CTS when using larger channel width.

### 2.4.3 Channel Width vs. Spatial Streams

Two main factors responsible for throughput gains of 802.11ac are more SS and larger channel width. Both of these factors achieve a similar increase in throughput - e.g. increasing SS from 1 to 2 nearly doubles the throughput, similarly, doubling the channel width from 40 Mhz to 80 Mhz also has the same effect on throughput. We raise a simple question, since the throughput increase of both mechanisms is comparable, how different are they in terms of their power consumption?

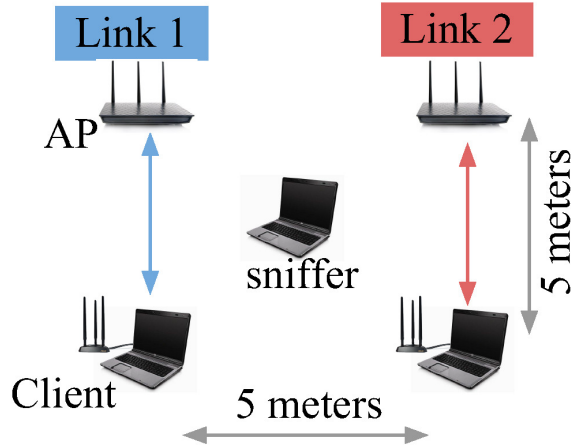


Figure 2.13. Indoor setup of 2 links and a sniffer

To understand this, we perform an experiment where we fix the MCS and configure Iperf to send at maximum possible source rate. We then perform two sets of operations. In the first one, we double the channel width while keeping SS the same. In the second, we increase SS while keeping the channel width unchanged. In both cases, we observe the percentage increase in throughput and power consumption. The results are presented in Fig. 2.12, which shows that increasing channel width consumes much more energy (primarily due to reasons described above) compared to increasing SS. Note that since none of the current hardware supports 6 SS, we use interpolation to find its power consumption.

Findings: *Increasing SS is a more energy efficient alternative compared to doubling the channel width for achieving the same percentage increase in throughput.*

## 2.5 Interference Characterization

We now look at the details of how 802.11ac operates when operating in presence of other 802.11a/n/ac links. Note that even if an 802.11ac AP is using 80 MHz channel width, it still utilizes a 20 MHz channel inside the 80 MHz as a control channel. This channel is referred as the *primary channel*. Beacons and management frames are sent over the primary channel. The purpose of using the primary channel is twofold.

- (1) Primary channel is used to determine the channel width (20, 40, 80 or 160) in real time depending on the current interference. An Enhanced RTS/CTS protocol is used for dynamic channel width selection. The Enhanced RTS/CTS utilizes explicit message exchange for dynamic channel width selection and collision avoidance. We study this in details in Sec. 2.6.1.
- (2) 802.11a/n clients capable of operating at maximum of 40/20 MHz channels can still receive the

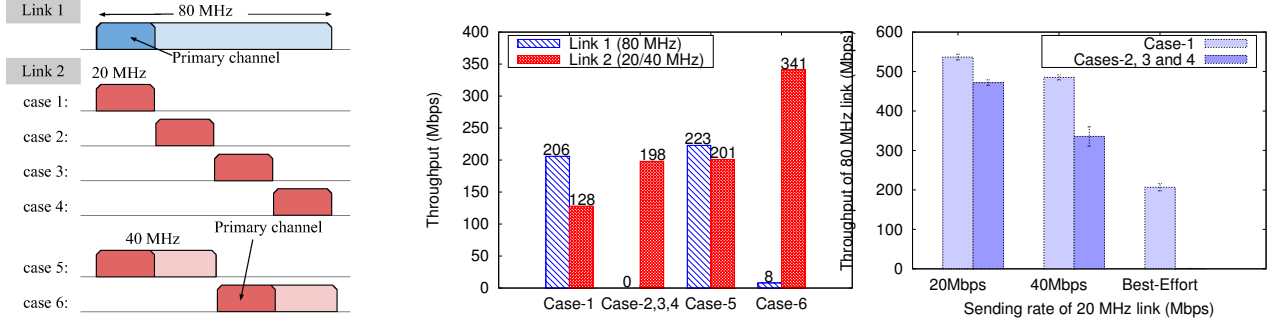


Figure 2.14. Link 1 is operating in 80 MHz fixed channel width and Link 2 is operating on 40/20 MHz width. When Link 2’s primary channel is the same as that of Link 1, both link share the medium proportionally (Case 1 or Case 5). On the other hand, when Link 2’s primary channel falls within secondary channels of Link 1, severe degradation of throughput is observed for Link 1.

beacons and connect to an 802.11ac AP. 802.11ac uses the same preamble as 802.11a/n and can detect other 802.11a/n nodes and their activity during Clear Channel Assessment (CCA).

**Indoor Setup:** The selection of primary channel and the channel widths play crucial roles in determining how the spectrum is sliced between different links. We now focus on the experiments where two links can use different channel widths and can have the same or distinct primary channels. For these experiments, we deploy two 802.11ac links indoors as shown in Fig.2.13 using Asus PCE-AC66 as clients. In order to monitor how management frames are exchanged, we use an additional laptop that is equipped with four wireless cards. All four interfaces are tuned to different 20 MHz sub-channels of 80 MHz band. Their role is to sniff the MAC frames over the air on four sub-channels. Sniffers can only sniff the management frames, and any data frame that is sent over 20 MHz channels.

### 2.5.1 Throughput Anomalies with Heterogeneous Channel Widths

Using the setup of Fig. 2.13, we fix Link 1 to operate on 80 MHz and Link 2 to operate on 20 MHz. We now consider two scenarios where both links have same or different primary channels.

**Same Primary Channel:** In the first scenario, when both 80 MHz link and 20 MHz link have the same primary channel, the resultant throughput of both the links is shown in Case-1 of Fig. 2.14(a). It can be observed from Fig. 2.14(b) that when 20 MHz channel is overlapping with the primary channel of Link 1, throughput of both the links decrease but the decrease is more or less proportional to its throughput without interference. In the other words, neither link1 nor link2 severely decreases or even gets blocked.

**Different Primary Channel:** Cases 2, 3 and 4 of Fig. 2.14(a) show the scenario when a 20 MHz

link is operating in the secondary channels of the 80 MHz link. As we can see from Fig. 2.14(b), when Link 2 is sending at best-possible rate, throughput of Link 1 becomes zero. This is surprising to see because this means that co-existence of 80 MHz and 20 MHz links can deteriorate throughput of large channel width link significantly. We repeat the experiments with 20 MHz link reducing its sending rate. The results are presented in Fig. 2.14(c). It is observed that when the sending rate of Link 2 is less (20 Mbps), the relative decrease in Link 1's performance is not significant. As we increase the rate of Link 2 (40 Mbps as shown in Fig. 2.14(c)), the performance of 80 MHz link starts degrading. Further increasing the rate of Link 2 to its maximum (Best-Effort as shown in Fig. 2.14(c)) causes complete blockage of the 80 MHz link.

We repeat the same experiments with Link 2 now operating on 40 MHz channel width (Cases 5 and 6 in Fig. 2.14(a)). As in the case of 20 MHz, when Link 2 is overlapping with Link 1's primary channel, the throughput is proportionally divided. On the other hand, if Link 2 is not overlapping with Link 1's primary channel, the throughput of Link 1 degrades severely.

*Findings: When a 20/40 MHz link is operating in secondary channels of another 80 MHz link, the throughput performance of the latter link degrades severely.*

**Causes of Throughput Degradation:** We believe that this throughput anomaly when using heterogeneous channel widths is due to two main reasons - (i) 802.11ac channel access procedure (Section 2.5.2) and, (ii) difference in CCA sensitivity thresholds (Section 2.5.3). Next, we discuss both of them in details.

## 2.5.2 802.11ac Channel Access Procedure

802.11ac supports both static and dynamic channel width access methods. In the experiments discusses above, the link is set to operate at fixed 80 MHz channel. This means that only when the entire 80 MHz channel is idle, it is possible to send any data over the link. The procedure, that is used to determine if the larger channel is idle or not, is described in Algorithm-1 (extracted from [1]).

**Smaller Sensing time for secondary channels:** From the channel access procedure of Algorithm-1, we see that primary channel performs sensing for DIFS (Distributed Inter-Frame Space) and backoff time, however the secondary channels are only sensed for PIFS (Point Inter-Frame Space) time. This way, sensing time for the primary channel is much larger than that of the secondary channels. Furthermore, once the secondary channel is sensed busy (during PIFS), the station will exit the current cycle of access, and will return back to primary channel sensing the medium for DIFS time. This is shown in Fig. 2.15. The PIFS and DIFS are calculated as Equations 2.3 and 2.4 where aSIFSTime refers to a SIFS

---

**Algorithm 1 802.11ac Channel Access Procedure**

---

1. An 802.11ac node senses the primary channel for DIFS time;
  2. **If** the primary channel is idle for the DIFS time, then the node chooses a random backoff time from its current contention window.  
**Else** go back to Step-1;
  3. During the backoff time, if the primary channel is sensed to be busy, the node freezes the backoff counter, and keeps sensing until it is idle again. When the channel is idle, it resumes the backoff counter
  4. The secondary channels are simultaneously sensed for PIFS time just preceding the end of backoff timer.
  5. **If** all the secondary channels are reported idle, the transmission is initiated immediately.  
**Else if** *channel-access == static*  
    Go back to Step 1.  
**Else if** *channel-access == dynamic*  
    Transmit using the idle 20 MHz or 40 MHz channel containing the primary channel
- 

(Short Inter-Frame Space) duration. The backoff time is a random number selected from 0 to the current contention window size multiplied with the slot time (aSlotTime).

$$\text{PIFS} = \text{aSIFSTime} + \text{aSlotTime} \quad (2.3)$$

$$\text{DIFS} = \text{aSIFSTime} + (2 \times \text{aSlotTime}) \quad (2.4)$$

The main issue with operation of Algorithm-1 is that when a secondary channel is sensed busy, instead of freezing the backoff counter of primary channel, the transmission is aborted and the cycle is re-initiated. Note that the freezing of backoff counter is indeed implemented for primary channel but not for secondary channels. This on top of smaller sensing time for secondary channel makes it very difficult for an 80 MHz link to gain access to medium and transmit. We believe that increasing the sensing time and implementing freezing of counter for secondary channels can significantly improve 80 MHz link's throughput as it requires medium access for a very small fraction of time (due to high data rate).

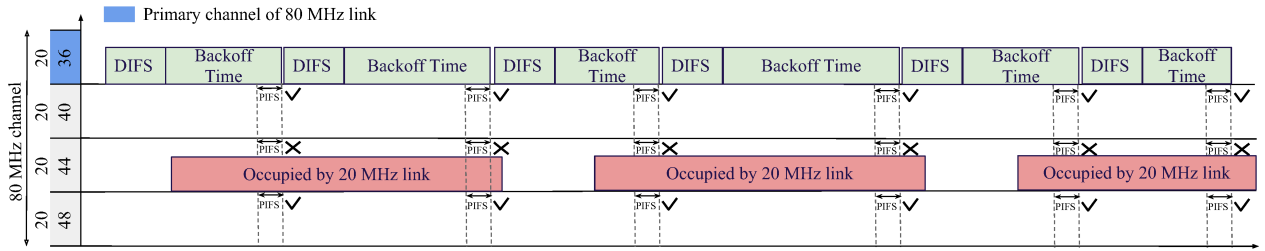


Figure 2.15. Different physical carrier sensing time and CCA methods in primary channel and secondary channels cause the 80 MHz link to continuously back off

Findings: Since backoff timer of primary channel is not frozen when secondary channels are found busy and secondary channels are only sensed for a small amount of time, a larger channel width link does not get useful medium access which results into severe throughput reduction.

### 2.5.3 CCA Thresholds

From [1], we know that the primary channel and the secondary channel use different CCA mechanisms. The primary channel utilizes a full CCA including preamble packet detection, and performs both physical carrier sensing and virtual carrier sensing. In other words, the primary channel will decode the detected PLCP (Physical Layer Convergence Protocol) preamble and use that information to set the NAV (Network Allocation Vector) counter. However, the secondary channel implements a *reduced* CCA and does not set the NAV counter.

Difference in CCA procedure and thresholds between primary and secondary channels is another reason of throughput degradation observed in Fig. 2.14(b). Since 802.11ac supports larger channel widths, it enforces much stricter requirements of CCA procedure. As before CCA in 802.11ac consists of two parts - signal detection (SD) and energy detection (ED).

Table 2.5. CCA Thresholds(dBm)

CCA mode	P-20	P-40	P-80	S-20	S-40	S-80
SD-th	-82	-79	-76	-72	-72	-69
ED-th	-62	/	/	-62	-59	-56

SD is used only when the detected channel activity is decodable (PLCP preamble detected), while the ED is used when signal can not be decoded. Furthermore, the signal detection thresholds for primary channel and secondary channel are different due to different CCA methods. We summarize the CCA thresholds used in 802.11ac in Table 2.5. In the table, P-20 refers to primary channel of 20 MHz, and

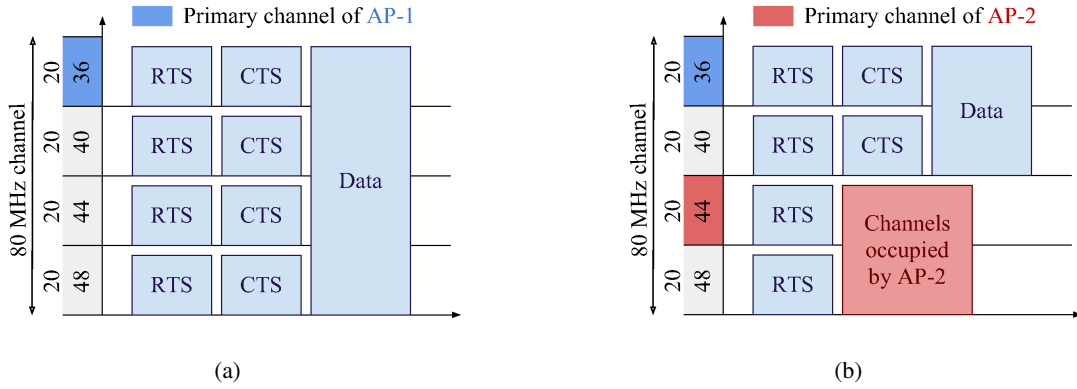


Figure 2.16. E-RTS/CTS protocol

similarly S-20 refers to secondary channel of 20 MHz. Also, SD-th denotes signal detection threshold while ED-th denote energy detection threshold.

**CCA in Cases 1 and 5:** In Cases 1 and 5, since the primary channel is overlapped, Link 1 can detect 20 or 40 MHz signal of Link 2, and similarly Link 2 can detect Link 1's signal (beacons on primary channel). This way, both the links use signal detection thresholds for CCA which results in nearly fair CSMA medium access.

**CCA in Cases 2, 3, 4 and 6:** On the other hand, when Link 2 operates in secondary channels of Link 1 (Cases 2, 3, 4 and 6), Link 2 will use energy detection threshold (-62 dBm) to perform CCA because it can not decode the signal of Link 1's 80 MHz data. However, Link-1 can decode Link 2's preamble and uses a more sensitive threshold of -72 dBm to do CCA. This will increase Link 2's chances of medium access substantially while starving Link 1. Here, we believe the CCA threshold for Link 2 in Case-2,3,4 is -62 dBm which is different with what Park said (-82 dBm) in [2]. The reason for this is that 20 MHz link can not decode 80 MHz PPDU from the secondary channel as there are not beacons.

Additionally, when the received interference power at each 20 MHz channels of the 802.11ac link is above the primary channel CCA threshold (i.e. -82 dBm) but below the secondary channel CCA threshold (here is -72 dBm), Park [2] showed the simulation results that the 20 MHz link (Link 2) will significantly back off and have an extremely low throughput. However, when we move the 20 MHz link (Link 2) away from the 80 MHz link (Link 1) which is equivalent to decreasing the received interference power for both links, we observe that the throughput of 80 MHz link gradually increasing from 0 to 400 Mbps, but the throughput 20 MHz link decreases only a little. This way, in our experiments, the significant back-off issue (as presented in [2]) does not happen. We attribute this to the difference between simulation and real-world experiments.

Findings: We showed that the larger channel accessing method and the difference in CCA thresholds does not work well when using larger and heterogeneous channel widths because it creates an unfair competition for medium access.

## 2.6 Dynamic Channel Width Access

### 2.6.1 Enhanced RTS/CTS Protocol

We consider an example as shown in Fig. 2.16 to discuss the operations of Enhanced RTS-CTS (E-RTS/CTS). First, let us consider an 802.11ac AP (AP-1) that is using channel 36 as its primary channel. When it has data to send to a client, it can use an 80 MHz channel given that the entire channel is idle for communication. If the part of the channel is busy due to other ongoing transmissions, this should be detected to reduce the channel width and avoid collisions. This is precisely the purpose of E-RTS/CTS protocol.

In this case, AP-1 will first carrier sense to see if the primary channel is idle or not. If there is any ongoing activity on the primary channel, AP-1 will defer its communication. Now, if the primary channel is idle and all the three secondary channels are also idle. Instead of sending the data directly, AP-1 first sends out RTS messages. What is interesting to note is that instead of sending an RTS message one time (as in 802.11a/b/g/n), the AP replicates the same RTS message on all four channels (Fig.2.16). When the client receives the 4 RTS messages, it interprets AP's intention to send data on an 80 MHz channel. The client follows up by detecting if the four channels are idle or not. Depending on which channels are busy or idle, the client broadcasts CTS messages. For now, let us assume that all the four channels are also idle for the client. In this case, when AP receives CTS messages on all four channels, it moves ahead by sending data on all four channels (80 MHz). Of course, when sending the data, the entire 80 MHz channel is treated as one channel and no replication of data is done.

Now let us consider the cases where there is some activity on secondary channels. If another AP (AP-2) operates using 44 as its primary channel and has an ongoing communication on channels 44 and 48. If AP-1 detects this activity, it will not send RTS messages on channels 44 and 48. This means that in ideal case, it will use only 40 MHz non-interfering band for its communication. Let us assume that AP-1 does not detect AP-2's activity but client of AP-1 does. In this case, after receiving four RTS messages from AP-1, the client will only reply back with 2 CTS messages on channels 36 and 40. AP-1 will interpret this information to send data on 40 MHz channels only. This is shown in Fig. 2.16.

By using E-RTS/CTS mechanism, sender and receiver can distributively come to a consensus on what channel and channel width to use for communication. It is worth noting that no matter what channel

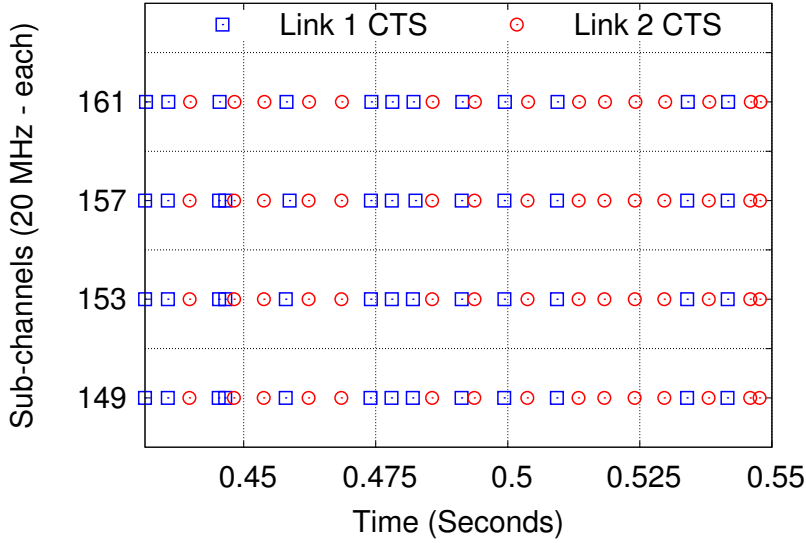


Figure 2.17. RTS-CTS packets captured by sniffer

width is used (20, 40, 80 or 160 MHz), the channel must include the 20 MHz primary channel.

### 2.6.2 Sharing or Dividing 80 MHz

To test the E-RTS/CTS protocol, we experiment with setup of Fig. 2.13. We fix the channel widths for both the links to be 80 MHz, and their primary channels to be the same.

We now send data at maximum possible rate on both the links. Fig. 2.17 shows how RTS/CTS messages are exchanged to use the 80 MHz channel. Since the primary channel is the same, both the links use the 80 MHz channel in a time divided manner. The average throughput of the links is shown in Case 1 of Fig. 2.18.

To study the impact of selecting different primary channels, we assigned different primary channels for both the links. Here, there are two possibilities where links can share the 80 MHz channel in time divided manner or they can divide the channel in two parts of 40 MHz, and use them in parallel. We observe that instead of dividing the 80 MHz channel into two 40 MHz channels, both links still use the same 80 MHz channel in time divided manner. The results of average throughput are given in Case 2 of Fig. 2.18. To further understand why sharing of 80 MHz was chosen over dividing it, we perform two additional experiments in the same settings. In Case 3, we force the links to operate on two non-overlapping and adjacent 40 MHz channels. We observe a significant degradation of throughput even though both the links were operating on two different channels. In Case 4, we repeat the same experiments but instead choose two non-adjacent 40 MHz channels. In this case, we find that throughput of

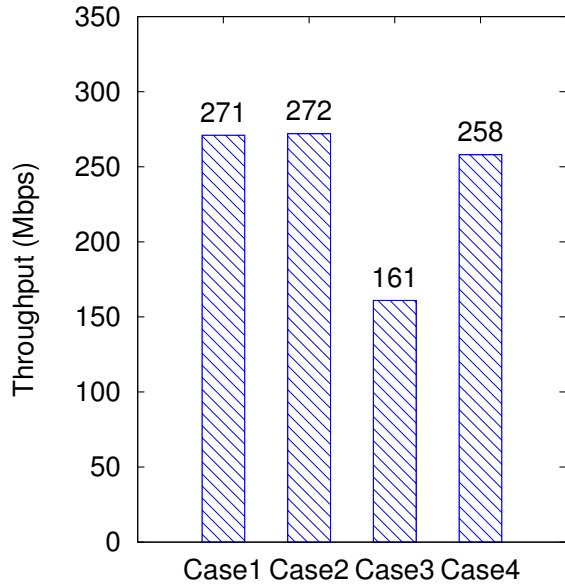


Figure 2.18. Throughput comparison of 4 cases where two links (Case-1): share 80MHz with same primary channel, (Case-2): share 80MHz with different primary channel, (Case-3): divide 80 MHz into adjacent 40MHz channels, (Case-4): divide 80 MHz into non-adjacent 40MHz channels

two 40 MHz links sum up to 80 MHz (with some difference due to overhead).

Findings: This shows that due to adjacent channel interference, it is not possible to use two adjacent non-overlapping 40 MHz channels to best of their capacity. In such case, choosing non-adjacent channels or in fact utilizing a larger channel width in time-divided manner is a better option.

### 2.6.3 80 MHz Channel Interference Pattern

In order to further understand the difference between 40 MHz and 80 MHz interference range, we setup two 802.11ac links (similar to Fig.2.13). We then increase the distance between the two links and observe how throughput is affected on both the links. The measurements are presented in Fig.2.19. As we expect, when both links operate at 80 MHz, their mutual interference reduces faster with distance. Because of this, we observe a faster increase in the throughput of both links as they move apart. However, if we operate both links on 40 MHz, the increase is slower in comparison because of larger interference range at smaller channel widths. This shows that to provide better coverage, it is better to deploy a denser network of AP when they operate on 80 MHz. Although, this denser deployment demands further complicates the interference management as there will be more neighboring cells for each AP.

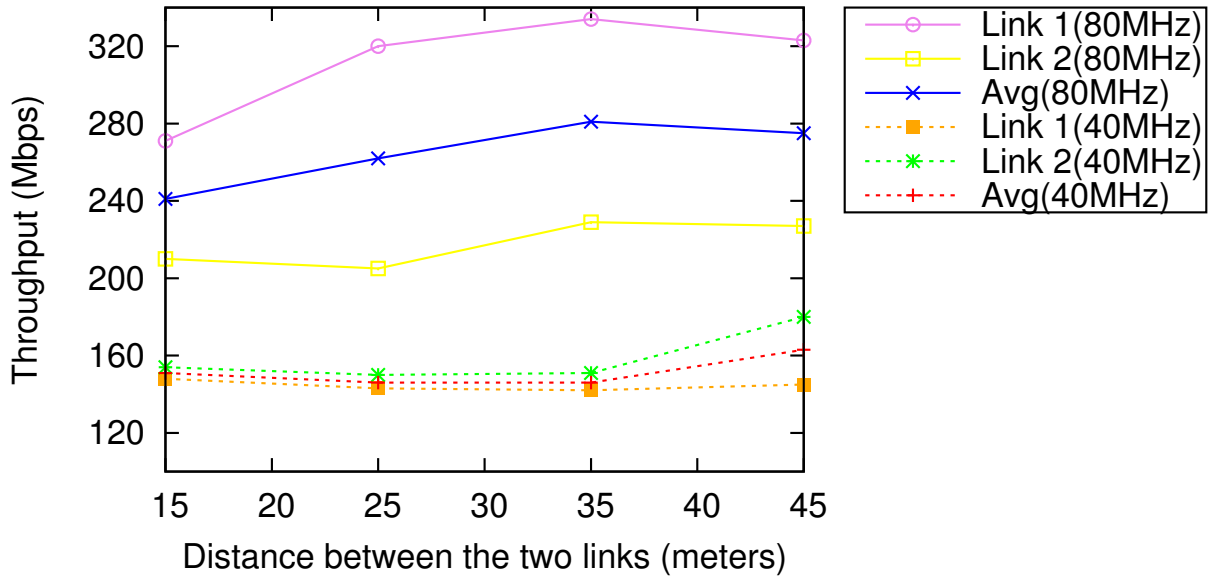


Figure 2.19. Two 802.11ac links - comparison of interference pattern between two cases, case 1 when both links operate on 80 MHz and case 2 when both links operate on 40 MHz.

## 2.7 Related Work

802.11n is the most prevalent standard used in current WLANs. Compared to other WLAN standards (802.11a/b/g), 802.11n introduced MIMO and frame aggregation as new features for throughput enhancement. Many previous research studies [22–24] provide an overview of these features of 802.11n. A detailed experimental evaluation of 802.11n is provided in [25]. It observed that throughput of an 802.11n link degrades severely in presence of an 802.11g link. Our observation about degradation of 802.11ac link performance is largely due to heterogeneous channel widths as we discussed. The work of Pelechrinis et al. [26] characterizes the influence of MIMO to the link quality. They show that MIMO highly increases the physical layer rate but produces more losses at high SNR values if packet size adaptation is not used. More recently, Kriara et al. [27] use regression analysis based on the testbed data to show that how these new features work independently to optimize the overall performance. But, all above testbed works are based on 802.11n and they didn't cover the effects and issues introduced by 802.11ac with larger channel width and denser modulation, and the coexistence between links of different channel widths.

Although some white papers [3, 4] provide an overview of 802.11ac standard, no experiment evaluation is presented. To our knowledge, our work provides first testbed based detailed evaluation of

802.11ac. Some previous research [2] has explored the benefit of dynamic channel switching in 802.11ac. However, some of their simulation results contradict what we get using real testbed. In our work, we use multiple experiments to illustrate the nature behind the throughput gain and the potential issues of 802.11ac.

In terms of power consumption characterization, Garcia-Saaverdra et al. [14] presents a new energy consumption model to measure the per-frame energy cost with higher accuracy and confidence. Halperin et al. [15] investigate the power consumption of 802.11 NICs and mainly focus on the effect of MIMO on energy cost. However, different from their work, our work focuses on the effect of larger channel width and denser modulation on power consumption of mobile devices especially for 802.11ac.

## 2.8 Summary

In this work, we presented a performance characterization of 802.11ac networks. We identified what is the impact of utilizing larger channel width on energy efficiency and interference. We showed that 80 MHz channel width yields substantial throughput improvement but the improvements come at the cost of higher power consumption. This is mainly due to higher idle mode power consumption of larger channel widths. We also showed that increasing the number of spatial streams is more energy efficient compared to increasing the channel width in achieving the same percentage increase in throughput. Also, our interference characterization showed that unplanned selection of primary channels and channel widths can severely degrade the throughput of links operating at larger channel widths. This requires that a careful interference management scheme should be designed for the success of 802.11ac. Integrating energy efficiency of mobile devices with interference management forms an important direction for future work.

# **Chapter 3**

## **Understanding Sensing Methodology: Energy Expenditure Estimation with Wearable Sensors**

### **3.1 Introduction**

Obesity is an epidemic both in the United States and all around the world. It is predicted to be the number one preventive health threat in the future [28]. Recent estimates indicate that two-thirds of U.S. adults are overweight. Poor dietary habits and lack of physical activity are two main contributors to this growing health crisis. New smartphone applications and research projects aim at helping people track their daily food intake [29] and a number of smartphone apps are available for consumer download. It is generally very difficult to know exactly how many calories people exhaust during daily physical activity as it depends on the age, gender, weight, height, type and intensity of activity.

Moderate and vigorous physical activity can lead to health promotion and disease prevention. Increased portion sizes and high caloric intake are great contributors to overweight and obesity. Provision of tools to accurately measure EEE would allow people to actively track expenditure of calories relative to the amount of calories ingested, creating awareness of personal habits that can be modified to promote personal health.

The most accurate way to measure Energy Expenditure (EE) is to use direct or indirect calorimeters, however these apparatus are not conducive to track daily intake and expenditure. COSMED K4b2 calorimeter uses pulmonary gas exchange to measure caloric expenditure with a very high correlation of 98.2% [30] but is impractical for use in daily life because of the high cost, complexity and difficulty of use [31]. Pedometers and accelerometer based approximation algorithms offer an alternative solution that is gaining popularity. Many wearable devices, such as Fitbit, Jawbone Up and Nike+ Fuelband provide a practical solution to monitor the dynamic energy expenditure by unobtrusively collecting data

Table 3.1. EEE (Cal) and step counts using commercial devices (Nike+ Fuelband and Fitbit one)

Walking type	Up	Down
Steps (Nike+)	$54.46 \pm 22.58$	$59.83 \pm 11.45$
EEE (Nike+)	$3.32 \pm 2.15$	$4.38 \pm 0.67$
Steps (Fitbit)	$61.96 \pm 20.44$	$71.38 \pm 13.18$
EEE (Fitbit)	$7.82 \pm 2.85$	$9.14 \pm 2.92$

required to make EEE. In our objective trials, we found many of these devices were accurate in step counts but inaccurate in EEE. Additionally, people need to purchase and carry these devices with them all the time to get a comprehensive assessment of energy expenditure value.

The main shortcoming of pedometers or any step-counting algorithms is their poor accuracy in detecting steps at slow speed and insensitivity to gait differences such as the length of the stride leading to unreliable estimation of energy expenditure. Another approach is to use accelerometer values directly. The existing algorithms used to estimate EE from accelerometers attempt to find an empirical relation between accelerometer data and energy expenditure data measured by a calorimeter, e.g., COSMED K4b2.

Accelerometer based algorithms have found high degrees of correlation with EEE in scenarios such as walking, running and standing. However, active lifestyle often involves climbing up or down stairs. In these scenarios, accelerometer or pedometer based approaches tend to be inaccurate. For example - in a sample trial we asked some volunteers to climb up 4 flight of stairs and then to climb down the same number of stairs. The EEE obtained using commercial products such as Fitbit and Nike+ Fuelband (which use pedometer based approach) are shown in Table 3.1. It is counter-intuitive that one will spend more calories climbing down than upwards. The algorithms used in these devices appear to count steps and speed of the movement and attribute higher expenditure based on these variables. Given that our volunteers moved faster when climbing down stairs versus up stairs these devices measured higher caloric expenditure for the less vigorous activity of climbing down versus up.

With smartphones becoming ubiquitous devices, we assert that they are the most convenient devices for EEE, rather than introducing than introducing dedicated wristbands, heart rate monitors or other tracking devices. However, work needs to be done to improve EEE accuracy using smartphone sensors. Accelerometry equations don't work well in climbing upstairs / downstairs where altitude change is involved.

New smartphones such as Galaxy S3, Galaxy Nexus, iPhone 5 and later models have an integrated barometer sensor in the phone which passively measures atmospheric pressure. Slight variations in atmospheric pressures can be detected by these algorithms to detect work done against gravity, hence improving the results. Another motivation behind our work is to develop a practical framework for EEE estimation. Existing accelerometry equations require heavy computations or require high sampling frequency, either of which will drain the battery of smartphones quickly.

The main contributions of this paper are as follows:

1. We advocate the use of machine learning techniques for EEE. We build a linear regression and multi-layer perceptron-based regression model to obtain an 89% correlation ( $\rho$ ) accuracy. We obtain high accuracy and low error (RMSE=1.07).
2. Multiple trials were conducted over 7 individuals and validated using COSMED K4b2 calorimeter. We can obtain high correlation using basic features and low sampling frequency, which will lead to battery efficiency.
3. We demonstrate that using barometer sensor, in addition to accelerometer, improves accuracy ( $\rho$  increases by 15%) without computational overhead.

Before going into the description of the methodology in details we would like to point out the scopes and limitations of our described model. First and foremost, our analysis have been built and analyzed on the basis of the most basic activities of a normal human being. The results can be extended to other physical activities like running, biking, etc. Secondly, our proposed model requires an individual to carry a smartphone at all times. This can be problematic as a smartphone may not always be carried by individuals and the sensor location will not always be known. Recognizing the activity type with a non-fixed location of sensor on the body is complex.

The rest of the work is organized as follows: Section 3.2 gives an overview of related works in this area. Section 3.3 discusses the methodology used to process sensor data from the smartphones. Section 3.4 gives a brief summary of the prediction models used in the paper followed by experimental results in Section 3.5. Section 3.6 states conclusions and discusses directions for future work.

## 3.2 Related Work

### 3.2.1 EEE Using Body Sensors

Fitbit is a highly popular commercial device which uses accelerometer and altimeter sensors to capture personal activity, a significant improvement over traditional pedometers. However, some experiments have demonstrated that Fitbit is not very accurate as it lacks activity-classification algorithms [32]. Nike+ Fuelband has the same limitations. Existing body sensor related energy expenditure estimation mostly employs a body-worn accelerometer and performs signal analysis to estimate calories expended in real-time using regression formulas. However, using a single sensor on the body is not enough to provide accurate measurement for body movement. Instead, multiple sensors are needed to improve the activity estimation performance [33].

Heart rate monitors have been used as stand-alone devices or along with accelerometer sensors to collect data and predict energy expenditure. Some devices such as Wahoo heart rate monitor, acquire heart rate data by measuring pulse rate and use a linear relationship between heart rate and oxygen uptake to predict energy expenditure. However, heart rate monitors have low accuracy during sedentary behavior and require individual calibration [31, 34].

### 3.2.2 EEE Using Smartphones

Accelerometer sensor in smartphone has been used for activity recognition in many studies like in [35]. CalFit is a widely used Android application that tracks time, location and physical activity patterns of users for health and wellness studies [35]. It uses smartphones' GPS receiver to get the location information and the accelerometer for obtaining motion data. It uses an algorithm presented in [36] to estimate energy expenditure strictly based on accelerometer data. Another previous work [37] shows how smartphones, along with GPS data, can be used to effectively calculate the EEE of individuals during biking.

### 3.2.3 Barometer Sensor and Its Application

Traditionally, the barometer sensor is used in meteorology to measure atmospheric pressure. It is also used as pressure sensor which measures relative and absolute altitude through the analysis of changing atmospheric pressure. The barometer sensor can be used for motion detection, but it is mostly used by location-based applications to evaluate elevation. Ohtaki et al. have first introduced the concept of combining barometer with accelerometer for detecting ambulatory movements [38], where authors embed a barometer sensor into a portable device to evaluate daily physical activity and classify the activity type.

### 3.3 Methodology

Our primary aim was to build an application capable of accurately providing EEE without leveraging significant computational resources on the smartphones. Low computational and power requirements will make such an algorithm more usable and attractive to consumers.

Researchers have used a sampling frequency of 10-800 Hz [39] for activity detection. However, studies have shown that 0.1-20 Hz is decent range for most human activities [40]. In this study, however, we restrict our measurements to the default smartphone sampling rate of 2Hz which corresponds to low battery consumption and processing overhead. Both accelerometer and barometer sensors are sampled at 2Hz (corresponding to 2 samples per second).

We use a window of time equivalent to 4 seconds (8 samples) to obtain different feature vectors required for our analysis. We divide these features into two basic categories: basic and derived. The basic features involve direct calculations of mean values from the tri-axis accelerometer and barometer sensor and these computations are power-efficient. The derived features are obtained from basic accelerometer data and selected from existing studies in this domain [31], which we believe will improve the accuracy of our algorithm. However, they require significant computational overhead beyond the requirements of the basic features. We also collect logistics inputs about the users and use them as feature vector in our machine learning algorithm.

#### 3.3.1 Logistics

We use subjective user information as feature vectors (FV 1-5) in our machine learning algorithm.

- *Gen*: Gender of the person (1 for male, 2 for female)
- *Age*: Age of the person in *years*
- *Hei*: Height of the person in *m*
- *Wei*: Weight of the person in *kg*
- *BMI*: Body to Mass Index of the person, calculated as division of height (squared) with weight and measured in *kg/m<sup>2</sup>*

#### 3.3.2 Basic Features

We use the following feature vectors (FV 6-9) obtained from the accelerometer sensor values over a window.

- $\mu A_x$ : Mean of x component of Accelerometer signal.
- $\mu A_y$ : Mean of y component of Accelerometer signal.
- $\mu A_z$ : Mean of z component of Accelerometer signal.
- $\mu_P$  mean of barometer signal.

The FV above are calculated easily from sensor data and are referred to as basic FVs.

### 3.3.3 Derived Features

Next, we define the additional FVs we derived from tri-axial accelerometer data. These features have been useful in human activity recognition and possibly also improve accuracy in our scenario [31]. These are termed as derived FVs (FV 10-34).

- $\mu ACA_x, \mu ACA_y, \mu ACA_z$ : absolute mean of energy deviation from average of  $A_x, A_y$  and  $A_z$  signals.  
(for example,  $\mu ACA_x = \text{mean of } |A_x - \mu A_x|$ )
- *SVM*: Signal Vector Magnitude is the root mean square value of AC component along all three axis.
- $\rho_{x,y}, \rho_{z,y}, \rho_{x,z}$ : Correlation between  $A_x, A_y$  and  $A_z$  signals (pairwise).
- $P_x, P_y, P_z$ : Pitch of  $A_x, A_y$  and  $A_z$  signals.
- $\sigma^2 ACA_x, \sigma^2 ACA_y, \sigma^2 ACA_z$ : variance of energy deviation from average energy of  $A_x, A_y$  and  $A_z$  signals.  
(for example,  $\sigma^2 ACA_x = \text{variance of } (A_x - \mu A_x)$ )
- $R_x, R_y, R_z$ : Range of  $A_x, A_y$  and  $A_z$  signals in given window.
- $E_x, E_y, E_z$ : Energy of  $A_x, A_y$  and  $A_z$  signals in given window.
- $H_x, H_y, H_z$ : Entropy of  $A_x, A_y$  and  $A_z$  signals in given window.
- $\sigma_P^2$ : variance of barometer signal.
- $Ran_P$ : Range of barometer signal (in given window).
- $mgh$ : Work done against gravity.  $mgh = Ran_P \times Wei$

### 3.3.4 Calorimetry equations

The activity counts or acceleration values collected using accelerometers can be combined with demographic information and regression techniques [36, 41] or physical models of the human body [42] to produce energy expenditure estimates. We use the popular equation proposed by [36] to obtain EEE. This model is also deployed in Calfit [35] used by researchers in California to assess associations between the built environment and physical activity in many case studies. EEE estimates given by this method uses the following heuristic relation:

$$\widehat{EEE} = aA_H^k + bA_z^m, \quad (3.1)$$

where,

- $A_H = (A_x^2 + A_y^2)^{0.5}$ ,
- $a = 0.01281 * Wei + 0.84322$ ,
- $b = 0.0389 * Wei - 0.68244 * Gen + 0.69250$ ,
- $k = 0.0266 * Wei + 0.14672$ ,
- $m = -0.00285 * Wei + 0.96828$

Researchers have reported 60-95% correlation using Equation 3.1 for ambulatory activities such as walking or running. However, the performance degrades when used for activities involving change of altitude. We use this as FV(35) in our algorithm.

### 3.3.5 Instruments

Another critical task is to measure accurate EE values. Direct calorimeter [43] requires observations in a confined metabolic chamber and is therefore impractical in our scenario. Doubly labeled water techniques are inappropriate because they calculate EE over a long duration instead of for a single activity. To calibrate exact energy expenditure values, we used COSMED K4b2 [44] indirect calorimeter, which is portable and can be used with our setup.

We used Samsung Galaxy Nexus smartphones to record observations of barometer and smartphone sensors.

## 3.4 Prediction Models

In this section, we briefly introduce the two regression models we use in this work for EEE using accelerometer and barometer data. The former is linear while the other is a non-linear model.

Table 3.2. Regression Results

Model used	$\rho$	RMSE	MAE
ANN			
Raw Accelerometer (only)	0.7189	1.6235	1.2244
All Feature Vectors (FV)	0.8794	1.1266	0.7347
Linear Regression			
Raw Accelerometer (only)	0.6028	1.8251	1.4611
All FVs	0.5807	1.8643	1.4797

### 3.4.1 Linear Regression

Simple linear regression is the least squares estimator of a single explanatory variable. It minimizes the sum of squared vertical distances between the observed responses in the dataset and the responses predicted by the linear approximation. The resulting estimator can be expressed by a simple formula, especially in the case of a single regressor on the right-hand side. If  $X$  denote the vector of inputs (obtained or derived from accelerometer and barometer readings) and  $Y$  denotes EE obtained using COSMED calorimeter,  $\bar{Y}$  denotes EEE values obtained from the model:

$$\bar{Y} = X\beta + \varepsilon, \quad (3.2)$$

where  $\beta$  and  $\varepsilon$  are constants.

### 3.4.2 Artificial Neural Networks

We use Artificial Neural Network (ANN), a non-linear, non-parametric and data driven machine learning approach in addition to simple regression technique. These non-linear techniques have been successfully used in a number of domains [45, 46] for successful prediction. Inspired by biological nervous systems, ANNs are simplified representations of the model used by human brain for intelligent functions.

The number of input layers is determined by the modality of  $X$  i.e. the number of feature vectors extracted from accelerometer and barometer data. We use one hidden layer, composed of simple elements (called neurons) and each neuron uses a non-linear transfer function to map inputs into outputs [47]. The connections between neurons largely determine the network function. One can train a neural network to perform a particular function by adjusting the values of the connections (weights) between elements. The final layer produces the ANN's output. The output of a feed-forward neural network with one hidden

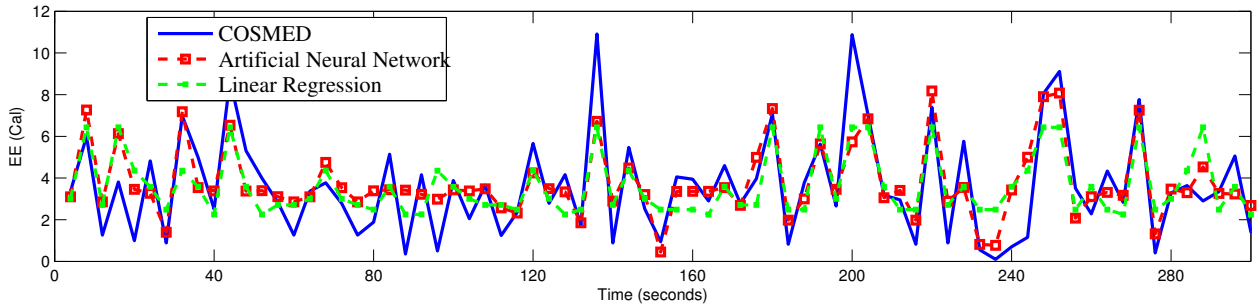


Figure 3.1. Plot of EEE using ANN and Linear Regression with actual EE values for one individual using raw accelerometer output

layer and one output neural network is given by

$$\bar{Y} = \Gamma \left[ \sum_{j=1}^{N_{hidden}} \omega_{j,o} \times \Gamma \left( \sum_{i=1}^{N_{input}} \omega_{i,j} \times X_i + b_j \right) + b_o \right]$$

where,  $\omega_{i,j}$  denotes weight between link i and j; all the inputs to a node are summed and passed through transfer function  $\Gamma$ . Input layer neurons uses *tansig* (Tan-Sigmoid) transfer function.

These functions are available for implementation as standard routines in Weka toolbox [48] and were used in this work.

### 3.5 Experiments and Results

In this section, we present our results using ANN and linear regression models on data collected from field experiments. The smartphone sensors logged their data using Androsensor app into a csv file while COSMED K4b2 calorimeter was used to validate the readings and measure actual EE. The smartphone was held in hand by the participants. For each participant, the following set of ambulatory activities were designed:

- Standing (at rest) for 2 minutes.
- Walking two laps of a 50m corridor.
- Climbing up and down on a staircase, 4 flights at a time, for four times.

Seven individuals participated in the tests. Healthy male graduate students of different ethnic background from our lab contributed to these experiments and we ran multiple trials. The range of bodily features are as follows: Weight (56-109 Kg), Height (173-184 cm), Age (22-29 years) and BMI (18-36  $kg/m^2$ ).

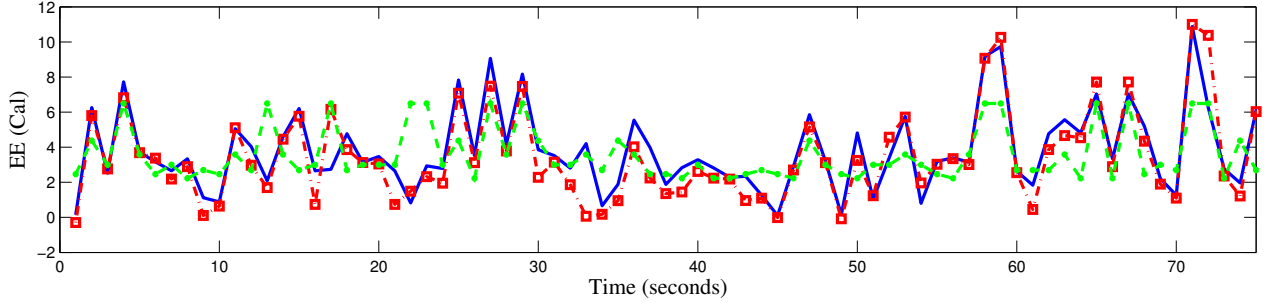


Figure 3.2. Plot of EEE using ANN and Linear Regression with actual EE values for one individual using all FVs

Table 3.3. Impact of Calorimetry Equation (CE) on ANN performance

Model used	$\rho$	RMSE	MAE
CE	0.606	1.9044	1.4634
Raw Accelerometer	0.7189	1.6235	1.2244
Raw Accelerometer + CE	0.6738	1.7642	1.3347
All FV - CE	0.8653	1.2104	0.7456
All FV	0.8794	1.1266	0.7347

We obtained all the values and then extracted the feature vectors mentioned earlier. Matlab and Weka software tools were used for computational analysis. Unlike, activity specific classification and EEE algorithms [34], our focus here is on designing a single robust EEE algorithm, that can be applied to a combination of all regular physical activities in a combined manner.

Table 3.2 gives the performance results using Artificial Neural Networks and Simple Linear Regression models.  $\rho$  indicates correlation between predicted output and actual EE values. RMSE is the Root Mean Square Error while MAE is Mean Absolute Error. Raw Accelerometer means that only the mean accelerometer values are provided as inputs to machine learning algorithm. ‘All FV’ refer to the case when all 35 FVs mentioned earlier are included in ANN.

It can be clearly seen that linear regression gives very poor performance in all cases. There is no improvement in linear regression performance with increase in Feature Vectors. Thus, the utility of using non-linear models for regression is clear. Using ANN model, we are able to achieve 72% correlation with actual EE values with a RMSE of 1.62 using only accelerometer equations. When all FVs are used, correlation increases to 88% and RMSE reduces to 1.13.

Figure 3.1 and Figure 3.2 give plots of output values using ANN and linear regression, as compared

Table 3.4. Impact of barometer values on EEE prediction using ANN

Model used	$\rho$	RMSE	MAE
Raw Accelerometer (only)	0.7189	1.6235	1.2244
Raw Acc. + Bar.	0.8326	1.2991	1.0029
All FV	0.8794	1.1266	0.7347

to COSMED values. The errors are less in ANN than by the Linear Regression model, and less in cases where more FVs are used.

### 3.5.1 Impact of Calorimetry equations

Calorimetry Equations (CE) proposed in literature, such as the one used in [35, 36] have very high computational complexity as they involve fractional arithmetic and are not feasible on smartphone processors. We want to quantify the impact of these calculations (which are otherwise accurate for walking and running) on the accuracy of ANN model. We ran the ANN model with and without this equation for both Raw Acc. and All FV models. The results are presented in Table 3.3. Using only CE gives us a correlation of 60%. It can be seen that including CE has a negative impact on the accuracy of ANN model with Raw Acc. while there is insignificant improvement with other FVs. Hence we remove this input from our selection of feature vectors.

### 3.5.2 Impact of barometer sensor

The experimental results validated our assertion that barometric sensor (Bar.) has high correlation with EEE accuracy. Appending the mean of barometer values ( $\mu_P$ ) improve the correlation of EEE to actual energy expenditure from 71% to 83% as shown in Table 3.4. However, the results can be further improved using other FVs. ‘All FV’ refer to the case when all 35 FVs mentioned earlier are included in ANN.

### 3.5.3 Influence of Feature Vectors

Extracting each feature vector from raw sensor inputs can be time consuming. Particularly, on an embedded device like a smartphone, such operations may drain the battery.

We first profile the different FV extraction algorithms in terms of their computational complexity. Since the exact speed of computation is device dependent, we report relative speed (time of execution relative to time of execution of Raw Acc. values). The values are reported in Table 3.5. These computations are performed with a desktop processor running at 2.6 GHz and averaged over 200K computations. We show relative performance trend which should scale well to mobile processors. Next, our goal is to

Table 3.5. Relative Computational Time of FV extraction step (relative to accelerometer data)

Name	Time	Name	Time
Correlation	18.7X	$\mu AC$	1.2X
Pitch	158X	SVM	0.21X
Variance	3X	Energy	0.5X
Range	12X	Entropy	0.71 X

prune the FVs with higher computational cost without sacrificing the accuracy of EEE.

We ran multiple trials and found interesting observations:

- Unlike activity classification [31], EEE accuracy is not impacted by pitch, range, axes correlation or entropy. In fact, these FVs have a negative impact on ANN performance. By removing these FVs our classifier correlation improved to 89% and MAE dropped to 0.7886. This, set of features, where we select  $\mu AC$ , SVM, energy and variance along with raw accelerometer values, is referred to as ‘Moderate FV’ in Table 3.6.
- Using only Signal Vector Magnitude and  $\mu AC$  coefficients energy along with Raw sensor values gives reasonable accuracy and low computational requirements. This case is referred to as ‘Simple FV’ in Table 3.6.

The summary of these results is given in Table 3.6. The correlation of EEE using Raw Accelerometer values increases by up to 15% using Raw barometer sensor values. Similarly, barometer sensor value impacts performance with Simple FV and Moderate FV by 21% and 24% respectively without incurring any significant computation cost. Also the RMSE values show significant improvement in each of these cases.

We are now in a position to recommend 3 ANN models for best performance tradeoffs: (1) using only accelerometer and barometer mean values, (2) adding simple FVs and (3) adding moderate FVs. The exact choice will depend on accuracy required and available computational power.

### 3.5.4 Comparison with other products

It is not possible to obtain second by second EEE from commercial devices such as Fitbit or Nike+ Fuel band. However, we did calibrate these values before and after each trial. We present the summary results in Figure 3.3. The errors in individual measurements seem to sum up and CE algorithm (calorimetry equation used in Calfit) presents an estimate which is within 25% of the COSMED values. ANN values

Table 3.6. Understanding trade-off between computational requirements and accuracy for EEE using ANN

Model used	Computation Time				% Improvement	
		$\rho$	RMSE	MAE	$\rho$	RMSE
Raw Accelerometer (only)	1X	0.7189	1.6235	1.2244	REF	REF
<b>Raw Acc. + Barometer</b>	<b>1.3X</b>	<b>0.8326</b>	<b>1.2991</b>	<b>1.0029</b>	<b>15.8</b>	<b>20</b>
Raw Acc. + Simple FV	2.2X	0.7837	1.47	1.06	9	9.5
<b>Raw Acc. + Bar. + Simple FV</b>	<b>2.5X</b>	<b>0.8726</b>	<b>1.1358</b>	<b>.8466</b>	<b>21.3</b>	<b>30</b>
Raw + Moderate FV	5.2X	0.7668	1.55	1.09	6.6	4.5
<b>Raw + Bar. + Moderate FV</b>	<b>5.5X</b>	<b>0.8909</b>	<b>1.07</b>	<b>.78</b>	<b>23.9</b>	<b>34.1</b>
All FV	194X	0.8794	1.1266	0.7347	22.3	30.6

are within 10% of the range of COSMED values. We can see that Nike+ Fuelband tends to underestimate the EE while Fitbit tends to overestimate the value. The error bars in the figure show the standard deviation for each device/ algorithm. Fitbit has an abnormally high deviation. Our algorithm has a smaller deviation over the population considered, which is comparable to actual COSMED values.

### 3.6 Summary and Future Work

In this work, we proposed usage of the accelerometer and barometer body sensors of smartphones for accurate EEE in ambulatory settings. To emulate a practical setting, we used a smartphone sampling accelerometer and barometer sensors readings at 2Hz only. We then used these values to obtain FVs and fit an ANN which can yield up to 89% correlation and RMSE of 1.07. with very small computational overhead. We observed significant benefits in fusing the input of barometer sensor to an accelerometer sensor as it allows, with use of simpler FVs, achievement of higher correlation and accuracy. The algorithm we have employed here for our prediction model, ANN, is relatively slow when it comes to building the model. However, the smartphone, will be trained using this model offline and the actual prediction in real-time will be fast and hence, not energy extensive. However, for building the model in real time, decision trees can be used.

Motivated by these strong results, we plan to collect a more extensive dataset, using a higher number of individuals, along with other physical activities like biking and running. Using this dataset, we wish to build a more representative model for EEE (using Artificial Neural Networks or other machine learning algorithms like decision trees), which will improve EEE accuracy. Another direction of future work

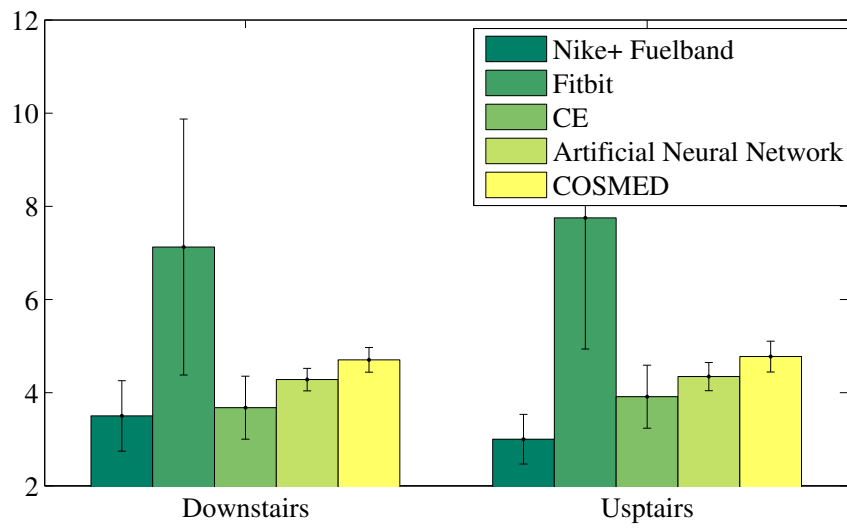


Figure 3.3. Overall absolute EE comparison of COSMED and ANN with Nike+, Fitbit and Calorimetry equation

involves building a smartphone application which can be used to accurate estimate energy expenditure of individuals by using Artificial Neural Networks, without draining smartphone energy.

# Chapter 4

## Enabling Sensing Application through 2.4/5 GHz-based WLANs

### 4.1 Fine-grained Device Motion Recognition through WiFi Signals

#### 4.1.1 Introduction

In this work, we propose APsense, a framework using which an Access Point(AP) can estimate the patterns of motion sensors of an associated smartphone. APsense, bringing the sensing capability to the AP, can classify fine-grained motion of the smartphone which is typically only available through Accelerometer, Magnetometer and Gyroscope (AMG) sensors. APsense can be implemented on off-the-shelf commodity hardware without any additional communication overhead. In order to perform fine-grained device motion detection, APsense uses (Channel State Information)CSI feedback information from the client smartphone and extracts useful features that are indicative of fine-grained motion. We show that changes in CSI feedback at the AP has a strong correlation with how observed values of AMG sensors change on the smartphone. As CSI feedback is commonly being used in newer MIMO and MU-MIMO systems, predicting fine-grained motion using CSI does not require any additional communication. Estimating how AMG sensor pattern changes can be used for many different applications such as gesture recognition and activity recognition (e.g., walking, running etc.).

The major contributions of our work are as follows:

- **Identify Motion:** First, we show that CSI feedback received at the AP from client smartphone can reflect fine-grained motion of the smartphone. We perform experiments on commodity NIC to collect CSI traces at different locations and show that it can clearly distinguish between the cases where client is stationary or has fine-grained motion.

- **Classify Different Motion Types:** Next, we demonstrate that certain features extracted from CSI can create a unique signature for different types of motion. We evaluate this using four different types of motion (described in Section 4.1.3) and observe that CSI features can uniquely identify them with simple machine learning algorithms. Based on this, we design APsense framework which consists of machine learning classifier that can learn and classify within a very short time period. Our evaluation shows that APsense can classify different motions with overall accuracy greater than 90% in certain cases.
- **Correlate CSI and Sensor values:** We then correlate the CSI feedback values to smartphone’s AMG sensors, and show that there exists a strong correlation between them. We think this is an important first step towards our ultimate goal which is to derive AMG sensor patterns using CSI feedback. Since there are plethora of applications designed on smartphone’s AMG sensors, deriving their values passively using CSI would be extremely useful. As a first step, we establish the correlation between them and leave the actual derivation to our ongoing work.

#### 4.1.2 Related Work

Sensing using the wireless signals has gained a lot of attention recently. There are multiple characteristics of the signal that can be used for the purpose of sensing motion. Received Signal Strength Indicator(RSSI), which measures the received radio signal power, has been used for the purpose in some of the recent work. Youssef et. al. [49] introduced a system that can detect and track a moving object using RSSI. More recently, Wang et. al. [50] proposed to use RSSI to predict the length of human queues in public areas. However, RSSI is a coarse-grained abstracted measure and can not be used for detecting fine-grained motion. Compared to RSSI, CSI is a much more fine-grained measure of the wireless channel. Wu et. al. [51] leveraged CSI to perform a more accurate indoor localization. Recent work such as [52] and [53] have used CSI although their work is mostly limited to detecting motion in surrounding and not applicable to fine-grained motion detection (e.g., hand gestures). Pu et. al. [54] designed a system that can recognize human gesture based on the Doppler shift of the wireless signals although such system cannot be implemented using off-the-shelf hardware.

All the above work mostly deal with device-free motion detection, while our focus in this work is different. We are interested in detecting fine-grained motion of a client device (e.g., smartphone) when it is associated with an AP. Our objective is to build a sensing framework where AP can understand client’s sensor patterns purely using wireless signals. We think that such a framework can enable a number of novel applications.

### 4.1.3 CSI and Motion

#### 4.1.3.1 CSI Background

To measure wireless signal, RSSI is considered to be a coarse-grained way which characterizes the overall attenuation of radio signals from propagation. Current WiFi standards like 802.11n and 802.11ac use Orthogonal Frequency Division Multiplexing(OFDM) in their physical layer. OFDM divides the channel into multiple subcarriers and data is sent over the subcarriers using the same modulation and coding scheme. This partitioning of the channel into subcarriers allows OFDM to combat the frequency selective fading due to multipath. Because each subcarrier is smaller than the coherence bandwidth, it suffers from independent flat fading. This way, the effect of multipath on different subcarriers can be considered more or less uncorrelated.

CSI contains amplitude-frequency response and phase-frequency response in the granularity of each subcarrier. The received signal can be modeled as

$$y = H \cdot x + n \quad (4.1)$$

where  $y$  is the received signal,  $x$  is the transmitted signal,  $n$  is the channel noise and  $H$  is the CSI which is a complex-number matrix that indicates the channel frequency response of each individual subcarrier for each spatial stream. This way, CSI for all subcarriers and all spatial streams is a  $m \times n \times w$  matrix, where  $m$  is the number of transmitter antennas,  $n$  is the number of receiver antennas and  $w$  is the number of subcarriers. Such a fine-grained matrix can accurately capture the temporal and spectral conditions of the channel and changes caused by small-scale multipath effects. Our proposed APsense framework is leveraging the aforementioned properties of CSI to recognize the fine grained motions of the receiver and further predict the sensor patterns of the receiver on the AP side.

Until recently, CSI values were not available outside the NIC firmware which made it difficult to use it for any other application. Recently, Harperin et. al. [55] developed firmware and driver support for Intel 5300 802.11n NIC that can extract Channel Frequency Response (CFR) in the format of CSI from off-the-shelf commercial hardware in kernel/user space. We use their tool in our work. Note that although 802.11n utilizes 56 subcarriers in a 20 MHz channel, the CSI tool [55] reports 30 values for 30 groups evenly spread over the 56 subcarriers. This way, CSI for one spatial stream is a vector

$$\mathbf{H} = [H_1, H_2, \dots, H_{30}] \quad (4.2)$$

where  $H_i$  represents the  $i$ th subcarrier group.  $H_i$  is a complex number representing both amplitude and

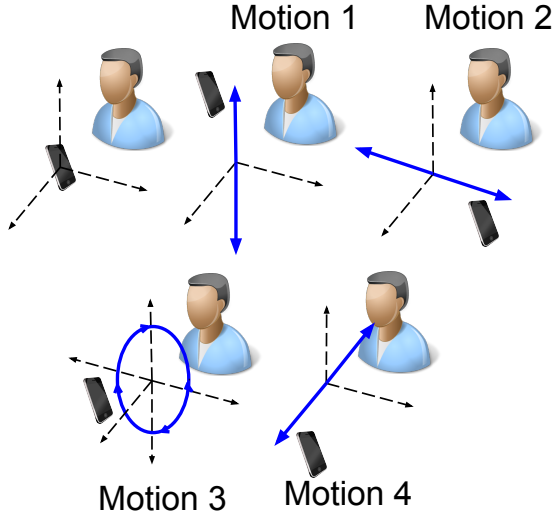


Figure 4.1. Different type of hand motions studied in APsense

phase responses as follows

$$H_i = | h | e^{jp} \quad (4.3)$$

where  $| h |$  is the amplitude and  $p$  is the phase.

#### 4.1.3.2 Experimental Settings

We use CSI tool [55] enabled on Intel 5300 802.11n NIC with three external antennas as the receiver to collect the CSI data which will be eventually available on the AP side through the feedback information. In order to understand the relationship between CSI changes and motion patterns, we attach a Shimmer [56] device at the center of the external antennas. The Shimmer device has accelerometer, magnetometer and gyroscope sensors, and we collect their values to establish ground truth in our comparison. To check if CSI can classify motions or not, we try four separate hand movements as shown in Fig. 4.1. Albeit simple, these motions can be combined to generate many other complex gestures. In our experiments, the client stays at the same location, facing towards the AP in a line-of-sight link. We repeat each motion 50 times while collecting both the CSI and Shimmer sensor data. The CSI is collected at a rate of 10 samples per second for a more tractable analysis, while the Shimmer data is collected at 100 samples per second for higher accuracy in understanding the motion type. The same experiments are repeated for a case where the client device is stationary in order to establish a base line for comparison. We also repeat the experiments at four different indoor locations. In order to reduce the impact of excessive multipath in our experiments, we perform the experiments at night time with nearly no movement of surrounding

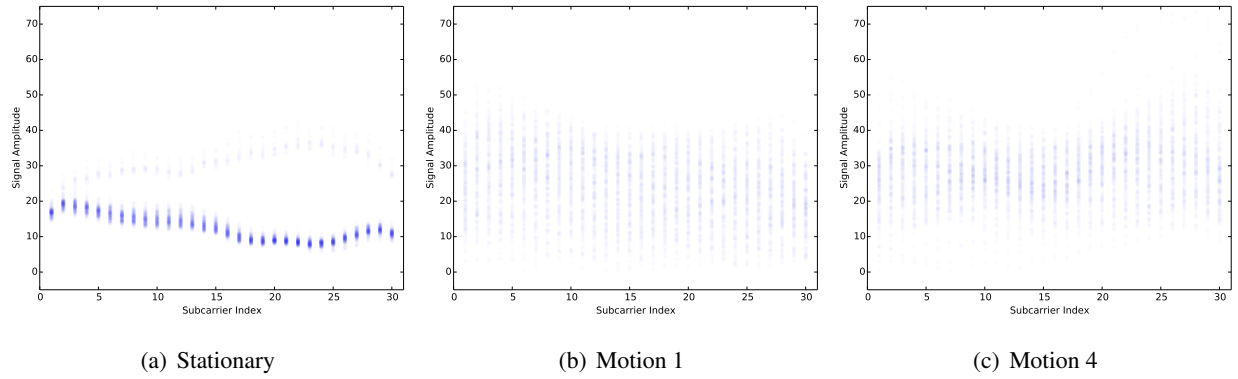


Figure 4.2. Density Distribution of CSI amplitude in each subcarrier for a 30s trace where client is in different motions. The x axis is the subcarrier index from 1 to 30 and the y axis is the CSI amplitude.

objects.

#### 4.1.3.3 Identifying Motion Using CSI

Now we take a look at how fine grained motions can affect CSI. Our observation is that the multipath changes due to small motion affect individual subcarriers and each subcarrier suffers from uncorrelated flat fading. Also, we observe that different subcarriers are affected in different ways for different motions. To demonstrate this, we collect CSI traces for three cases - device is stationary, motion 1 and motion 2 (Fig. 4.1). Fig. 4.2 shows the observed CSI amplitude density distribution for each subcarrier within a 30 seconds' trace. As we can see in Fig. 4.2(a), in the case where there is no motion, the amplitude values are much more concentrated. On the other hand, Figs. 4.2(b) and 4.2(c) shows that in the case of motion, the CSI amplitude is much more dispersed. Comparing Fig. 4.2(a) with Figs. 4.2(b) and 4.2(c) shows that CSI can clearly identify if the device is stationary or in motion. Furthermore, the pattern of dispersion in Figs. 4.2(b) and 4.2(c) is noticeably different which tells us that a closer look at the CSI values can in fact classify different types of motions as well.

#### 4.1.3.4 Classifying Motions using CSI

We now know that CSI can identify whether or not the receiver is in motion. Next, we take a step further to see if CSI can also be used to classify different types of motion. Before doing rigorous feature extraction, we first calculate some obvious yet important statistics about the subcarrier-level information available in CSI. We first divide the CSI data in time windows of  $t$  seconds and calculate different statistics for each time window. As an example, we calculate the mean of amplitude of 30 subcarriers at for all samples in a time window and find the 90th percentiles of the mean values. Intuitively, this should reflect the upper limit of mean values in the time window without considering the impact of outliers.

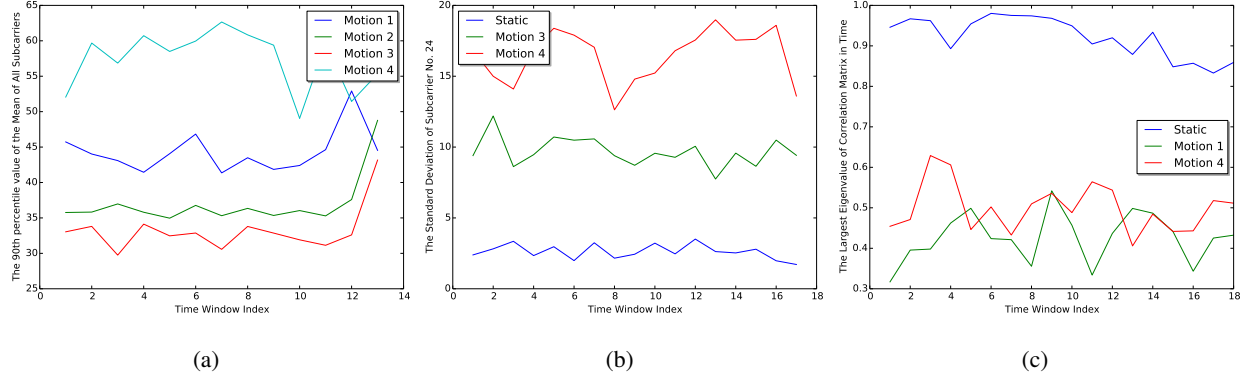


Figure 4.3. Comparison between different CSI features for different types of motions

As shown in Fig. 4.3(a), the 90th percentile of mean values is noticeably different for different motion types. This is because different motion has different effect on the maximum amplitude of all subcarriers. Next, we take a look at a specific randomly chosen subcarrier and calculate the standard deviation of its amplitude values in given time window. As shown in Fig. 4.3(b), we observe that this value can be used to distinguish between static case, motion 3 and motion 4. Note that although the same value can not be used for classifying motions 1 and 2, we see that the same statistic about other subcarriers can be used for that purpose. Next, we determine a more comprehensive set of features that we use for motion classification.

To find a more complete set of candidate features, we derive statistics in both time and frequency domains based on the raw CSI data. We use two sets of features - features for individual subcarrier and features across all subcarriers in a given time window.

- **Features for individual subcarrier:** We calculate the following features using CSI amplitude value in each time window.

- Mean/Median - Measuring the static component of CSI amplitude with different motions' impacts
- Min/Max/Range - Measuring the changing range of CSI amplitude
- Standard Deviation - Capturing the fluctuation level with in each time window
- Percentile at 10% / at 90% - Measuring the CSI amplitude range without potential outliers.
- Normalized Energy - Capturing periodic changing patterns caused by different motion. Here, we use FFT to calculate the samples in frequency domain.

- Normalized Entropy - Measuring the degree of disorder using the frequency domain samples
- **Features across all subcarriers:** To calculate a feature across all subcarriers, we first calculate its value for a specific CSI sample. We then take various statistics of that over the time window where there are many different CSI samples. For each feature calculated over all subcarriers, we calculate its mean, min, max, range, standard deviation, skewness and kurtosis over the time window.

In addition, to have a overall comparison in each time window, for each time window  $T$ , we can get the following matrix across subcarriers

$$\mathbb{H} = [\mathbf{H}_1^T, \mathbf{H}_2^T, \mathbf{H}_i^T, \dots, \mathbf{H}_T^T] \quad (4.4)$$

where  $\mathbf{H}_i^T$  is a vector of length 30 and includes the CSI amplitudes of all subcarriers for  $i^{th}$  time sample. After calculating the correlation matrix between  $\mathbf{H}_i^T$  and  $\mathbf{H}_j^T$ , we can obtain the largest and the second largest normalized eigenvalues as the other two features for CSI [53]. As described in [53], larger values of these two features indicate lesser or no motion. This can be seen in Figure. 4.3(c) which shows the largest eigenvalues of different motions.

Similarly, we also obtain the following matrix across time between individual subcarriers

$$\mathbb{S} = [\mathbf{S}_1, \mathbf{S}_2, \mathbf{S}_i, \dots, \mathbf{S}_{30}] \quad (4.5)$$

where  $\mathbf{S}_i$  is vector of length  $T$  and includes all the CSI amplitudes for  $i^{th}$  subcarrier in this time window. We also get a correlation matrix by calculating the correlation between  $\mathbf{S}_i$  and  $\mathbf{S}_j$ . Then, we obtain the largest and the second largest normalized eigenvalues of the correlation matrix and use them as the features for CSI.

#### 4.1.4 APsense

In this section, we introduce APsense, our framework that uses CSI feedback at the AP to recognize the fine-grained motion of the associated clients. As we mentioned before, the ultimate goal of APsense is to estimate the sensor reading patterns (e.g., accelerometer) of the clients. Such CSI-based sensing of client's sensors on AP side can enable numerous new applications without requiring any additional message overhead. In this work, we have focused on classifying different motions as a first step towards it.

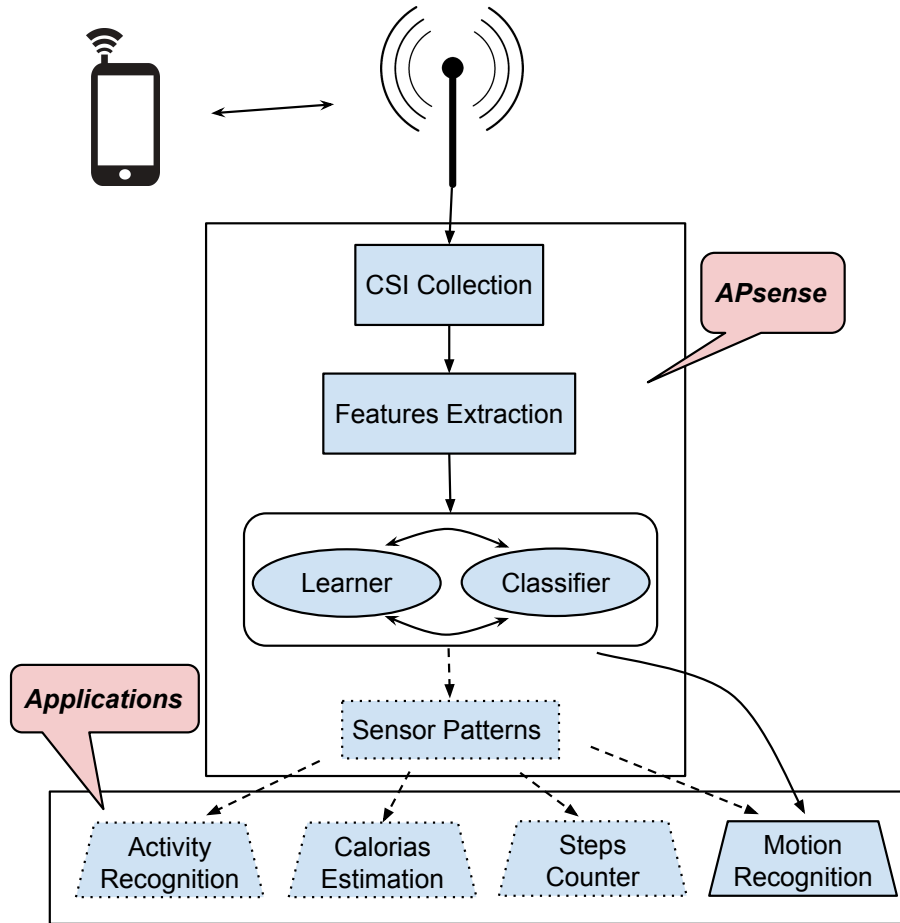


Figure 4.4. APsense Architecture

#### 4.1.4.1 System Overview

The architecture of APsense is shown in Fig. 4.4. Here, the AP first collects the CSI information from the client smartphone. It then extracts useful features from raw CSI data as shown in Section 4.1.3.4. These features are then used by machine learning module that can learn and classify different motions. In the future, we plan to extend our system where machine learning module can recognize/classify sensor patterns (dotted boxes in Fig. 4.4) which can then be used for a number of different applications.

To learn and classify different motion based on CSI features, we use two commonly used supervised machine learning techniques - *Naive Bayes* and *Decision Tree*. We choose these two methods because they can handle non-linear nature of the features and their inter-dependencies. Also, decision tree can output simple if-else classification models that are useful in understanding the importance of different CSI features. We plan to use other more complex and customized classifiers in the future.

Table 4.1. APsense Motion Recognition Results at Different Locations - TP Rate

Method	L1	L2	L3	L4	Combined
Naive Bayes	0.927	0.783	0.859	0.738	0.568
Decision Tree	0.938	0.774	0.815	0.786	0.748

Note that current design of APsense requires a small amount of client feedback for training the classifier. Here, the client device can provide the motion type to the AP along with the CSI data for some initial samples. Once the classifier model is built, it can then classify motions purely based on the CSI data.

#### 4.1.4.2 Performance Evaluation

As explained in Section 4.1.3.2, we evaluate APsense at four different indoor locations. Table 4.1 shows the true positive rate of both machine learning methods for all four locations. Here, true positive rate is defined as the fraction of instances correctly classified as motion type X out of all instances actually belonging to motion type X. As we can see, both the machine learning methods can very well classify different motions at all four locations. The classification accuracy is much higher (93.8% and 85.9%) for locations L1 and L3 because both the locations have much richer multipath environment compared to locations L2 and L4. We also combine instances of all the locations and perform a single classification across the locations. This is to evaluate how well our classification can work when the model is trained at a specific location. We observe in Table 4.1 that overall classification accuracy drops (especially for Naive Bayes) in the combined case. This shows that APsense can achieve higher accuracy if the model is trained using location specific CSI profile.

Next, we take a look at the detailed results of combined locations case in Table 4.2. Here, precision is defined as ratio of number of true positives to the total number of true positive and false positives. The ROC (Receiver Operating Characteristics) area is the area under the curve when plotting FP rate versus TP rate. We can see that stationary case and motion 4 have a very high TP rate, while motions 1, 2 and 3 are often mis-classified reducing their TP rate. We believe that this is due to nature and directions of the motions. As shown in Fig. 4.1, motions 1, 2 and 3 are along the same X-Y plane, keeping the distance same from the AP. On the other hand, in motion 4, the motion is towards and away from the AP.

The size of the time window over which we calculate the CSI features is an important factor. The above results are presented for the time window size of 5 seconds. We now experiment with changing the size of the time window to see its impact. Fig. 4.5 shows the comparison of TP rate for different

Table 4.2. Detailed Analysis for Combined Locations Case

Motion Class	TP Rate	FP Rate	Precision	ROC Area
Static	0.989	0.007	0.978	0.997
Motion 1	0.592	0.079	0.646	0.892
Motion 2	0.614	0.072	0.672	0.920
Motion 3	0.625	0.098	0.580	0.891
Motion 4	0.848	0.054	0.778	0.969
Average	0.748	0.059	0.746	0.938

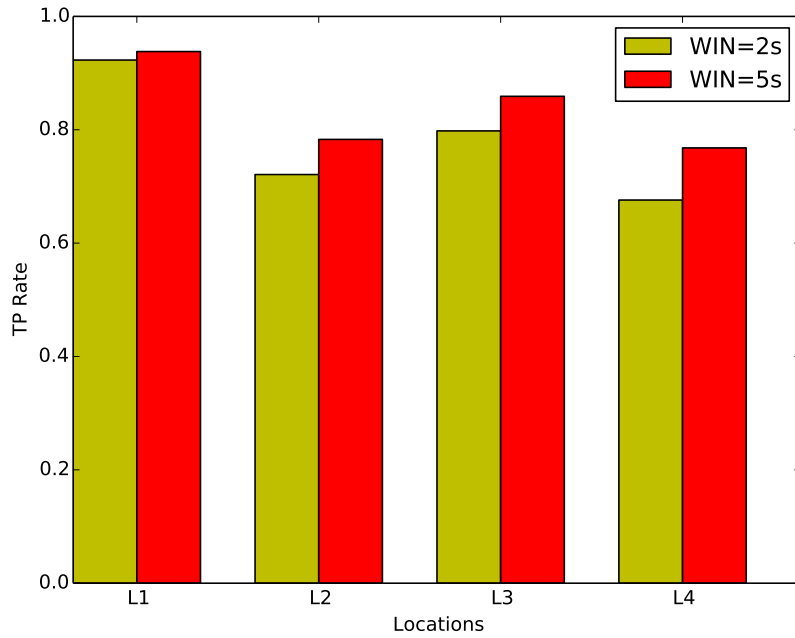


Figure 4.5. TP Rate comparison with different time window sizes

locations with time window size of 2 and 5 seconds. We observe that larger time window size provides better classification accuracy for all locations. This is mostly because more number of CSI samples are available for calculating features in the case of larger window size.

#### 4.1.4.3 Correlating CSI and Sensor values

In our ongoing work, we plan to extend APsense such that it can estimate the client's sensor pattern using the CSI data. To test the feasibility, we calculate different features of Shimmer sensor data collected in our experiments (Section 4.1.3.2). We then calculate one-on-one correlation of these features with CSI features. Intuitively, if these features are correlated to each other, it means that we can use the CSI data to derive how the sensor data changes. Fig. 4.6 shows the correlation coefficient for different pairs of

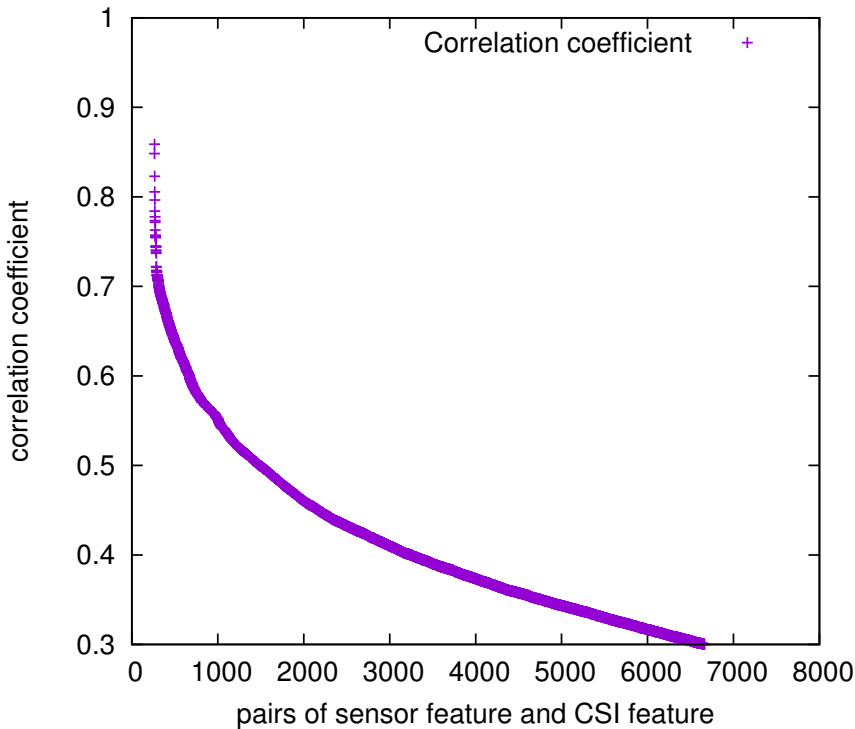


Figure 4.6. Correlation between sensor and CSI features

CSI and sensor features. As we can see, a large number of pairs show a very high correlation which tells us that we can use the CSI features to derive the sensor patterns.

#### 4.1.5 Discussion and Conclusions

In this work, we showed that CSI data can be used to determine client's fine-grained motion at the AP. There are multiple challenges in APsense as it evolves in our ongoing work. First, it is expected that motion detection accuracy would decrease when the surrounding environment has many moving objects and the resultant multipath is severe. Our current experiments were done in a controlled environment with mostly stationary surroundings. We are addressing these challenges as part of our ongoing work. Second, since CSI samples are available only when actual frames are sent, it would become challenging to detect motion when available number of CSI samples are sparse. Revising the CSI features for fewer samples such that motion detection accuracy is still high is also an interesting direction of future work.

## 4.2 Analyzing Shopper's Behavior through WiFi Signals

### 4.2.1 Introduction

Analyzing shopper's behavior in retail stores and shopping malls can provide crucial insights in a variety of aspects such as browsing habits, shopping interests etc. These insights can be useful to the business

owners in improving the recommendations, services and effectiveness of promotions. Such tracking and analysis of a shopper in a retail store is referred as physical analytics. Compared to online shopping where user’s navigation patterns and other characteristics can be easily recorded, analytics in physical domain has received comparatively low attention in research. The complexity of physical analytics arise from many challenges. Simply relying on video surveillance to understand shopper’s behavior is not scalable, given that deployment of video cameras and mining the video stream to extract information can have very high cost along with some serious privacy implications.

Recent works [57,58] have proposed to use a user-driven approach where inertial sensors and camera available on shopper’s wearable devices are used for physical analytics. However, this approach requires the shoppers to carry such devices and also effectively communicate the acquired information to the business owner. Relying on store’s infrastructure for sensing shopper’s behavior is a preferred way to enable non-intrusive monitoring. Shopper localization using RF signals [59–61] or Visible Light Communication (VLC) [62] is an attractive alternative but it requires the shopper to actively engage in the process (e.g., connecting to store WiFi or exposing the smartphone camera to LED luminaires). Since many shoppers can choose not to participate in the process, it is difficult to enable accurate physical analytics using such methods. This motivates the need of a passive, non-intrusive, device-free, low-cost and privacy-preserving form of sensing shopper’s behavior for accurate physical analytics.

In this work, we propose to utilize WiFi signals for understanding shopper’s behavior in retail stores. WiFi is an attractive choice due to its pervasiveness in shopping malls, super-markets etc. Although the primary purpose of the WiFi deployment is to provide low-cost internet access, we show in this work that it can provide an efficient and accurate way of sensing shopper’s behavior. There has been a considerable amount of work in indoor localization using WiFi, and our system proposes to further extend the sensing through WiFi by identifying and classifying shopper’s activities. The proposed system does not require the shopper to carry any device as the movements of the shopper is detected purely by observing the variations in CSI of WiFi. It is also low-cost as the retail store owner does not require any infrastructure other than WiFi for observing shopper’s behavior. Depending on where a WiFi link is deployed, it can sense different shopper’s activities. For example, when deployed close to the entrance, our system can monitor if a shopper is entering or leaving the shop. Additionally, our presented way of using WiFi requires no modifications to off-the-shelf commercial WiFi hardware. We identify different states of a shopper in retail store and categorize them in two types of location in a retail store: (1) near the entrance (2) inside the store. It is then shown that each of the state exhibits a unique CSI signature which allows

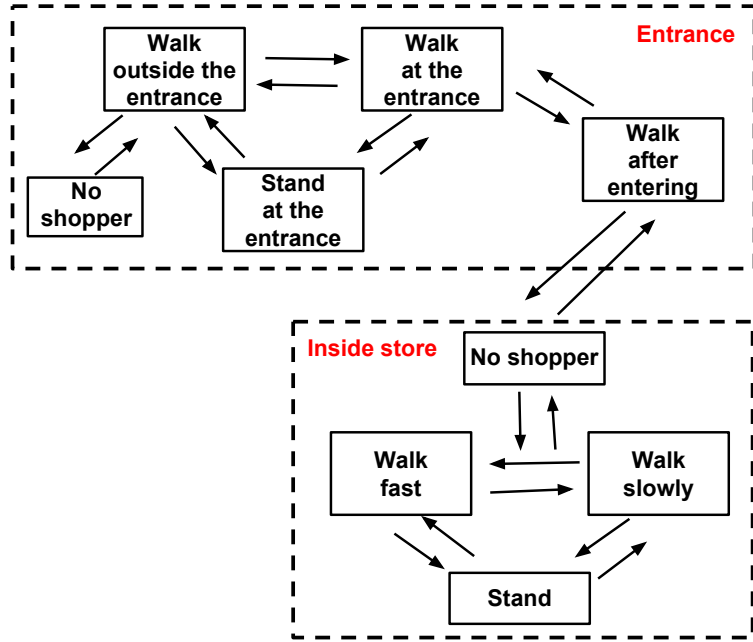


Figure 4.7. Shopper's states transition diagram

us to detect that a shopper is in a given state. Our experimental evaluation indicates that different states of a shopper near the door and inside the store can be classified with 90% and 96% accuracy respectively.

#### 4.2.2 Motivation

Accurate physical analytics entails analyzing shopper's behavior while meeting some important design goals. Improved understanding of the behavior will allow the brick and mortar stores to compete with the online stores by providing better service. For in-store analytics, it is necessary to answer various questions about shopper's behavior. The questions include how long a shopper remains in the store? How long the shopper stands at the entrance and looks at the advertisement board? What's the reaction of the shopper after looking at the advertisement board? Is the shopper entering or exiting the store? Is the shopper walking fast (with purpose, knows what she wants) or slowly (browsing)? The answers to these questions should be obtained while meeting the following requirements.

1. **Non-intrusive:** The shopping experience for the shopper should be as distraction-free as possible. This means that minimum input and interaction are expected from the shopper, and increasing reliance on passive monitoring is preferred. Such a requirement rules out techniques where user has to connect to a WiFi network or actively answer survey questions about her present state.
2. **Device-free:** An accurate estimation of shopper's behavior should not require her to wear/carry

Table 4.3. Shopper's behavior around the entrance

Shopper's state	Inferred activity	Useful in determining
Walking outside the entrance	Preparing to enter the store	Effectiveness of promotions outside the store
Walking at the entrance	Entering the store	Estimating store occupancy
Standing at the entrance	Observing close-to-entrance promotions	Effectiveness of in-store promotions like flyers etc.
Walking inside the store	Proceeding towards aisle of interest	Effectiveness of in-store arrangements

Table 4.4. Shopper's behavior inside the store

Shopper's state	Inferred activity	Useful in determining
Walking fast	Walking towards pre-decided item	Opportunity for offering discount, additional items
Walking slowly	Browsing items of interest, exploring new items	Opportunity for advertisements, promotions
Standing	Closely observing item(s)	Factors affecting shopper's choice

any devices such as smartphones or smartglasses. Relying on shopper's devices can introduce significant inaccuracies as shopper may not carry or use the devices as expected for physical analytics. Previous approaches like [57] assume that the shoppers wear such devices, however, in this work, our focus is to design a device-free technique for physical analytics.

3. **Low-cost:** It is always desirable that the physical analytics technique is low-cost and can reuse the existing infrastructure with minimum configurations and maintenance.
4. **Privacy-preserving:** The information made available through the use of analytics should not lead to privacy leakage for shoppers. For example, using video surveillance can reveal shopper's identity along with her behavior. Any such technique should be avoided to protect shopper's anonymity.

We show in this work that WiFi-based physical analytics can satisfy the aforementioned requirements. Given that most retail stores already have available WiFi infrastructure, our system does not incur any additional cost since it does not require any additional infrastructure. It purely relies on the changes in multipath observed through CSI variations to determine shopper's fine-grained behavior. Our system needs zero effort from the shopper and is implemented on the off-the-shelf commercial hardware. Since the WiFi signals can not be used to track the shopper's identity, it protects shopper's privacy without losing the functionality to capture shopper's behaviors in an anonymous way.

#### 4.2.3 Understanding Shopper's Behavior

During a typical visit to a retail store, a shopper enters the store, purchases the intended products and leaves. This behavior can be further classified into fine-grained states as shown in Fig. 4.7. Each state

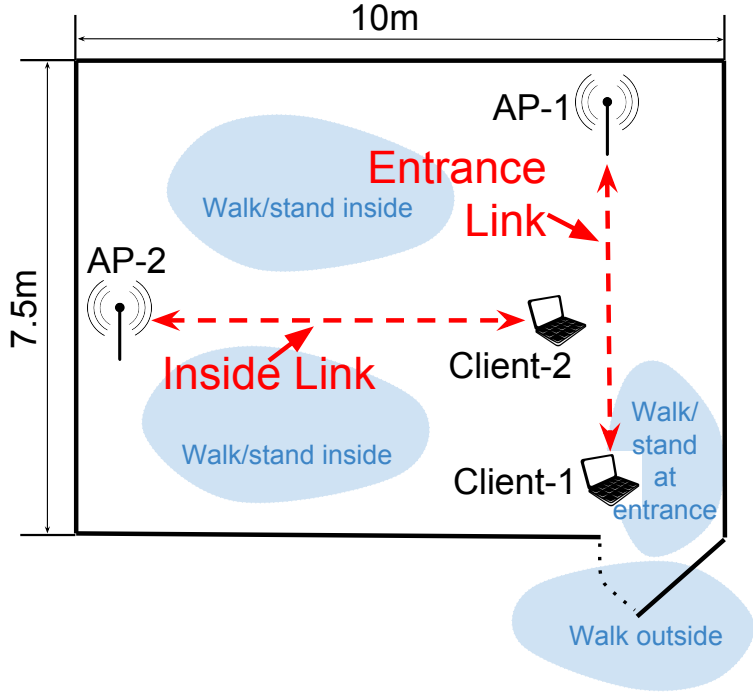


Figure 4.8. Experiment layout

of the shopper can be used to infer an activity related shopper's behavior. This mapping between the states and the inferred activities is shown in Tables 4.3 and 4.4. The tables also describe how the inferred activities are useful in analyzing various aspects of business strategies and feasibility of improvements. For example, for shopper's behavior near the entrance, determining the amount of time spent by a shopper walking outside the entrance can be an indication of the effectiveness of the promotions outside the store. Similarly, detecting that a shopper is walking fast inside the store means that she is walking towards known pre-decided items.

The characteristics of shopper's behavior includes not only the current state of the shopper but also how the shopper traverses through multiple states to accomplish what is intended in the visit to the retail store. This means that it will be useful to detect the transitions in shopper's state for a complete view of the behavior. In this work, we show how different states of a shopper (as shown in Fig. 4.7) can be determined using CSI. We will demonstrate how CSI variations can be used to fingerprint shopper's behavior with a very high accuracy. We note there can be many more fine-grained states of a shopper (such as fetching an item, checkout etc.) beyond the ones considered in this work. However, our objective in this work is to demonstrate the feasibility of WiFi based shopper behavior analysis for which we use fewer yet representative states.

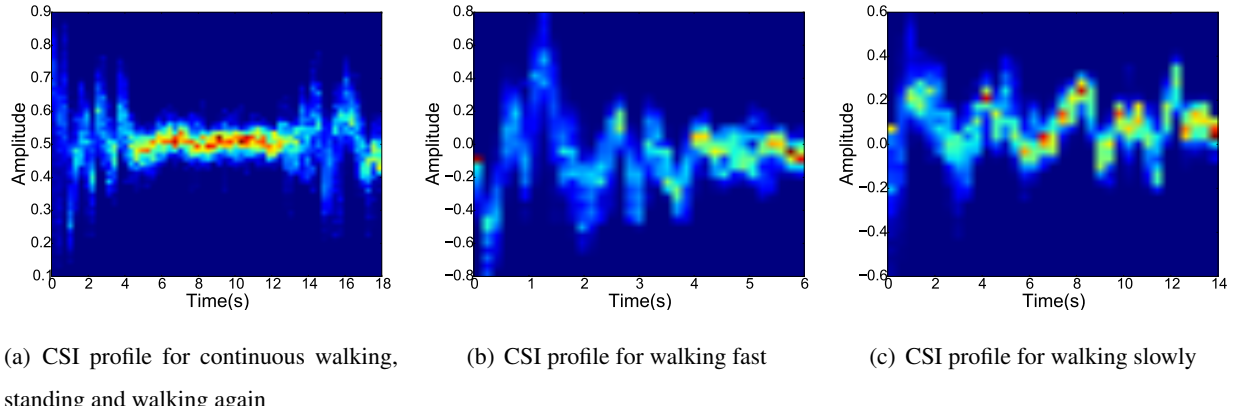


Figure 4.9. CSI profiles when a shopper performs different activities

#### 4.2.4 Analyzing Shopper’s Behavior Using CSI

##### 4.2.4.1 Experiment Setup

We implement our WiFi-based shopper behavior analyzing system using off-the-shelf commercial WiFi devices. Asus RT-AC66U WiFi router with 3 external omnidirectional antennas is used as the AP which operates in IEEE 802.11n mode in 2.4 GHz band. The WiFi client connecting to the AP is a Dell laptop with Intel 5300 802.11n WiFi NIC and 3 external antennas. We choose a large conference room in a university building to emulate a retail store scenario. Since in a typical large retail store, there can be a substantial distance between the entrance and the aisles, the “entrance” and the “inside store” scenarios use separate WiFi links as shown in Fig. 4.8. Note that in our setup, the experiments are done only on one link at a time to avoid interference.

For the collection of CSI, the client pings the AP at 100 packets per second and the CSI is collected at the client side from the modified driver [55]. Since any WiFi link observes different static multipath depending on the location of endpoints, CSI profile for different shopper activities will be slightly different at different locations. This means that the training procedure has to be repeated for each new location of the WiFi endpoints.

##### 4.2.4.2 CSI Processing

In a stationary environment without any user movements, the CSI data captured between the two endpoints profiles the static multipath of the environment. When a shopper walks within the range of the link, the variations observed in the CSI can be used to profile how the shopper moves. However, it is challenging to create a unique signature of shopper’s activity purely using the raw CSI data. This is because the raw CSI data contains a variety of noise introduced by the surrounding and high-frequency

movements. In order to distill the underlying impact of the shopper's state, it is first necessary to remove the high-frequency noise from the raw CSI data. Since majority of the human activities exhibit lower frequencies [63], we use a band-pass filter with cut-off frequency of 2 Hz and 0.3 Hz to remove the high-frequency noise as well as the static component.

In order to understand how filtered CSI data can distinguish between different shopper's state, we perform two separate experiments. In the first experiment, a user is asked to walk, stand and walk again while the CSI is being captured. Fig. 4.9(a) shows the filtered CSI data for the experiment. Large CSI variations (with alternating peak-valley) are observed when the shopper is walking, while relatively smaller variations are observed during the time when the shopper is standing. In the second experiment, the shopper is asked to walk fast and slowly for a fixed distance on a given path. The filtered CSI profile is shown in Figs. 4.9(b) and 4.9(c). Apart from the time taken to complete the walking, a simple visual inspection (amount of signal variation, number of variations cycles) can distinguish between the two types of walk. This shows us that CSI signal profile can be used to determine shopper's state and infer her activities for physical analytics.

To differentiate between different activities of the shopper using CSI, we calculate various statistical features from the CSI data and create CSI profiles of the activities. A sliding window based approach is used with 3 seconds window size, moving over the time-series CSI data at an interval of 1 second. The features are calculated for each of the 3 seconds windows. These features are adapted from the feature set used in activity recognition through motion sensors (e.g., accelerometer, gyroscope) [63]. We next describe some of the notable features we have used in our analysis.

- Mean/Absolute-mean/Max/Min/Median/Quartiles: We calculate these basic statistics after a band-pass filter with a cutoff frequency range with 0.3 Hz to 2 Hz. These features can describe the shape and the distribution of CSI amplitude in each time window.
- DC-Mean/DC-Area: After a lowpass filter with a cutoff frequency of 1 Hz, we calculate the mean and the sum of all amplitude. The DC band features can provide the static component in current environment which can be used to infer shopper's body posture.
- Variance/Range/Mean-crossing-rate: They can provide us the variation and fluctuation level of the CSI amplitude changing in the time domain.
- Skewness: Measuring the asymmetry of the CSI amplitude distribution.

- Kurtosis: Measuring the peakedness of the CSI amplitude distribution.
- Normalized-Entropy ( $H$ ): It measures the disorder of the CSI amplitude samples in frequency domain. Let  $N$  be the window size and  $V_i$  be the normalized FFT coefficients, then  $H$  is calculated as

$$H = - \sum_{i=1}^{N/2} V_i \cdot \log_2 (V_i) \quad (4.6)$$

- Normalized-Energy ( $E$ ): It measures the sum of energy without the DC component in the frequency domain. Let  $N$  be the window size and  $V_i$  be the normalized FFT coefficients, then  $E$  can be calculated as

$$E = \sum_{i=1}^{N/2} V_i^2 \quad (4.7)$$

- FFT-Peak: Selecting the largest FFT coefficient without the DC component. It can reflect the dominant activity frequency in the current window.
- Dominant-Frequency-Ratio: We divide the largest FFT coefficient by the sum of all FFT coefficients. It can reflect the ratio of the dominant frequency to the sum of all frequencies.

As mentioned before, our CSI-based sensing of shopper's behavior is highly dependent on the static multipath profile. This means that it is necessary to retrain the machine learning classifier if the location of the WiFi endpoints between which the CSI is measured changes. For a given location of the WiFi link, the classifier can be trained by a user with moving to different states as shown in Fig. 4.7. Note that we perform our training separately for "Entrance" and "Inside store" in the layout shown in Fig. 4.8. It is not required to retrain the classifier for different shoppers. Two machine learning algorithms - decision tree and simple logistic regression - are used to train and test the classifier.

#### 4.2.4.3 Performance Evaluation

- **Activities Around the Entrance** For evaluating the performance of detecting shopper's states at the entrance, we first ask 3 users to be in the following states (refer to Figs. 4.7 and 4.8) - walk outside the entrance, walk at the entrance, walk after entering the store, stand near the entrance. Another state "no person" is also considered to identify absence of any shopper. Each shopper repeats these activities 20 times where each round of the activity lasts around 10 seconds.

The classification accuracy results for identifying shopper's state at the entrance are shown in Fig. 4.10. Average accuracy of nearly 90% and 85% can be achieved using the decision tree and

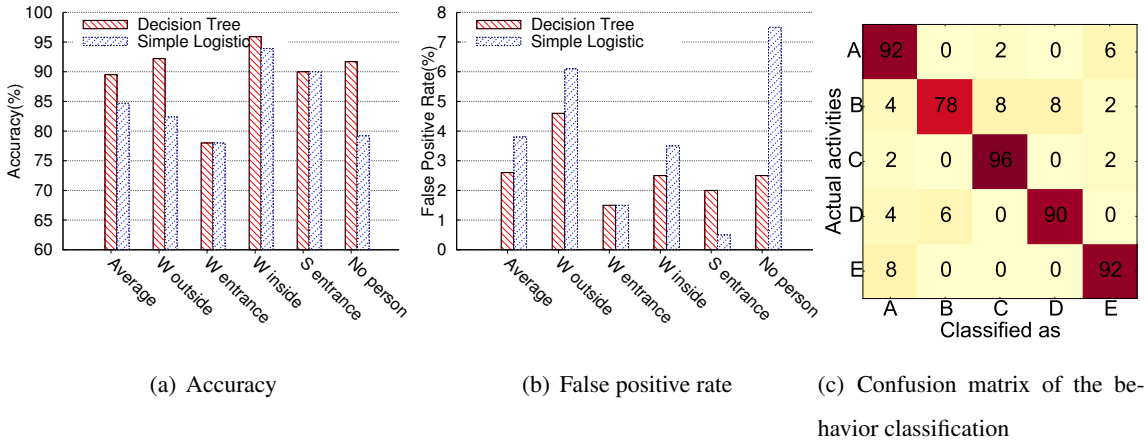


Figure 4.10. Performance around the entrance (W is "walk" and S is "stand") (In the confusion matrix: A is "walk outside", B is "walk at entrance", C is "walk inside", D is "stand at entrance" and E is "no person")

simple logistic regression-based classifier respectively. We observe that decision tree-based classifier always performs better or equal compared to the simple logistic regression-based classifier. Fig. 4.10(b) shows that average false positive rate for classification is approximately 2.5% and 3.8% for decision tree and simple logistic classifiers respectively. This shows that shopper's state can be accurately identified using the CSI with a low false positive rate. It is observed that walking outside the entrance and walking after entering are typically better classified compared to walking near the entrance. Fig. 4.10(c) shows the confusion matrix for each state at the entrance. We can see that walking near the entrance is often mis-classified walking inside and standing at the entrance, due to their similarity in location and activity. Similarly, walking outside the entrance is often misclassified as no shopper being present. This is due to the fact that while walking outside, a shopper may walk far away from the WiFi link, which leads to the misclassification as no user present.

- **Activities Inside the Store** After entering the store, the shopper will have different activities which can be used to infer different shopping behavior. Here we consider different states during a typical shopping (shown in Fig. 4.7) - shopper is walking fast, walking slowly or standing. To conduct the experiments and collect CSI profile, we ask three persons to walk (fast and slowly) and stand inside the store. The walking/standing locations are shown in Fig. 4.8. Same as the entrance case, each person repeats the activities for 20 rounds and each round is recorded for around 10 seconds.

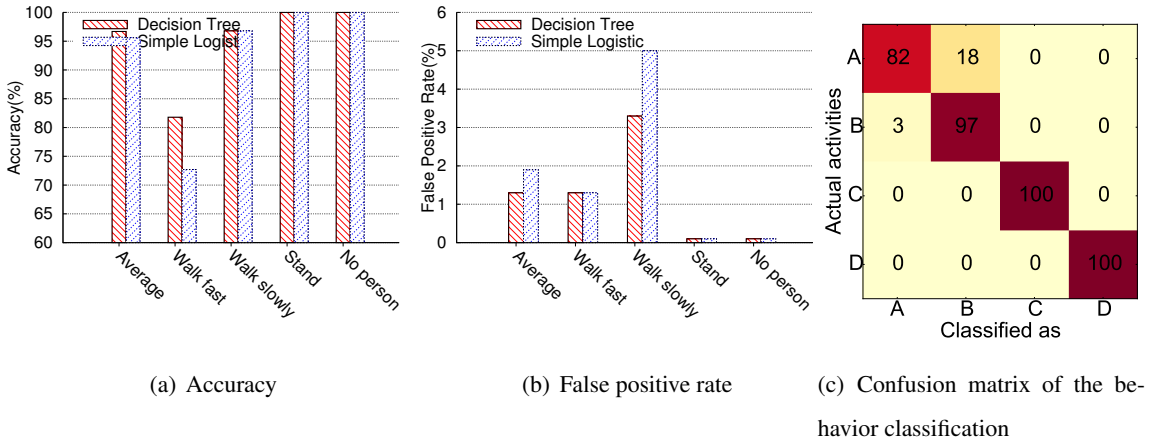


Figure 4.11. Performance inside the store (in the confusion matrix: A is "walk fast", B is "walk slowly", C is "stand" and D is "no person")

Fig. 4.11 shows the results of classification accuracy for shopper's states inside the store. A higher average accuracy of classification (decision tree - 96%, simple logistic - 95%) is observed compared to the entrance scenario. The false positive rate is also observed to be as low as 2% in Fig. 4.11(b). The lowest classification accuracy is observed for the walking fast state. Based on the confusion matrix shown in Fig. 4.11(c), the walking fast is often misclassified as walking slowly. Depending on different users involved in experiments, walking speeds for fast and slow walking can vary substantially, leading to higher mis-classification rate.

#### 4.2.5 Related Work

**Physical Analytics:** The growing interest in tracking user's movements, locations and activities has attracted both industry and research community towards physical analytics. WiFi-based indoor localization has been studied extensively [59–61] in recent years. Other ways of localization such as using visible light and LEDs [62] are proposed to overcome the accuracy limitations of RF-based localization methods. The localization techniques only provide shopper's location but no other information such as shopper's behavior, browsing pattern etc. are available. In a recent work, Rallapalli et al. [57] proposed the use of smart-glasses for analyzing shopper's fine-grained behavior such as gaze, fetch etc. The limitation of such approach is that the information is available to the shopper and not the business owner, requiring active engagement from the shopper to share the information. Instead, in this work, we have focused on detecting shopper's behavior only with passive monitoring using WiFi.

**WiFi-based Sensing:** With the availability of CSI in commercial off-the-shelf hardware using tools such as [55], WiFi-based sensing has attracted considerable attention in recent years. The CSI informa-

tion has been used for gesture recognition [64, 65] and in-home activity recognition [66]. Our work builds on this research to further improve the accuracy of fine-grained activity recognition (such as fast walking vs. slow walking), and identifies important challenges of WiFi-based sensing in physical analytics applications.

#### 4.2.6 Potential and Limitations

**Cost, Scalability and Privacy:** Since WiFi-based behavior analysis can reuse the existing WiFi infrastructure, it is more cost-effective and scalable compared to video-based analysis which incurs substantial deployment and processing cost for a large retail store. WiFi-based sensing also preserves shopper’s anonymity as shopper’s identity can not be revealed through sensing.

**Number of shoppers:** One major limitation of our proposed approach is that it assumes there is only one shopper in the range of any WiFi link. Since, in practice, there can be many shoppers in a retail store, this assumption would require many WiFi links to be deployed in the retail store. To sense the activities of multiple shoppers within one WiFi link, sectors can be generated using beamforming and shoppers in different sectors can be monitored in parallel.

**Fine-grained shopper activities:** Another challenge in WiFi-based sensing is that it becomes increasingly difficult to detect fine-grained activities of the users. For example, detecting if a shopper is reading the item label or puts the item in a cart requires fine-grained CSI fingerprinting. In recent work such as [66, 67], such fine-grained activity recognition is shown to be feasible with CSI, however, further work is required in the context of physical analytics.

**Hybrid Sensing:** Although the CSI-based sensing of shopper’s behavior protects her identity, in some cases, it can be beneficial to identify the shopper uniquely for profiling purposes. To address this, CSI-based sensing can be combined with activity recognition through shopper’s wearable/mobile devices [57, 58]. Such hybrid approach can overcome some of the limitations of CSI-based analytics by improving classification with multiple shoppers and fine-grained activity recognition.

**Type of retail store:** The shopper’s behavior is likely to differ depending on the type of the retail store. For example, the same shopper may walk differently in a furniture store and a grocery store. Hence, it is necessary to train the WiFi-based sensing of user’s behavior for a given retail store to account for business specific characteristics.

#### 4.2.7 Summary

In this work, we present a novel physical analytics approach which leverages CSI from WiFi network to infer shopper’s behavior. Our proposed system is a non-intrusive, device-free, low-cost and privacy-

preserving way to perform physical analytics. It can achieve around 90% accuracy to classify different states of the shopper during a typical in-store visit. We also discuss various limitation and potential of our system.

# **Chapter 5**

## **Enriching WLANs with Device-free WiFi-based Person Identification System in Smart Spaces**

### **5.1 Introduction**

There has been an increasing interest in offloading the functionality of user's smart devices to the infrastructure surrounding the user. Embedding sensing, computation and communication capabilities in the environment such as home or office can allow a person to be truly "device-free" while still receiving the same services otherwise available through portable/wearable devices like smartphone. Such intelligent environments are often referred as smart spaces. Numerous applications can be enabled with the realization of smart spaces. For example, currently counting the number of steps walked by a person requires her to constantly carry a device (smartphone or fitness band) at all times even at home. Similarly, tracking sleep behavior requires her to wear a sleep tracking device even during her sleep. The need of carrying/wearing devices introduces a great deal of discomfort to the user and also inaccuracy in measurements when the user does not wear the device as suggested. With the emergence of smart space, such sensing and activity tracking functionality can be performed by the environment (home or office) itself, relieving people from the need of constantly wearing smart devices.

There are huge challenges in the true realization of smart spaces. Tracking a person's actions in smart spaces requires sensing without any physical interaction. Monitoring a person's activities like sleep and walking through audio/video is possible, however, it imposes unacceptable privacy risks. Recent research on activity tracking using RF signals of WiFi provides an attractive solution for device-free sensing. Authors in [68] demonstrated that a large set of in-home activities can be identified using WiFi. Similarly, device-free person localization using WiFi is also shown to be feasible using [69]. WiFi-based activity recognition is especially attractive due to the pervasiveness of WiFi and low-cost availability of

WiFi devices. The availability of Channel State Information (CSI) for 802.11n WiFi devices has further fueled the device-free activity recognition using WiFi.

Current state of WiFi-based activity recognition has many limitations. One of the biggest limitations of such schemes is that they cannot identify a person using WiFi in a smart space. Person identification can be considered a prerequisite for activity recognition since without that, it is not possible to associate a sensed activity to a given person. For example, if it is possible to identify the person who is in the home, detected activity (e.g., cooking [68]) can be associated with that person. Such person identification can make way for many applications in smart spaces. When a smart home detects that one of the five family members has entered the home, it can use that identity to trigger person-specific customization such as adjust room temperature using thermostat, provide content recommendation on television, start coffee machine etc. It would also facilitate several applications related to Internet-Of-Things (IoT) that might be otherwise infeasible without knowing the person's identity.

In this paper, we investigate person identification problem using WiFi. Specifically, we address the following question - can we identify a person out of the  $n$  known people with simply the use of WiFi? We are primarily interested in scenarios such as smart homes and offices where a person currently present can be identified from the know  $n$  people sharing the home or office. As an example, our technique is applicable to a typical house or apartment complex that is shared by 4-5 family members or an office that is shared by 6-7 people. In both cases, it is reasonable to assume that there is an active WiFi connection. In this paper, we present WiWho, a framework which can monitor and mine the variations in the WiFi signals to identify a person.

Person identification using WiFi is an extremely challenging problem. One possibility is that in a small group of people, a person can be identified uniquely from her height or body mass. Sensing the impact of a person's height or body mass using WiFi signal is very difficult in indoor environments due to severe multipath. Such fine-grained sensing is not feasible using current off-the-shelf WiFi hardware and requires a dedicated software-radio or an antenna assembly (such as [69] or [70]). Our objective in this work is to use the existing WiFi infrastructure to allow pervasive, low-cost deployment of smart spaces. To address these challenges, WiWho relies on off-the-shelf WiFi hardware to measure variations in WiFi signal using detailed CSI. WiWho exploits the rich indoor multipath to understand how various reflected paths are affected when a person walks around. We show that after removing distant multipath and other noise, it is possible to detect a person's walking steps directly from the CSI. This step information in signal domain is rich enough to characterize the person's gait (manner of walking). Previous research

[71, 72] has shown that gait is sufficient to identify the person. By analyzing the shape of a person’s step, walking speed and overall variation in CSI due to walking, WiWho is able to identify a person uniquely from a small group of people.

WiWho is well suited for person identification in smart spaces. It does not require a person to carry any device (such as a smartphone) for identification. This is especially important in indoor scenarios as a person might not carry the smartphone with her all the time. Unlike face/fingerprint recognition methods which require deploying dedicated hardware, WiWho is low-cost as it reuses the existing WiFi infrastructure for identification. Another important advantage of WiWho is that it simply relies on a person’s walking and does not require her to proactively perform any activity to get identified. It also provides improved privacy compared to identification through audio/video monitoring which can also track other private activities of the person. With extensive evaluation, we show that WiWho provides moderate to high accuracy of person identification. We believe that such accuracy is reasonable for smart space applications (homes and offices) where primary purposes of identification are convenience and entertainment. WiWho is not suitable for high-risk applications (such as government identification or authentication at airports) where mis-identification can have life-threatening consequences.

The contributions of this work can be summarized as follows:

- We provide measurement-based evidence that channel state information between two WiFi endpoints can be used to identify walking steps of a (device-free) person. Similar to accelerometer-based step detection, step cycles can be constructed purely from the CSI data. This can enable various smart space applications such as a device-free pedometer.
- We demonstrate that a person’s step information available by monitoring CSI is rich enough to determine the person’s individual walking gait. Based on the previous works which proved that gait can be used to identify the person, we analyze the CSI-based gait of different people to determine the properties that can allow us to distinguish different people. To this end, we present WiWho, a framework that can passively monitor the CSI in smart spaces, and identify a person (out of a small group of known people) based on her walking gait analysis.
- We evaluate WiWho using experiments with off-the-shelf hardware and 20 volunteers at multiple locations. WiWho can identify a person with average accuracy of 92% to 80% from a group size of 2 to 6 people respectively. In most cases, it only requires a person to walk for less than 2-3 meters in order to get identified based on the gait analysis. We discuss the potential and limitations

of such WiFi-based person identification from the perspective of smart space applications.

The remaining of the work is organized as follows. Section 5.2 provides an overview of WiFi-based sensing approaches. We discuss the design goals and system overview in Section 5.3. Section 5.4 provides a motivating study describing how CSI can detect steps and feasibility of person identification. Section 5.5 describes the details of walking detection and Section 5.6 provides the details of person identification using CSI-based gait. The evaluation results are presented in Section 5.7 followed by the discussion in Section 5.8. We conclude in Section 5.9.

## 5.2 Related Work

**Wireless Sensing:** Recently, wireless signal based sensing has innovated many applications. Recent works have shown that we can leverage the wireless signals to detect human motion and activities [68, 69, 73], recognize gestures [70, 74] and other types of sensing (e.g., hearing people talk [67], counting crowd [75], estimate queue length [76], detecting fall [77] and monitoring sleep [78]). However, among these wireless sensing applications, there remains one fundamental question unsolved - person identification. This paper is the first work to achieve person identification purely using wireless signals in a device-free manner. We believe that our work can be applied with the aforementioned works to enable more practical and personalized applications in smart spaces.

**Gait-based Person Identification:** Gait has been recognized as a unique signature for human beings. Recent works have demonstrated that gait can be used as a biometric signature for person identification. In [79, 80], authors use video cameras to record people walking and extract gait information from the video record. These video based methods introduce major privacy concerns and require camera deployment incurring high cost. Other works leverage various sensors, such as floor sensors [81], rotation sensors [82] and accelerometer-based wearable or smartphone sensors [83–85], to capture gait signature. Ngo et al. [72] use the largest inertial sensor-based gait database which contains 744 subjects to further evaluate and compare different sensor based gait identification approaches. Pan et al. [86] deploy geophone on the floor and identify walking people through detected structural vibration. However, all above sensor based methods require people carrying additional devices on the body or deploy these sensors in the environment which are not convenient and require additional cost. Our work solves this problem in a convenient, low-cost and effortless manner leveraging the existing WiFi infrastructure.

Many other methods can be used for person identification. Unar et al. [71] did a comprehensive survey about all possible biometrics which can be used for person identification. Some biometric tech-

nologies, such as fingerprint, retina and face recognition, have higher accuracy and are more reliable. However, such kind of methods cannot be directly used for smart spaces scenarios either due to their high cost or inability to operate in a device-free manner.

## 5.3 Overview of WiWho

In this section, we describe the design goals, usage scenarios, challenges and the overview of WiWho.

### 5.3.1 Usage Scenarios and Design Goals

**Usage Scenarios:** Our objective in this work is to design a low-cost device-free solution for person identification using WiFi. It is necessary to point out that our objective is not to design a person identification system that provides nearly 100% accuracy. Our system should not be used in many situations/scenarios such as identifying a person at an airport or any other government identification where error in identification can lead to life-threatening consequences. Instead, our system is useful for purposes of convenience and entertainment in homes and offices where the penalty of mis-identification is not catastrophic.

**Design Goals:** In the view of the application context, the proposed person identification system in smart spaces should meet the following goals:

1. **Device-free and effortless:** The system should not require the person to carry any device. It is expected that the person in a smart space is not carrying her smartphone or any similar device such as a wrist-band. This is inline with the design goal of a smart space itself where instead of relying on the person, more and more functionality is handled by the infrastructure itself. Requiring the person to carry a device that can provide identification credentials to the smart space reduces the overall usability and introduces inaccuracies when the person does not wear the device as intended. Furthermore, no proactive interaction from the person should be necessary in order to get identified. This means that the person should not have to perform any additional activity (such as posing for face recognition) to make the identification process as effortless as possible.
2. **Low cost and moderate accuracy:** Another important design goal is that person identification solution should be low cost and moderate identification accuracy is acceptable. This means that a solution which can provide very accurate identification but incurs high cost is less desirable than the one where moderate accuracy is feasible at a lower cost. An example of such system is fingerprint-based biometric authentication which is not only a high cost solution but also defeats our previous goal of effortless person identification.

3. **Privacy:** Person identification process should not result in privacy leakage for the person. Since such privacy measure can be subjective, this design goal is difficult to achieve. However, it is still possible to rule out the use of audio/video monitoring for identification (e.g., voice/face recognition) as they can track each and every movement of the person. Similar to the design goal of low-cost, it is necessary that our solution protects the person’s privacy even if that reduces the identification accuracy.

### 5.3.2 Central Idea and Challenges

Our central idea in this work is to exploit WiFi signals for person identification. It can be claimed that WiFi-based person identification can meet all the design goals described above. WiFi is already pervasive in indoor environments such as home and office. This means that using WiFi-based sensing will eliminate the need of deploying a dedicated system.

At first, it is not clear how WiFi-based sensing can be used for identifying people in an indoor environment. One possible solution is to analyze the WiFi signals reflected from a person’s body. Assuming that the person was stationary (e.g., standing without any movements), the received signal might have different signature for different people depending on his/her height, waist and body mass. The problem with this approach is that it is extremely difficult to isolate the signal which reflected from a person’s body because indoor propagation is dominated by severe multipath (presence of many reflected paths). Although recently WiTrack [69] showed how body reflection waves can be used for tracking, it requires a software radio platform and custom antenna assembly. We are interested in developing a solution that can work with low-cost off-the-shelf WiFi hardware without requiring any modifications.

In this paper, we propose a novel way of using WiFi signals for person identification. We show that even though the indoor environments face severe multipath, a person’s walking activity can be recognized using CSI. It is also shown that variation in the wireless channel state provides sufficient information so that it is possible to identify a person’s walking gait. Similar to accelerometer-based gait analysis, we analyze the *CSI-based gait* information for different people and find that it not only can provide detailed step information but also can distinctly identify a person. This provides us with a novel technique to identify a person from a small group of people without requiring the person to carry any device or perform any activity proactively.

**Challenges:** There are many challenges in using CSI-based gait for person identification. First of all, it is not clear whether we can detect if and when a person is walking purely using the CSI data. This is because in a rich multipath environment such as home or office, the received signal is a combination

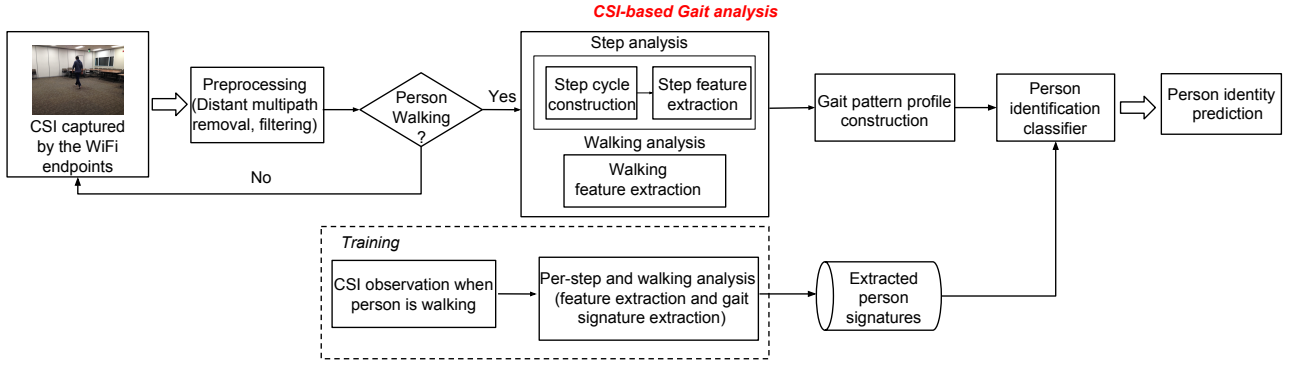


Figure 5.1. System architecture of WiWho

of multiple reflected paths. This requires the design of a technique that can distinguish CSI variations due to walking from that of other activities. Second, even if we can determine that a person is walking, to identify the person, it is necessary to observe fine-grained gait information from the CSI. This requires that the effect of a person's walk is distilled from the noisy signal which may be affected by other reflections (e.g., people moving in the next room). Third, different from accelerometer-based gait measurement which is location-independent, CSI-based gait is highly dependent on the multipath of a given room. We will address these challenges in Sections 5.4, 5.5 and 5.6.

### 5.3.3 System Overview

The outline of our WiWho is provided in Fig. 5.1. We assume that there are two stationary endpoints in the room of the home or the office where WiWho is deployed. These endpoints communicate with each other to collect the current CSI. One endpoint can be a WiFi AP and the other can be any WiFi equipped device such as a desktop computer or a smartTV. Two endpoints are only needed to collect the CSI data, and the WiWho is only required to be operating on one of the endpoints (say the AP). It is assumed that a person (not equipped with any device) starts walking in the room. At the same time, the collected CSI samples are constantly analyzed to determine if the person is walking or not. This includes removal of distant multipath and noise filtering. If it is detected that a person is walking, the CSI samples are input to the gait analysis module. The gait analysis consists of two parts:

- (1) Step analysis: In the step analysis, the step cycle is constructed from the CSI data and for each of the detected step, and various features of its shape are derived.
- (2) Walk analysis: It analyzes the overall walking behavior of the person for the entire walk segment (multiple steps). This provides information on various body movements that can be different from person to person.

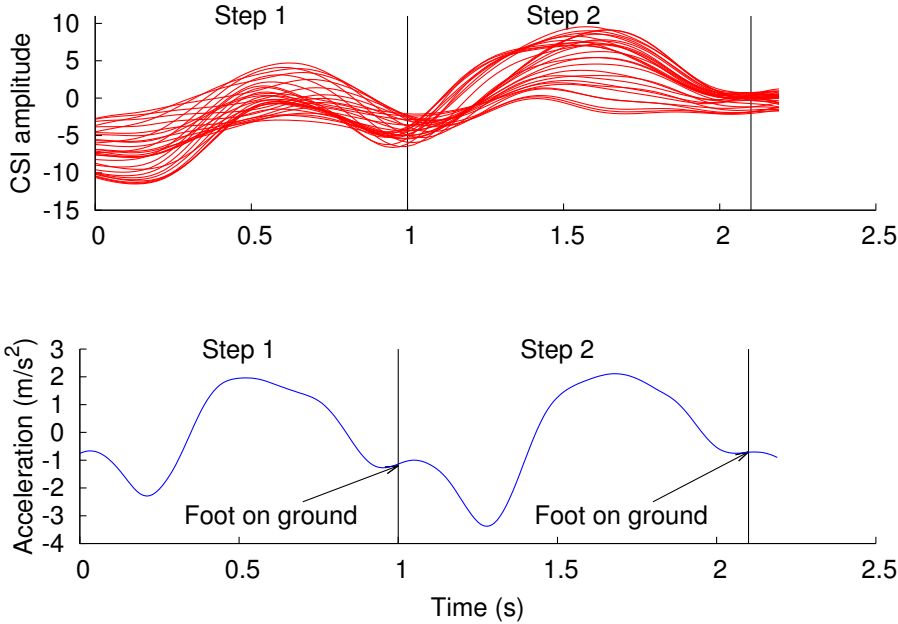


Figure 5.2. Comparison between CSI Amplitude and on-body accelerometer readings while a person is walking

The characteristics of step and walk are extracted in the form of features. They are then compared to pre-trained people walk signatures using a machine learning classifier. The classifier outputs its prediction of the person’s identity. An important part of WiWho is training where per-person gait signatures are built. In the training phase, each person who would like to be identified walks on a pre-determined path for fixed number of times. The CSI samples are collected for during the training phase. The CSI samples are analyzed for gait and walk characteristics, and a CSI-based gait signature is extracted for each person.

## 5.4 Measurement based Feasibility Study

In this section, we will provide some preliminary results that serve as a motivating study for WiFi-based person identification.

### 5.4.1 Detecting Gait from CSI

The first challenge of designing WiWho is to detect if there is a noticeable pattern in the observed CSI while a person is walking. Note that just detecting whether a person is walking or not is not enough to distinguish between different people. WiWho requires detecting the step cycle and constructing gait profile from a person’s walking activity using purely observed CSI data.

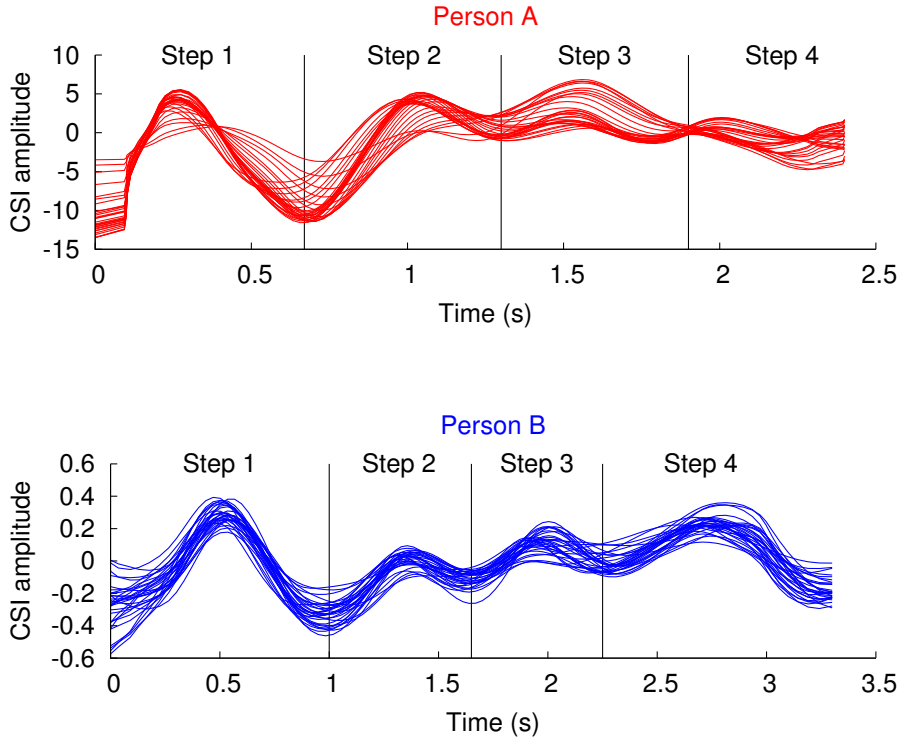


Figure 5.3. Comparison between the CSI-based gait of 2 people

To demonstrate that gait can be detected using CSI, we carry out an experiment where a person walks on a straight line in a room with two WiFi endpoints communicating and collecting CSI. For generating the ground-truth of gait, the person also carries a smartphone in the pocket. Fig. 5.2 shows synchronized CSI and accelerometer data for the person's walking. For CSI, we plot the amplitude of 30 subcarriers for one spatial stream, and for accelerometer, we plot the acceleration values for X axis. Note that the CSI data shown in this section is preprocessed from the raw data for removing various types of noise. We will discuss this procedure in details in Section 5.5.1.

It is observed from Fig. 5.2 that the step cycles can be extracted from the CSI data. The steps observed through CSI follow a similar pattern of alternating peak and valley. Unlike accelerometer observations, the steps detected by CSI is less fine-grained i.e. various phases of gait are not clearly detected like [87]. However, we will show that this CSI-based gait information is rich enough for person identification. Since CSI-based gait is observed by nearby WiFi devices and not by a device worn on the person's body, it is dependent on location-specific multipath. This means that the gait varies at different locations as a person walks in a room. We will address these issues in Section 5.6.

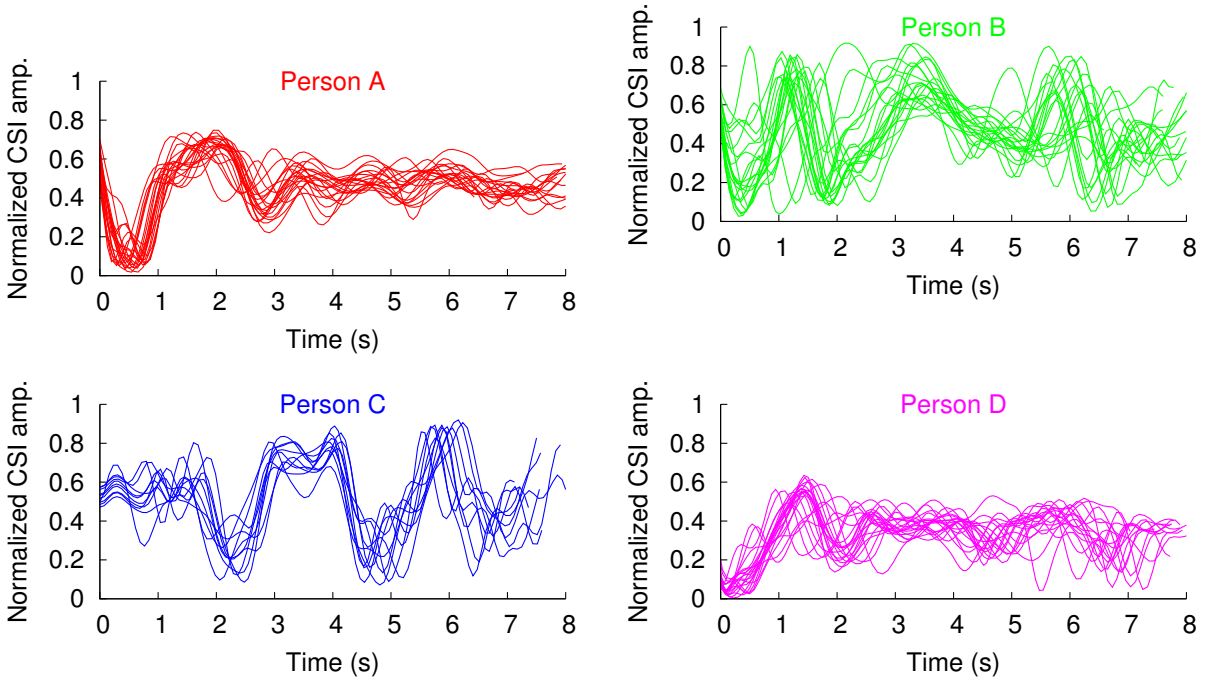


Figure 5.4. Comparing CSI-based gait for different people over time

#### 5.4.2 Difference in CSI-based Gait for Two People

Although we are able to get the gait information from CSI, it is not clear whether such information is sufficient to uniquely identify different people. To investigate this, we perform an experiment where two people walk in a room on the same path and we capture the CSI data. Fig. 5.3 shows the CSI data for the initial four steps while two people are walking separately. By visual inspection, we can see the difference between the *shape of the steps* between the two people. Also, the step lengths also observed to be different for these two people. These visually observed difference and many other underlying differences will be used for building unique gait profile for each person which will be used for identifying individual person.

#### 5.4.3 Consistency of CSI-based Gait over Time

One of the most important question to investigate for person identification through CSI-based gait is - does the CSI-based gait for a given person remains the same over time for the same location (e.g., room)? This means that if we learn a person's CSI-based gait at one time, can we use the same gait to identify the same person at a different time? To address this, we ask 4 different people to walk one after the other for 20 rounds. To understand the consistency over time, the rounds are separated by 10 minutes. We plot the mean CSI amplitude across all subcarriers of each round for 4 different people in Fig. 5.4. It

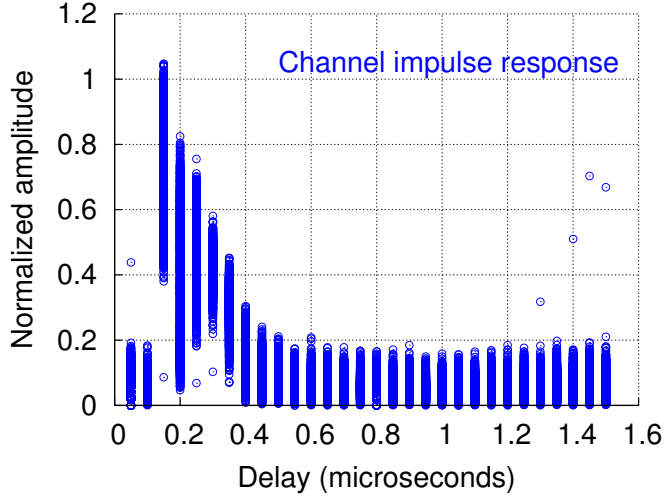


Figure 5.5. Channel impulse response showing distant multipath

is observed that for any given person, the CSI-based gait remains similar between each round even over nearly 2 hours of time period.

Our preliminary study shows that CSI-based gait for one person is more or less consistent over time, and it is sufficiently different for different people. This motivates us to design a person identification system based on CSI-based gait.

## 5.5 CSI Preprocessing and Walking Detection

### 5.5.1 CSI Preprocessing

Current WiFi standards like 802.11n and 802.11ac use Orthogonal Frequency Division Modulation (OFDM) for their physical layer. In OFDM, the channel is divided into multiple subcarriers and the data is transmitted over the subcarriers using the same modulation and coding. The CSI information represents the amplitude and phase information of the OFDM subcarriers. It is a complex-number matrix that shows the Channel Frequency Response (CFR) of each individual subcarrier for all spatial streams. The raw CSI data can be considered noisy for direct use in person identification. Specifically, there are two types of noise we are interested in removing - (1) distant multipath and (2) high-frequency noise due to other movements.

(1) Distant multipath removal: Distant multipath is a result of reception of a strong signal due to reflection from a distant object or person. For example, in case of WiWho, such reflection can be due to person moving far away from the room where CSI is collected. The distant multipath can cause the observed CSI profile to vary in a non-deterministic manner which can affect the gait analysis. To address

this, we remove the distant multipath from the CSI data. Note that the CSI contains CFR for 30 subcarriers which includes the distant multipath. We first convert the CFR to Channel Impulse Response (CIR) which provides the delay profile of signal reception. An example CIR is shown in Fig. 5.5 which contains distant multipath components after the delay of 1 microsecond. We remove the multipath components that have delay more than 0.5 microseconds, and convert the CIR back to CFR using FFT (Fast Fourier Transform). Note that this threshold is chosen based on the multipath delay characterization provided in previous studies such as [88]. The multipath removal allows us to focus on the reflected paths within a room which is necessary for fine-grained analysis of gait.

(2) High-frequency noise removal: Another important noise removal procedure in our case is to eliminate the high-frequency noise from time-domain CSI signal. The walking activity of a person typically exhibits energy in 0.3 Hz to 2 Hz [63] frequency band. This is attributed to arm and leg movements while walking which is known to happen at no more than 2 Hz frequency. In order to distill the step cycles from the time-series CSI data, we apply a butterworth band-pass filter with cutoff frequency of 0.3 Hz to 2 Hz. Such filter also removes the static DC component.

Note that the high-frequency filtering is only necessary for step analysis which finds the step cycles and performs step shape analysis. WiWho also performs walk analysis that extends to an entire walk segment (multiple steps). In the walk analysis, we are interested in studying the movement of body parts which may happen at a faster rate than 2 Hz. Hence, we will separately study different frequency bands (upto 10 Hz) for walk analysis in Section 5.6.3.

### 5.5.2 Walking Detection

As shown in Fig. 5.1, the first step towards identifying a person using CSI-based gait is to detect whether a person is walking or not. In this section, we discuss how we can detect walking activity using the CSI data and how we can distinguish it from other indoor activities such as standing, sitting, typing etc. Accurately detecting the walking activity will ensure that the gait-based person identification is only initiated when a person is found to be walking.

Our approach towards distinguishing various activities from the CSI data stems from accelerometer and gyroscope based activity recognition. Based on the previous research [63, 89] on this topic, different human activities can be identified using the frequency domain analysis of a person's movements. Typical indoor activities such as sleeping, standing, sitting, walking etc. show different characteristics in the frequency domain. These activities can be categorized as low or moderate intensity activities as shown in [63].

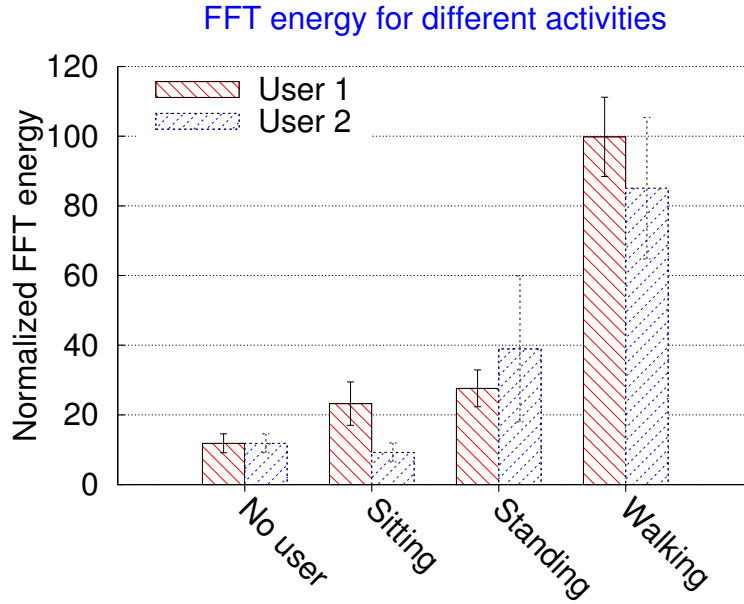


Figure 5.6. Comparison of FFT energy in a 6s window between different activities

Note that the smart space scenario allows us to exclude the high intensity outdoor activities (driving, playing sports etc.) which in turn simplifies how we can detect if a person is walking or not.

To verify that frequency domain properties of different activities are also observed in the CSI, we perform experiments where (1) there is no person in the room, (2) a person is sitting and performing routine activities such as typing, moving objects on a desk, (3) a person is standing (without taking steps) using her phone, writing on whiteboard and (4) a person is walking. Fig. 5.7 shows the coefficients of the FFT profile for the four activities (without the DC component) observed by CSI data. As we can see, in the case where there is no person in the room, very low amplitude of FFT coefficient is observed in the low frequency band. Compared to that, sitting and standing exhibit higher amplitude values (more intensity) for the same frequencies. However, for the walking activity, the observed intensity in 0.3-2 Hz band is noticeably high. This is expected given that movement of legs and arms are known to move at that frequency while walking.

To represent the FFT profile of different activities, we use a metric referred as motion energy [63]. The motion energy (or simply energy) can be calculated as

$$\text{Energy} = \sum_{i=1}^{\text{window\_length}/2} \text{magnitude}^2 \quad (5.1)$$

where magnitude values are the normalized Fast Fourier Transform (FFT) coefficients calculated over

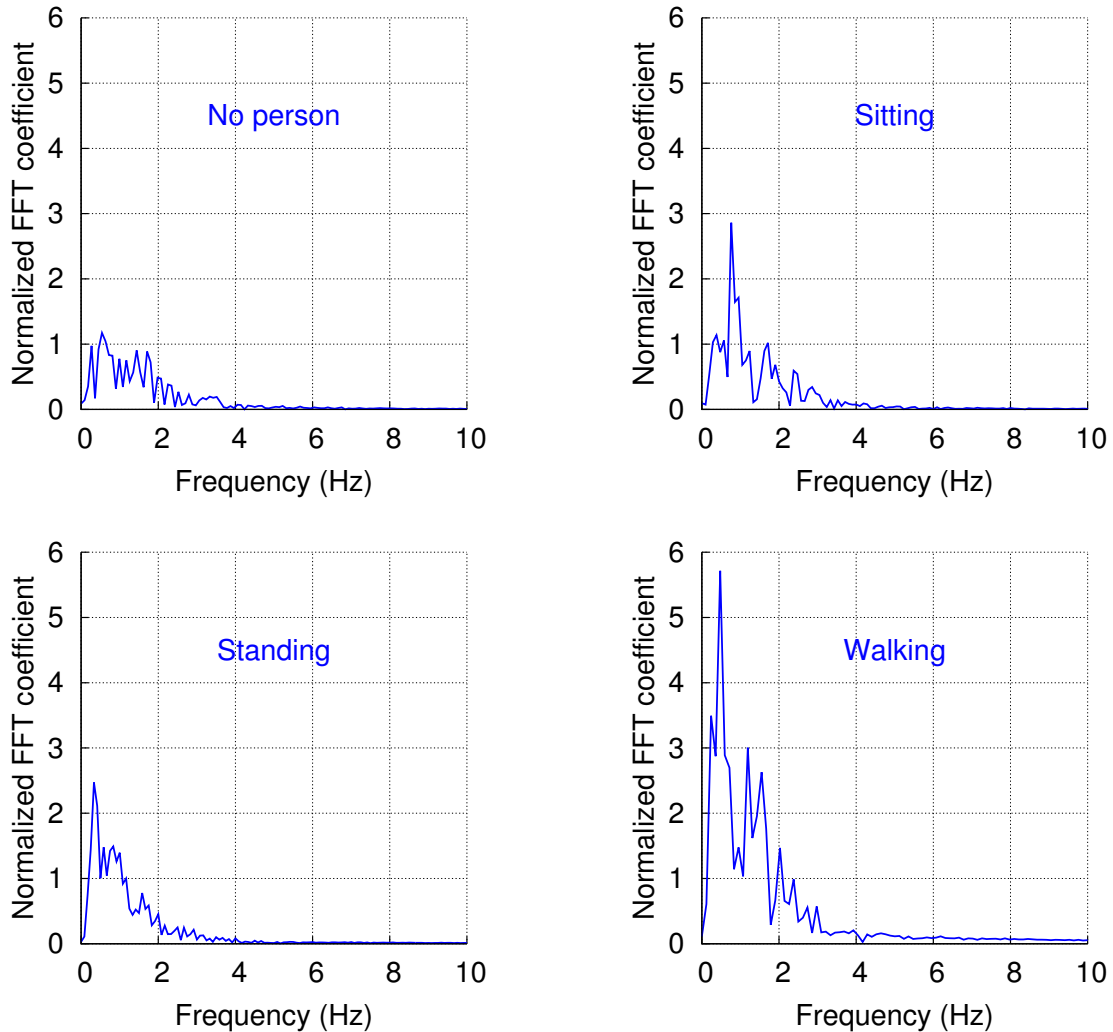


Figure 5.7. Comparison of FFT coefficients for different activities

the time window. Fig. 5.6 shows the observed energy for the four activities for 2 people. Since energy observed during walking activity is much high compared to sitting and standing, we use calculated energy as a way to detect if the person is walking or not.

## 5.6 Person Identification using CSI-based Gait

As shown in Fig. 5.1, the CSI-based gait analysis of WiWho consists of two parts: (1) step analysis and (2) walk analysis. In this section, we first describe the features used for both the parts, and then explain how they are used for step and walk analysis to construct a gait pattern profile. The result of overall gait analysis is used for person identification.

### 5.6.1 Constructing CSI Features

Designing the feature space that can capture a person’s walking gait is challenging because CSI includes amplitude and phase values for each of the subcarriers and spatial streams, and dimensionality reduction is necessary for a tractable analysis. In this work, we primarily focus on one spatial stream mostly due to significant similarity between the data from multiple spatial streams and to lower the computational cost.

Let  $v_t = \{c_1, c_2, \dots, c_s\}$  be the CFR vector for  $s$  subcarriers at time  $t$ . We first append additional statistics to  $v_t$  to generate  $v_t^*$  which includes  $v_t$ , and the maximum, minimum, mean, median, standard deviation, skewness and kurtosis of  $v_t$ . These statistics capture the shape (e.g., peakedness, symmetry, variation) of instantaneous distribution of CFR of all subcarriers. This process is repeated for each new sample of CSI data for the remaining of the feature calculation.

The features are calculated for a time window where the window can be for a step or for the entire walk segment. Table 5.1 describes the time domain and frequency domain features that are calculated for the window. These features are shown to be useful in accelerometer-based activity classification in [63]. For a window of size  $T$ , features of the table are calculated for each subcarrier and its statistics included in  $v_t^*$  for all  $t \in T$ . These features enable detailed time and frequency analysis of CSI data for a time window. We include the frequency domain features such as entropy and energy as they profile the walking activity inside the time window with high accuracy. Note that the choice of time window depends on whether we are analyzing individual steps or a walk segment.

### 5.6.2 Analyzing Person’s Steps

The step analysis evaluates how steps differ from person to person as observed by CSI. Previous research [72] has shown that the *shape* of the step varies noticeably for different people. This has led to design of person authentication methods [83] where smartphone’s accelerometer signal is analyzed to differentiate between people. The challenge with the use of CSI is that the shape of a typical step of a person is highly dependent on the static multipath of the environment. The shape of a person’s step changes at different locations in a room depending on the multipath at that location. When the person walks from one point to another point in a room, the shape of steps also change depending on relative position of WiFi endpoints and changing in multipath.

**Step Cycle Construction:** The step analysis requires finding the step cycle of the first step. However, finding the step cycle is not trivial. Let us consider that we have a time-series CSI data starting from time  $T_s$  to  $T_e$ . The number of steps taken during the time period is unknown and we would like to find out

Table 5.1. Time window features

- **Time domain:**

- Minimum, maximum, median, variance, standard deviation, range
- CV (ratio of standard deviation and mean times 100), skewness (3rd moment), kurtosis (4th moment)
- First, second and third quartiles; difference between the third and the first quartile
- Mean Crossing Rate: number of times the signal crosses the mean value)
- Area under the signal curve and autocorrelation

- **Frequency domain:**

- Energy: measure of total energy in all frequencies (Equ. 5.1)
- Entropy: measures the impurity in the CSI signal
- DomFreqRatio: calculated as the ratio of highest magnitude FFT coefficient to sum of magnitude of all FFT coefficients
- FFTPeaks: 5 largest frequencies in the signal and their magnitude

the step cycle of each step in the time period. One possible solution is to create step template of different people from the training data and compare it with CSI data in  $(T_e - T_s)$  window using Dynamic Time Warping(DTW) to find out the step cycles. However, this requires a brute-force, since every person's step template has to be compared with current window. Such brute-force incurs a prohibitively large computation cost given that DTW requires solving an optimization problem with dynamic programming. Furthermore, due to the step shape for each person will vary at different locations along the walking path, such template matching method will have a very low accuracy for constructing step cycles.

Instead of using DTW, we rely on a peak-valley detection algorithm for step cycle construction. The peak-valley detection algorithm uses local minimum and maximum of time-series data along with the significance constraint [90]. Using this method, we denote the time from the start to the first valley to be the duration of the first step (Fig. 5.2). Immediately after we have detected that a person is walking, we start detecting the step cycle. We also set up an expected step cycle time range of 0.8s to 1.8s [91]. If we detect a step cycle which is less than 0.8s, we will further include the next peak or valley. If the detected step cycle is greater than 1.8s, we will start a new detection. The duration of the first step is then used to detect the rest of the step cycles. This assumes that the step duration does not vary significantly during

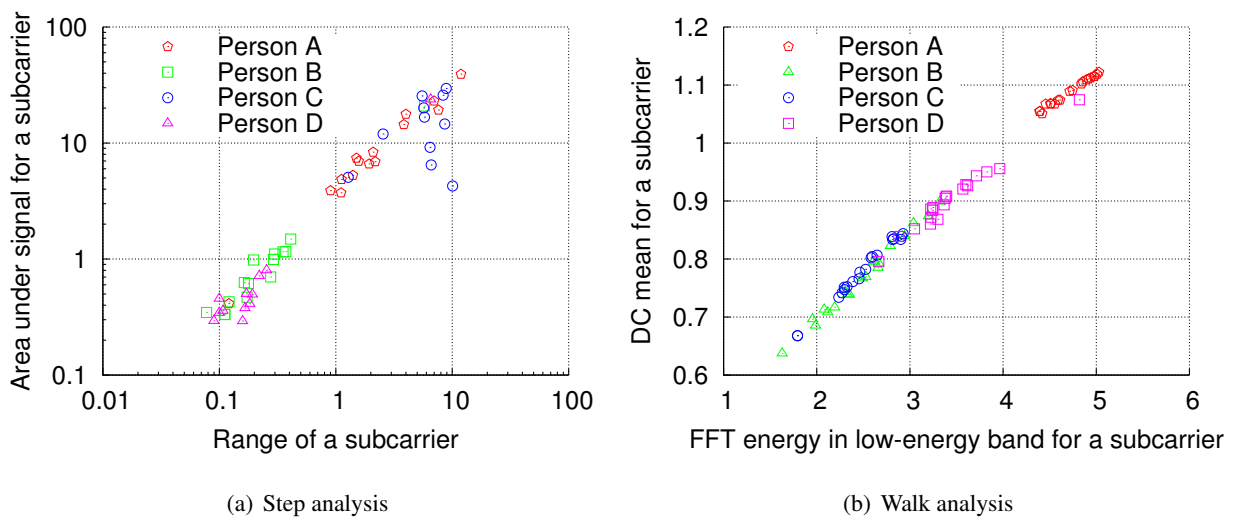


Figure 5.8. Selected features for step and walk analysis

the walk segment. This is reasonable since we assume that person walks on straight line path without any turns or breaks. Note that peak-valley detection algorithm does not detect trivial peaks/valleys since the input CSI data is already filtered to remove high-frequency noise.

**Per-Step Feature Calculation:** After the step cycle of each step is determined from the input walking segment, the CSI data in the time window of each step is used to calculate the features. We first apply the 0.3-2 Hz band pass filter to remove high-frequency noise, and then calculate the time domain features of Table 5.1. We do not calculate frequency domain features as they provide only a little information within a small time window. The time domain features represent the shape of the person’s steps in the form of statistics. Given that the shapes of different people’s steps are likely to be different even at the same location, this will allow us to perform step based person identification. Fig. 5.8(a) shows how two of the features - area under the curve and range - are different for the steps of different people. The results are shown for one representative subcarrier only which is not enough for classification, but all the features calculated for all subcarriers provide sufficient information for identifying the person.

### 5.6.3 Analyzing Person's Walk

The step analysis helps in identifying the typical pattern of each step of a person. However, it can not capture the overall walking behavior that changes at a time scale faster or slower than the step duration. For such analysis, it is necessary to perform frequency domain analysis in order to understand various other characteristics such as the amount of energy in the walk segment across different steps, high frequency movements such as movement of arms, minor posture changes and etc. Such characteristics

found using walk analysis can also help us to distinguish different people along with the step analysis. To perform the walk analysis, we calculate the features presented in Table 5.1 for the entire walk segment. For calculation of frequency domain features, we first identify three activity bands (subset of bands proposed in [63]) as

- (1) Low-energy band: 0 - 0.7 Hz
- (2) Activity band: 0.3 - 2 Hz
- (3) High-energy band: 0.7 - 10 Hz

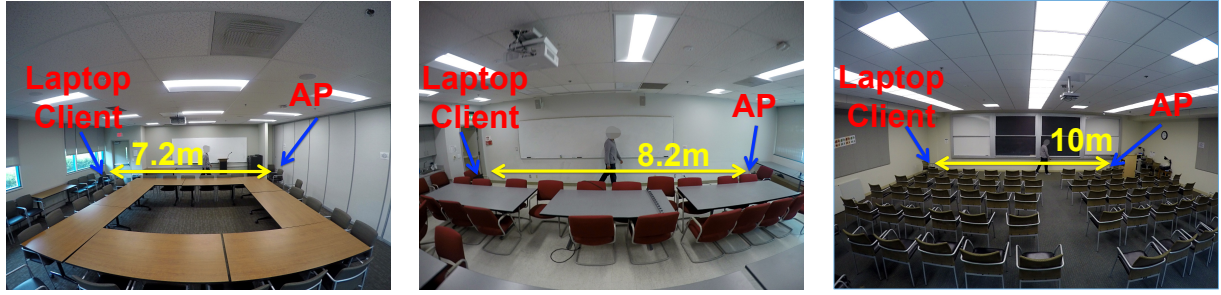
The low-energy band has been found to be useful to profile slow-moving activities such as posture change. It also includes the static DC component. The activity band is of primary interest as it identifies the impact of arm and leg movement while walking, and the energy (intensity) by which a person performs these activities. The high-energy band mostly captures the fluctuations in the CSI that is caused by movements of the person that are much faster in time. The frequency domain features of Table 5.1 are calculated for all three bands described above, while the time domain features are only calculated for the activity band. These features characterize each person's walking behavior which will be used along with the step analysis to construct a complete gait pattern profile for person identification. Fig. 5.8(b) shows the effectiveness of the frequency domain features applied to three frequency bands. It plots energy in the low-energy band along with the mean of DC component to show that such features can distinguish different people based on the pattern of their walking segment.

Apart from these features of step and walk analysis, we also include one additional statistic for each person which is number of steps per second captured by CSI. This represents the walking speed of each person.

#### 5.6.4 Person Identification using CSI-based Gait

After calculating step based features and walk segment features, we combine them to build a complete gait pattern profile for individual person. Note that in order to reduce the computation when the walking segment is long, WiWho only considers first few steps for step analysis.

WiWho uses decision tree-based machine learning classifier to identify people based on the step and walk analysis. The procedure to train the classifier requires the same set of features as for the testing phase. In the training phase, a person walks on a pre-determined straight line path for a certain number of times. The CSI data is collected for these instances and features are calculated. The process is repeated for all the people who would like to be identified in the smart space (e.g., home, office). As mentioned before, the person identification classifier is specific to a given room in a home or an office. This is



(a) Location 1

(b) Location 2

(c) Location 3

Figure 5.9. Experiment layouts and device setup

because the changing the room and location of WiFi endpoints changes the observed multipath, which in turn affects how a person’s step is observed through CSI. However, since the location of WiFi endpoints do not change in a smart space once they are deployed, the classifier is only required to be trained once for that location for all people. Since different locations might have different constraints on indoor space and possible length of walking segments, we will evaluate the performance of WiWho in the cases where person can walk for only a few steps in Section 5.7.

We note that machine learning algorithms other than decision tree can be used in order to improve the identification performance. However, our objective in this work is to demonstrate the feasibility of person identification using CSI-based gait, and we leave the further optimization of performance to future explorations.

## 5.7 Performance Evaluation

### 5.7.1 Implementation and Experiments

**Devices and Setup:** We implement WiWho using off-the-shelf commercial WiFi devices. Our setup consists of an AP-client pair. The AP is Asus RT-AC66U 802.11n WiFi router which has 3 external omnidirectional antennas. The client is a Dell laptop equipped with Intel 5300 802.11n WiFi NIC with 3 external omnidirectional antennas. The laptop runs Ubuntu 10.04 LTS with modified Intel driver and firmware [55] to collect the CSI data. In our setup, the pair of WiFi devices constantly communicates with 100 packets per second to retrieve CSI at that sampling rate. For each packet, the laptop records a CSI sample with CFR of 30 subcarriers. We implement both online and offline versions of WiWho which include preprocessing, gait analysis and person identification modules with over 3000 lines of Python code.

**Experimental Scenarios:** Since our primary focus in this work is smart spaces such as homes and

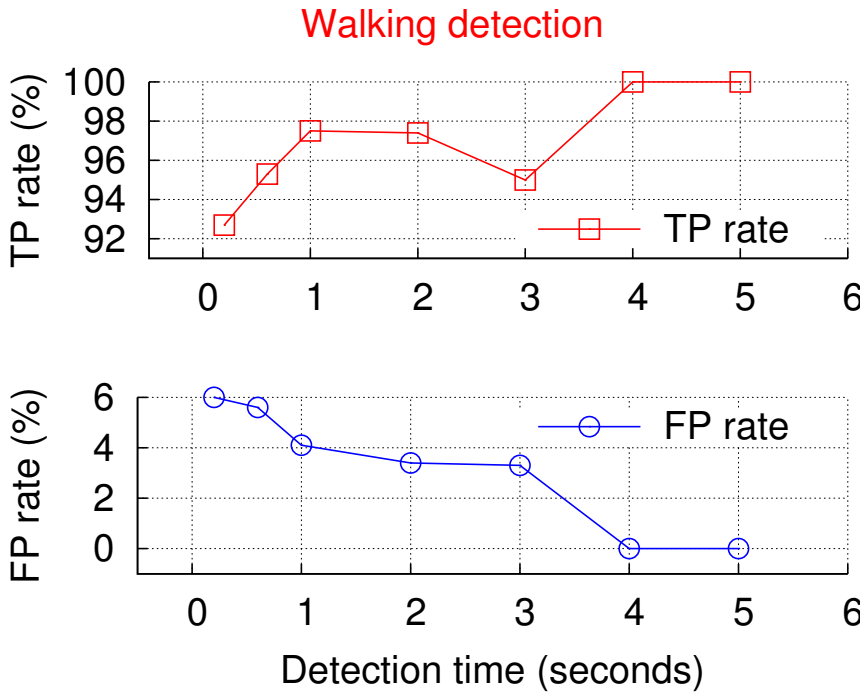


Figure 5.10. TP rate and FP rate of walking detection

offices, we choose three different indoor locations for our evaluation. All the three location layouts are depicted in Fig. 5.9. The three chosen rooms have different sizes and furniture layouts. A total of 20 volunteers were chosen to collect their CSI while walking in the three locations. The walking path is in parallel to AP-client LOS link at a distance of 1m. We consider different group sizes starting from 2 to 7 people at each location. These group sizes were chosen based on the typical number of people sharing a home (3-4) or a small office (5-7). For each group size, we conduct the experiments for 10 different combinations of people. In each combination, every person of the group walks along the pre-determined path (as shown in Fig. 5.9) in a round-robin manner for 20 times. Note that we do not ask people to remain at constant speed while walking. These experiments result in over 180 combinations of people with different group sizes at different locations.

A person's walking pattern is known to depend on her height, weight and age [72]. In our experiments, we selected 20 volunteers with both male and female, age from 22 to 32, height from 5'4 to 6' and weight from 120 lbs to 190 lbs.

**Evaluation Metrics:** We will use the following metrics in evaluation of WiWho.

(1) True Positive Rate (TP rate): TP rate of identification of person A is the fraction of walking instances of person A that are correctly identified as person A. The overall *accuracy* of person identification

		Classified as			
		W	S	T	N
True activity	W	95	0	5	0
	S	1	79	2	18
	T	15	0	85	0
	N	1	16	5	79

Figure 5.11. The confusion matrix of walk detection with 0.6 second detection time. W is walking, S is sitting, T is standing and N is without person

is the weighted average of TP rate of all the people in consideration.

(2) False Positive Rate (FP rate): FP rate of identification for person A is the fraction of walking instances that are incorrectly identified as person A.

Apart from TP and FP rates, we will use confusion matrix to detail how many times each person gets incorrectly identified as (which) other person. In a confusion matrix, the rows indicate the true identity of the person and columns indicate the identity as predicted by WiWho, and each element of the matrix is the fraction of the times the person in the row was classified as the person in the column.

### 5.7.2 Walking Detection Validation

It is crucial for WiWho to detect the start of walking activity from relatively stationary environment. Before performing the gait analysis, WiWho has to recognize that either a person entered the smart space or a person who was sitting or standing with relatively low movements started walking. When the walking is correctly recognized using the techniques presented in Section 5.5.2, the person identification module can be triggered to identify the person walking. An important expectation from WiWho is that it detects that person is walking in a very short time. This evaluation of detection time and average walking detection accuracy is shown in Fig. 5.10. We observe that even at 0.2 second detection time, WiWho can detect the walking activity with 92% TP rate and 6% of FP rate. It can detect the walking with 97% TP rate just after 1 second of start of the walking activity. After 4 seconds, the accuracy of detection is 100%.

Fig. 5.11 shows the confusion matrix for walking activity detection at 0.6 seconds. We observe that walking is often mis-classified as standing with 15% of standing is mis-classified as walking and 5% of walking is mis-classified as standing. This is expected since standing and walking both require the

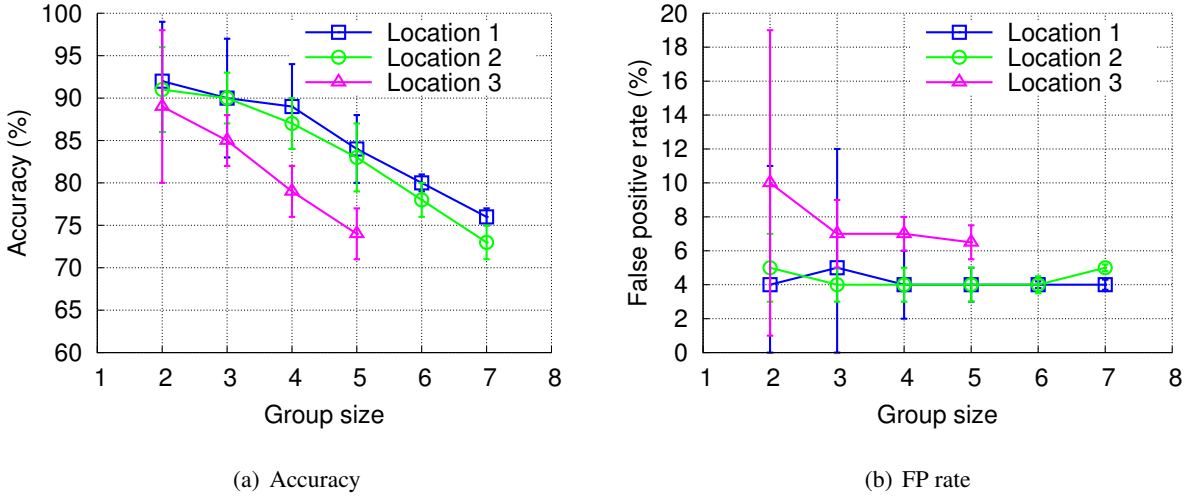


Figure 5.12. The accuracy and FP rate for person in identification with different group sizes

person to be in the same posture and standing is necessary before starting the walk. Since a typical step takes nearly a second for completion, 0.6 second of detection time allows us to capture the gait starting from the first step itself. We choose 0.6 second detection time in the rest of the implementation as it already achieves 95% detection accuracy.

### 5.7.3 Person Identification with Different Group sizes

In this section, we will evaluate the performance of person identification with different group sizes. As we discussed, the application of WiWho is targeted towards smart homes and offices, we only consider group of people in the range of 2 to 7. For each of the group size, WiWho uses gait analysis (step and walk analysis) to detect the person’s identity. Fig. 5.12 shows the average accuracy and FP rate of person identification with different group sizes for the 3 locations. We observe that as the group size increases, the accuracy of person identification decreases for all 3 locations. This is expected since introducing more people in person identification increases the chances of people having similar gait. For the same reasons, the average and maximum accuracy of person identification is as high as 92% and 97% respectively with the group size of 2 (binary classification). The average accuracy decreases to 75% when the group size of 7 is considered. WiWho achieves nearly 80% of person identification accuracy for group size of 6 or lower for all 3 locations.

It is observed from Fig. 5.12(b) that the FP rate of person identification varies only a little with the variation in group size. For Locations 1 and 2, the average FP rate remains lower than 6% irrespective of the group size, and for Location 3, the average FP rate is observed to be close to 8%. It can be claimed that for smart space applications in homes and offices where typical group size is close to 5 people,

		Classified as					
		A	B	C	D	E	F
Actual user	A	89	0	0	0	11	0
	B	0	85	5	5	0	5
	C	0	11	83	6	0	0
	D	0	5	5	79	0	11
	E	0	5	0	0	95	0
	F	0	13	25	0	6	56

Figure 5.13. The confusion matrix of person identification with 6 people

Table 5.2. Characteristics of 6 volunteers

Person	A	B	C	D	E	F
Height	5'10	5'7	5'6	5'7	5'8	5'6
Weight(lbs)	175	130	170	145	125	165
Gender	M	M	M	M	F	M
Age	30	30	28	27	30	29

WiWho achieves high accuracy of person identification while meeting the design goals.

Now we take a further look at the confusion matrix for the case of group size of 6 people. The confusion matrix is presented in Fig. 5.13. It is known from the previous research [72] that a person's gait is loosely correlated to his/her height, weight and age. Table 2 provides these characteristics for the 6 volunteers to understand the misclassifications in the confusion matrix. It can be observed that person F and person C have similar height and weight which can be related to frequent misclassification of person F to be person C. From the confusion matrix, it can be said that person E is found to be most uniquely identifiable among the group. From Table 2, we notice that E is the only female in this group. In general, we claim that identification using CSI-based gait have similar properties as the accelerometer-based gait in terms of overall accuracy.

#### 5.7.4 Step Analysis vs. Walk Analysis

As discussed before, the gait analysis in WiWho is a combined module of step analysis and walk analysis. In this section, we show how well the step and walk analysis modules can perform person identification individually. The walk analysis does not require the walk to be divided into steps, however, it requires FFT computations for frequency domain analysis (Section 5.6) of the walk segment. The step analysis

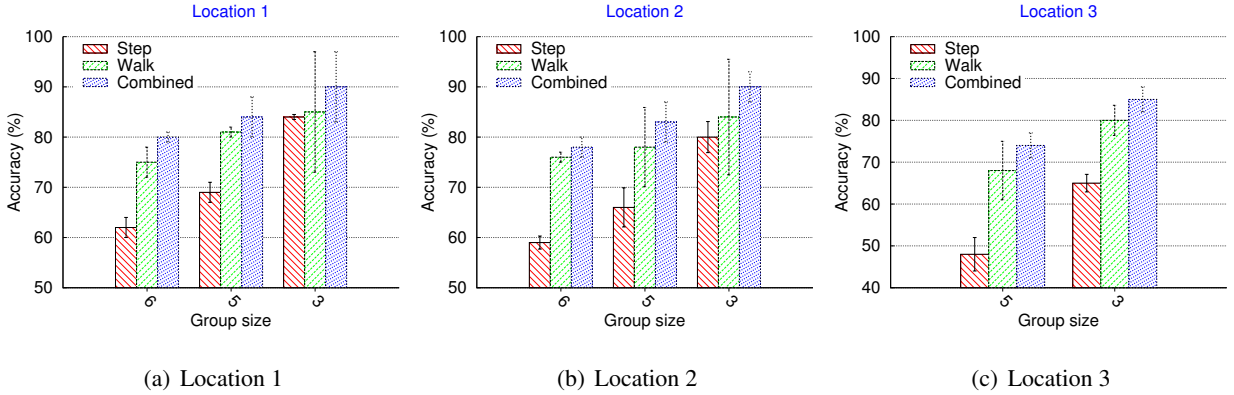


Figure 5.14. The performance with different feature calculation methods and different group size at different locations

requires step cycle construction and calculation of time domain features for each of the detected steps. Fig. 5.14 compares the identification accuracy for only step or only walk analysis, as well as the combined performance. It is observed that walk analysis individually works better to identify different people compared to step analysis. The step analysis applied individually achieves lower accuracy of person identification. This can be attributed to the fact that CSI provides more information on how person walks and body movements during the walk (frequency analysis of walk segment). In all cases, we observe that the combined analysis always improves the accuracy ( $\approx 5 - 10\%$ ) over simply using walk analysis which means that both step and walk analysis modules are essential to achieve high person identification accuracy.

### 5.7.5 Robustness with Different Walking Lengths

Another important factor in evaluation of WiWho is that the length of walking segment that a person walks. In practical scenarios, the layout of rooms and indoor spaces impose the restriction that a user can walk only few steps without taking a turn. We evaluate this situation using experiments at Locations 1 and 2. Specifically, we repeat the experiments of Section 5.7.3 with a restriction on the distance a person can walk before getting identified. The experiments are repeated at for group size of 3, 5 and 6 (10 rounds each). The length of walking segment is set to multiples of 2.4 meters ( $\approx 4$  steps) and 2.7 meters ( $\approx 5$  steps) for Location 1 and 2 respectively. The results of person identification accuracy are shown in Fig. 5.15. The accuracy either increases or remains similar with increase in the length of walk segment. This means that WiWho can identify person with high accuracy even with CSI data for a few steps, increasing its applicability in space-constrained indoor environments.

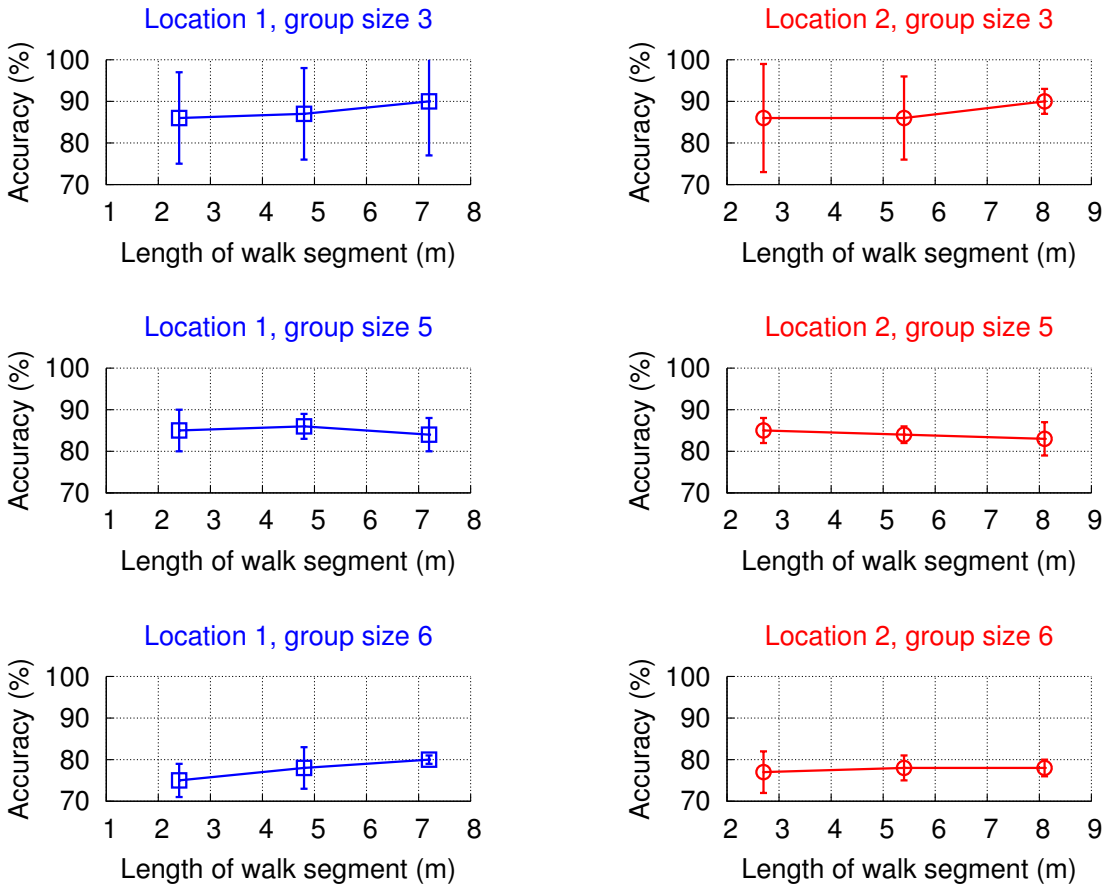


Figure 5.15. The accuracy of identification for different group sizes with different walking lengths

## 5.8 Discussion and Limitations

We now discuss the potential, challenges and limitations of our WiFi-based person identification system.

(1) Walking path: In this work, we have assumed that a person always walks on a straight line path. In a home or an office environment, a straight walkway such as a corridor or hallway can be chosen for the purpose, where a person can get identified at the same time when she enters the home/office.

(2) Detecting a person outside the group: We also evaluate WiWho to detect if a person is not within the training group. WiWho can achieve over 80% accuracy to detect whether the person is “stranger” or not for a group size of 4 or less.

(3) Number of people: Majority of WiFi-based sensing research assumes a single person system like ours. However, this limitation is less severe in our case since it can be assumed that WiWho is deployed in a hallway or a corridor where typically only one person enters the premises at a time.

(4) Diverse set of people: WiWho is currently evaluated only for the age group of 25-30 years.

Previous research such as [72] has shown that a person's gait is dependent on the person's age which means that the attainable accuracy of WiWho is likely to be higher when evaluated with other age groups (e.g., kids or elderly people).

## 5.9 Summary

In this paper, we presented WiWho, a framework for identifying a person using the gait information detected via WiFi. WiWho enables a device-free, effortless, low-cost and pervasive solution for person identification in smart homes and offices. We showed the feasibility of gait identification through CSI and discussed necessary characteristics of CSI-based gait that can identify a person. WiWho achieves an identification accuracy of 92% to 80% for a group size of 2 to 6 respectively and only 2-3 meters walking length is necessary. The limitations and potential of WiFi-based person identification system are also discussed.

# Chapter 6

## Enriching WLANs with MU-MIMO-aware AP Selection System

### 6.1 Introduction

The major Wi-Fi Access Point (AP) vendors worldwide seek to provide ubiquitous, gigabit wireless connectivity, by deploying high-density networks [92, 93], where a large number of clients and APs operate in the same RF coverage zone. A key feature for such deployments is MU-MIMO, which uses beamforming to support multiple, concurrent data streams from an AP to a group of client devices. MU-MIMO feature has already been adopted by the IEEE 802.11ac networks, to realize gigabit downlink speeds. It has been also widely perceived among the primary means to meet the speed requirements of the next generation Wi-Fi 802.11ax [94] and 5G networks [95]. However, MU-MIMO gains can be achieved only if an AP can identify groups of clients with homogenous configurations and orthogonal wireless channels, where concurrent transmissions will not cause inter-client interference. Consequently, MU-MIMO performance is fundamentally depending on how clients will be assigned to APs, which operate in the same coverage zone.

**Limitations of legacy designs:** State-of-the-art AP selection designs proposed by industry [96, 97] and academia [98, 99] assign clients to the strongest signal (RSSI) AP. Interestingly, our experiments with commodity MU-MIMO 802.11ac testbeds show that they yield more than 50% lower network throughput compared to the optimal client assignment. We have identified three root causes for such poor performance. (a) Legacy designs are MU-MIMO oblivious and may assign clients with correlated channels to the same AP. Grouping clients with correlated channels results in high inter-client interference, which forces the AP to operate in SU-MIMO mode (serving one client at a time). (b) Even when clients communicate over orthogonal channels thanks to rich multipath environment, legacy designs may still limit

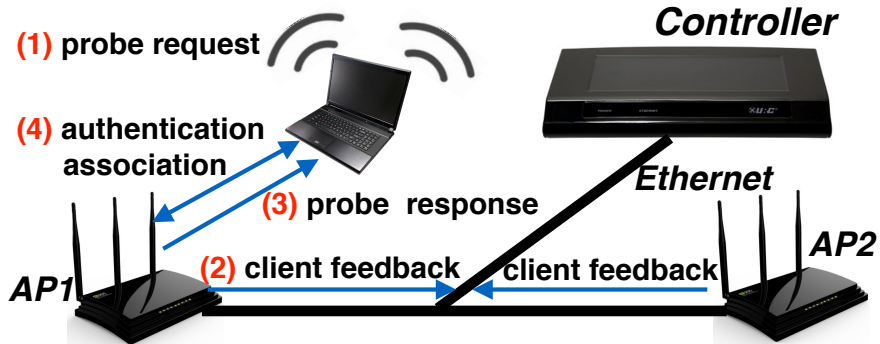


Figure 6.1. Client association in enterprise Wi-Fi.

MU-MIMO grouping opportunities, by assigning clients with heterogeneous bandwidth configurations to the same AP. Specifically, clients which operate on different 802.11ac bandwidth options cannot be grouped together. This constraint is attributed to AP's capability, which can only transmit on a single center frequency and bandwidth at a time. Moreover, the AP cannot always use the highest bandwidth option for transmitting to all the clients in a group, due to clients' different interference profiles. (c) Finally, the widely adopted approach to assign clients to the least "loaded" AP, can limit MU-MIMO gains, even for clients which operate on orthogonal channels and homogenous bandwidths. This is because more loaded APs may offer more grouping opportunities.

**Design challenges:** The design of MU-MIMO-aware AP selection, which addresses the above limitations, poses significant challenges. First, a key design challenge is to identify clients with orthogonal channels and assign them to the same AP. A naive approach would be to associate each client to all APs in its range, and use explicit beamforming feedback [100–102] to estimate channel correlation. However, such an approach requires excessive handoffs in high-density Wi-Fi deployments, and leads to poor performance. Hence, a new, low-overhead approach is required for profiling the multipath environment and estimating channel correlations. Moreover, MU-MIMO-aware AP selection should be able to capture clients' (and APs') bandwidth profiles, which dynamically change in time, due to interferences. Then, it needs to estimate how clients' bandwidth profiles will affect their grouping opportunities at an AP. Finally, AP selection must balance the load among APs, without limiting their MU-MIMO gains, which are often conflicting objectives.

**MAPS design:** In this paper, we propose a new *Mu-mimo-Aware AP Selection (MAPS)* design for 802.11ac networks, which addresses the aforementioned challenges. MAPS leverages a NULL frame probing scheme to collect CSI (Channel State Information) feedback from clients, without requiring

them to associate with APs. CSI samples measured at the AP-side can capture the multipath characteristics of the environment, and can be used as a proxy for clients' channel correlation, as shown by our experiments. MAPS first sanitizes CSI samples by removing the RF-hardware triggered amplitude deviations, using local regression smoothing filters. It then constructs a CSI profile that differentiates between persistent and transient multipath. The CSI profiler applies a correlation metric among back-to-back CSIs, which captures dominant multipath changes, and at the same time remains robust to RF hardware-triggered CSI phase shifts. Using the CSI profile, MAPS can estimate the SINR (Signal-to-Interference-plus-Noise Ratio) and hence the PHY rate of a client as a part of an MU-MIMO group. MAPS' SINR approximation error is typically small (<2 dB) compared to SINR estimation using explicit client's channel feedback.

MAPS introduces a novel client assignment model, which leverages clients' SINR, traffic and interference profiles to infer the effective MU-MIMO throughput of a client, at each AP. Our model can balance between MU-MIMO gains and AP load, by considering the Wi-Fi channel busy time, and the airtime to be allocated to a client, at each AP. MAPS will then assign clients to APs which maximize their throughputs. Since optimal client assignment is an NP-Hard problem, we propose a low-overhead heuristic algorithm, which performs close to optimal, as shown by our experiments.

We evaluate MAPS' performance gains over legacy designs using testbed experiments with 802.11ac commodity APs and MU-MIMO-capable smartphones. Our results show that MAPS outperforms legacy designs in 90% of the settings, with network throughput gains greater than 50%. In the most (~85%) of our experiments, MAPS performs the same as the optimal, best-throughput client assignment. Our simulations using traces from Wi-Fi enterprise networks verify MAPS gains in large scale topologies, where more than 50 clients are connected to an AP.

**Contributions:** In summary, our main contributions are:

- (1) We conduct a measurement study with commodity 802.11ac MU-MIMO testbeds, and identify the limitations of legacy AP selection designs (Sec. 6.3). To the best of our knowledge, this is the first work that studies AP selection in MU-MUMO networks, using commodity 802.11ac testbeds.
- (2) We design MAPS, a practical, 802.11-compliant system, which can boost MU-MIMO gains by appropriately assigning clients to APs. (Sec. 6.4).
- (3) We implement MAPS in 802.11ac commodity hardware (Sec. 6.5), and evaluate its performance in multiple network settings, using 802.11ac APs and smartphone devices (Sec. 6.6).

## 6.2 Background

### 6.2.1 IEEE 802.11ac Background

The key differentiator of 802.11ac over its predecessors is the MU-MIMO feature, which uses beamforming to support concurrent downlink data streams from an AP to a group of clients. An 802.11ac AP can support MU-MIMO beamforming, by using a sounding protocol [103] to collect *VHT Compressed Beamforming Feedback (CBF)* from wireless clients. The CBF is represented by  $V$ , which is a steering matrix that specifies how AP should decorrelate transmitted data to multiple clients. A client calculates  $V$  by applying Singular Value Decomposition (SVD) on  $H$  as  $H = UDV^H$ . Here,  $H$  (or CSI) is the channel matrix measured at the client's side from sounding packet. Then, an AP uses  $V$  to precode the transmission data. Apart from CBF, 802.11ac clients provide SNR (Signal to Noise Ratio) feedback to AP. An 802.11ac AP selects a set of clients to transmit data concurrently through a *client selection* algorithm that precedes sounding and beamforming. Client selection algorithm is vendor-specific and unspecified by the 802.11ac standard. 802.11ac supports 20, 40, 80 MHz channel bandwidths, and an optional 160 MHz bandwidth. An 802.11ac device can use a 20 MHz sub-channel only if it is not occupied by another transmission in its vicinity. An 802.11ac AP can negotiate communication at higher channel widths through an RTS/CTS handshake protocol [103, 104]. Interestingly, *only clients with the same channel bandwidth configuration can be grouped together in the same MU-MIMO group*. This is because an AP can only transmit using a single center frequency and bandwidth at a time. Moreover, clients of different channel bandwidth may have different interference profiles, and hence the AP cannot transmit data to all of them using the highest channel bandwidth.

### 6.2.2 Enterprise Wi-Fi Networks

In this paper, we focus on enterprise Wi-Fi networks where multiple APs operating in infrastructure mode, provide wireless connectivity in large buildings. APs are typically connected through Ethernet to controllers, as shown in Figure 6.1. Controllers support network management, and enterprise applications' security. They also assign clients to APs (i.e., AP selection) and initiate clients' handoffs. Specifically, prior to association, a client  $C$  scans Wi-Fi channels for APs. In *passive* scanning mode,  $C$  listens for beacons. In *active* mode,  $C$  broadcasts probe requests. The APs which receive these requests send information about  $C$  (e.g., RSSI) to the controller, which assigns  $C$  to an AP. The selected AP sends a probe response to  $C$ , which initiates the authentication and association process. If the controller decides to handoff  $C$  from AP1 to AP2, then AP1 sends a disassociate frame to  $C$ , and  $C$  follows the process shown in Figure 6.1.

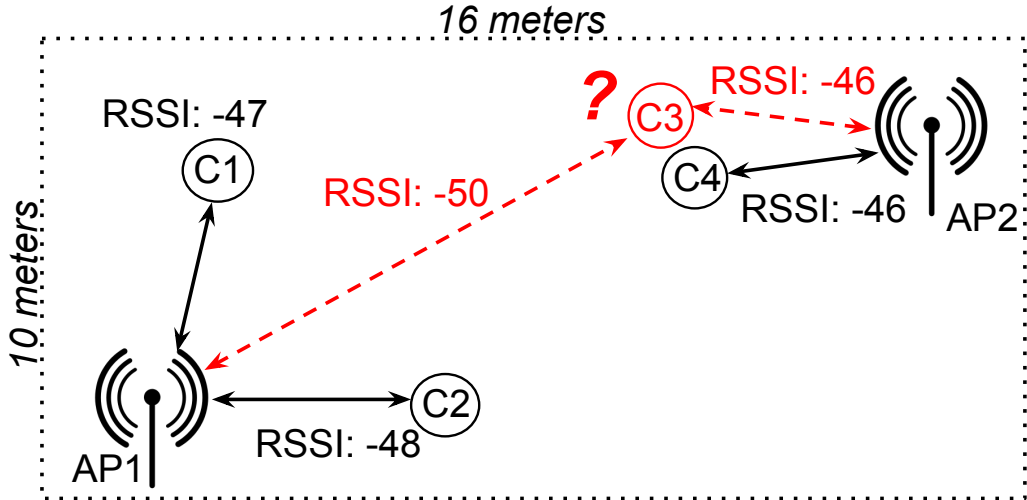


Figure 6.2. Network topology for the case study setting.

## 6.3 A Measurement Study

In this section, we show the limitations of legacy AP selection approaches in MU-MIMO networks, by conducting experiments with 802.11ac commodity wireless testbeds.

### 6.3.1 Platform and Methodology

Our experiments use commodity 802.11ac APs, equipped with a Qualcomm Beeliner 4×4 MU-MIMO-capable 802.11ac 5 GHz radio. The 802.11ac radio supports up to 80 MHz channel bandwidth and up to 256-QAM modulation level, with 1733.3 Mbps peak PHY rate. It has 4 antennas, but supports up to 3 data streams (clients) in MU-MIMO mode. MU-MIMO client selection along with other core MAC-layer functionalities (e.g., PHY rate and bandwidth adaptation) are implemented in the AP's firmware, and the source code is available for our implementation. Our experiments use Xiaomi Mi 4i smartphones as clients, which have an 802.11ac wave-2 chipset, with one receiving antenna.

For our experiments, we have modified the firmware of our APs to collect per-client wireless feedback such as: a) PHY rates (i.e., MCS, spatial stream, channel bandwidth), b) sounding feedback statistics (i.e.,  $V$  matrix, per-subcarrier SNR - cf. Sec. 6.2.2), c) frame error rate, and d) CSI measured at the AP side, from the received frames. We conduct experiments in enterprise and university campus settings.

### 6.3.2 Correlated Wireless Channels

We next show the limitations of legacy AP selection algorithms in typical 802.11ac deployments, with testbed experiments. In our case study setting, clients C1 and C2 are connected to the strongest signal (RSSI) AP1 and C4 to AP2, as shown in Figure 6.2. All clients operate at 80 MHz. C1 and C2 form

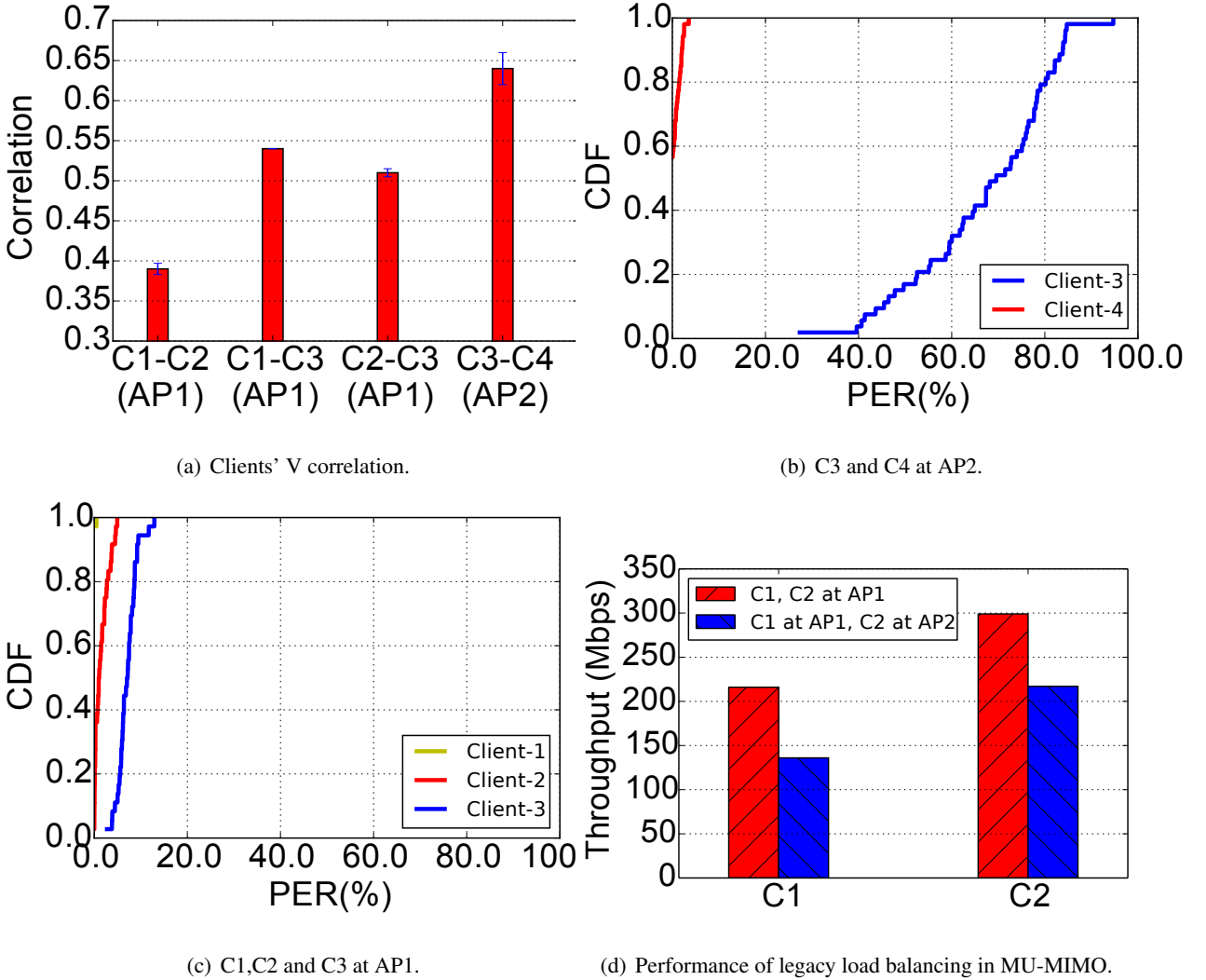


Figure 6.3. a) V correlation, b, c) Packet-Error-Rate, d) throughput for clients in our case study settings.

an MU-MIMO group and achieve 378 Mbps aggregate downlink UDP throughput compared to only 296 Mbps, when they operate at Single-User MIMO (SU-MIMO) (where one client is served at a time). When a new client C3 wants to join the network, legacy (e.g., RSSI-based) designs will assign C3 to the highest RSSI AP2. However, is this the best-throughput client assignment?

Our results show that clients C3 and C4 perform poorly in MU-MIMO mode, at AP2. Specifically, the aggregate downlink throughput at AP2 is 178.8% higher when C3 and C4 operate in SU-MIMO, compared to forming an MU-MIMO group. Hence, C3 cannot leverage MU-MIMO gains by connecting to the highest RSSI AP2. Interestingly, the aggregate (over AP1 and AP2) network throughput is from 50 to 230 Mbps higher when C3 connects to the lower RSSI AP1 (assuming AP1, AP2 operate on orthogonal channels). Particularly, the best-throughput setting is observed when C1, C2 and C3 form an MU-

Table 6.1. Per-client and aggregate (across APs) downlink UDP throughput (Mbps), when C3 connects to AP1, AP2.

Setting	C1	C2	C3	C4	Aggr.
AP1(MU), AP2(MU), C3-AP2	186 ± 5	192 ± 6	9 ± 2	92 ± 21	479
AP1(MU), AP2(SU), C3-AP2	186 ± 5	192 ± 6	147 ± 6	134 ± 5	659
AP1(MU), AP2(SU), C3-AP1	146 ± 2	148 ± 2	145 ± 2	269 ± 5	708

MIMO group at AP1, and C4 operates in SU-MIMO at AP2. The aggregate and per-client throughput for the above settings is summarized in Table 6.1. Client C3 cannot leverage MU-MIMO gains at AP2, because its wireless channel is highly correlated with C4, leading to inter-client interference. Channel correlation (and hence interference) between clients  $i, j$  at subcarrier  $s$ , can be estimated by the  $V$  matrix correlation [100] as:

$$\rho(i, j) = \frac{\sum_s \|V_i(s)V_j^H(s)\|}{\sqrt{\sum_s \|V_i(s)\|^2} \sqrt{\sum_s \|V_j(s)\|^2}} \quad (6.1)$$

Figure 6.3(a) shows that the  $V$  correlation between C3 and C4 ( $\rho(C3, C4)$ ) is 64% higher than that of clients C1 and C2, which gives the best MU-MIMO performance. Highly correlated channels result in inter-client interference and consequently to high Packet-Error-Rate (PER). Figure 6.3(b) shows that the median PER for C3 when grouped with C4 is approximately 70%, and the maximum PER exceeds 90%. On the other hand, the channel correlation among the clients of the MU-MIMO group {C1, C2, C3} at AP1, is lower than {C3,C4}, as shown in Figure 6.3(a). Due to lower inter-client interference, the PER for C3 at AP1 is lower than 10% for 90% of the samples, as shown in Figure 6.3(c). Hence, the best-throughput AP selection algorithm needs to assign C3 to the lower RSSI AP1, in order to leverage the MU-MIMO gains.

**Summary:** RSSI-based AP selection designs are oblivious to MU-MIMO feature, and assign clients to APs, without considering the channel correlation among clients connected to the same AP. Correlated channels lead to high inter-client interference and low throughput, in MU-MIMO settings.

### 6.3.3 Heterogeneous Bandwidth Clients

We next evaluate a two-AP topology setting (similar to Fig. 6.2), where C1 and C2 are connected to AP1 and AP2 respectively. C1 operates at 80 MHz and C2 at 40 MHz (due to the interference from neighboring networks). Let's consider a new client C3 operating at 80 MHz, whose RSSI is -50 dbm and -46 dbm from AP1 and AP2, respectively. RSSI-based designs will assign C3 to AP2, without

Table 6.2. Per-client and aggregate downlink UDP throughput (Mbps) and fairness, for heterogeneous width clients.

Setting	C1	C2	C3	Aggr.	Jain Idx
AP1(SU), AP2(SU), C3-AP2(80MHz)	269 ± 5	80 ± 4	151 ± 5	500	0.82
AP1(SU), AP2(MU), C3-AP2(40MHz)	269 ± 5	127 ± 10	125 ± 10	521	0.87
AP1(MU), AP2(SU), C3-AP1(80MHz)	186 ± 5	161 ± 3	192 ± 6	539	0.99

considering that different bandwidth clients cannot be grouped together (cf. Sec. 6.2.2). Consequently, C2 and C3 will operate at SU-MIMO. On the other hand, C3 could form an MU-MIMO group with C1 at AP1, increasing by 40 Mbps the aggregate network throughput (cf. rows 1, 3 of Tab. 6.2). Even when AP’s bandwidth adaptation algorithm allows for C2 and C3 to form an MU-MIMO group at 40MHz, at AP2<sup>1</sup>, assigning C3 to the lower RSSI AP1 still gives better network throughput, as shown in rows 2, 3 of Table 6.2.

Assigning clients to APs with high MU-MIMO gains can also improve fairness. For example the Jain Fairness Index [105] of the network when C3 operates in SU-MIMO at AP2 is 0.82 (1 implies perfect fairness), while it increases to 0.99, when C3 connects to AP1.

**Summary:** RSSI-based AP selection designs can limit MU-MIMO grouping opportunities, by assigning clients with heterogeneous bandwidths to the same AP.

### 6.3.4 Load Balancing

We finally evaluate a topology of two APs in the same vicinity, operating on the same wireless channel. This is a realistic setting in dense AP deployments, when there are not enough non-overlapping channels for adjacent APs. The approach of assigning the same channel to adjacent APs has been also used by industry [93] for better interference management and faster inter-AP handoff. In our setting, client C1 operating at 80 MHz is connected to AP1, while AP2 does not serve any client. We assume that AP1 fully utilizes the wireless channel capacity to serve C1’s traffic. Let’s now consider a new client C2 operating at 80 MHz, whose RSSI from AP1 and AP2 is the same. Existing designs [98, 99] will assign C2 to AP2, to balance the load among APs. However, such assignment is suboptimal in terms of throughput, as shown in Figure 6.3(d). Clients C1 and C2 operate in MU-MIMO when both are connected to AP1, and achieve 515 Mbps aggregate throughput. However, when connected to different APs, they share the wireless medium, and hence achieve 162 Mbps lower aggregate throughput.

**Summary:** Legacy load balancing designs can reduce MU-MIMO grouping opportunities and hence

---

<sup>1</sup>Commodity 802.11ac APs do not adjust channel bandwidth, to increase MU-MIMO grouping opportunities.

*throughput performance, by assigning clients to the least loaded AP.*

## 6.4 Design

In this section we present *MAPS* (*Mu-mimo-Aware AP Selection*), an 802.11-compliant system, which can boost MU-MIMO gains by appropriately assigning clients to APs. MAPS seeks to increase MU-MIMO grouping opportunities by setting three key design goals: (a) to accurately identify clients with uncorrelated channels at low overhead, and assign them to the same AP, (b) to assign clients with homogenous bandwidth settings to the same AP, by monitoring their interference profiles, (c) to allow for client assignment to more “loaded” APs, if they can form high-throughput MU-MIMO groups. MAPS is a practical, lightweight design, which can be implemented in commodity 802.11ac hardware, without client-side modifications.

**MAPS architecture:** An overview of MAPS is shown in Figure 6.4. MAPS takes an implicit feedback approach to identify clients with uncorrelated channels, without requiring them to be associated to an AP. It leverages a NULL data probing scheme to collect CSI samples at APs for each client in their vicinity. The compressed CSI samples are sent to the controller, which upon sanitizing them, it constructs the dominant multipath profile of a client, at each AP. The controller uses a client’s CSI profile to estimate its performance (i.e., PHY rate) as a member of an MU-MIMO group. A MAPS’ AP further maintains client’s bandwidth and traffic profiles, which along with AP’s Wi-Fi channel busy time and load, are used to estimate the throughput of a client at an AP. When a new client wants to join the network, or a client’s handoff is required, MAPS’ controller identifies the APs in client’s range, and assigns it to the AP which maximizes its throughput. Then, it sends its decision to the selected AP, which uses the MAC Sublayer Management Entity (MLME), to associate the client to itself. We next elaborate on MAPS’ building blocks.

### 6.4.1 MU-MIMO Performance Inference

A key challenge for MAPS is to identify clients with uncorrelated channels, and map them to the same AP. A naive approach would be to periodically associate each client to all APs in its range, and collect CBF to estimate clients’ channel correlation. However, such approach requires frequent handoffs and long associations with low-throughput APs. Given the dense Wi-Fi deployments with multiple APs in a client’s range and the long handoff times (order of seconds), explicit feedback approach will perform very poorly. Hence, MAPS takes an implicit feedback approach.

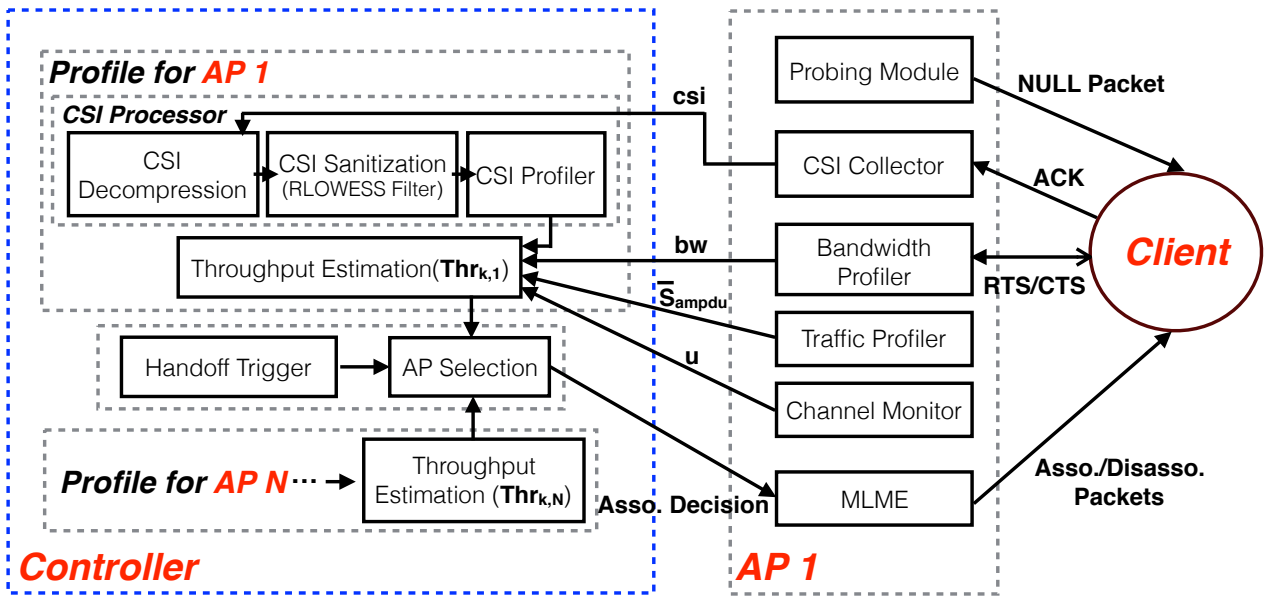


Figure 6.4. MAPS architecture.

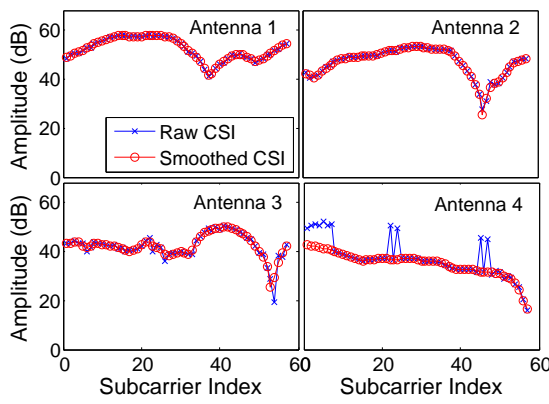
#### 6.4.1.1 Leveraging Implicit Feedback

MAPS uses implicit, AP-side, CSI feedback to identify MU-MIMO groups of clients with uncorrelated channels. Intuitively, since the “physical” wireless channel is reciprocal [106], CSI measured at the AP can capture the correlation among clients’ channels. However, leveraging AP-side CSI poses several challenges. How can an AP collect CSIs from clients not associated with it? Is it possible to filter Wi-Fi RF-hardware triggered noises of the collected CSI samples? How to construct a CSI profile that captures both persistent and transient multipath characteristics of the environment? We next describe MAPS’ approach to such challenges.

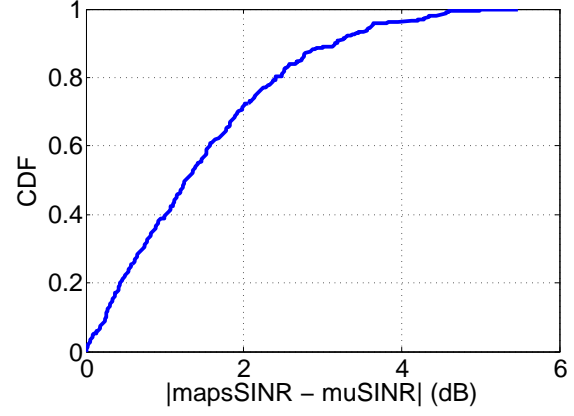
**CSI collection:** MAPS leverages a NULL data probing scheme to collect CSIs from the clients in AP’s vicinity. Specifically, an AP transmits NULL frames, and estimates the CSI from the ACKs sent by the client. A CSI sample is a  $N_t \times N_r$  matrix of complex numbers reported per OFDM subcarrier, where  $N_t$  and  $N_r$  are the number of antennas at the AP and client. A client will respond to a NULL frame received by an AP, even if it is not connected to this AP, as verified by our experiments.

NULL probing is a low overhead CSI collection scheme. Particularly, a NULL frame is only tens of bytes (depending on the 802.11 family). Hence, its transmission time is only 0.85 microseconds, for the smartphones used in our testbed. This overhead is negligible considering that MAPS only periodically (every 100ms) transmits NULL frames.

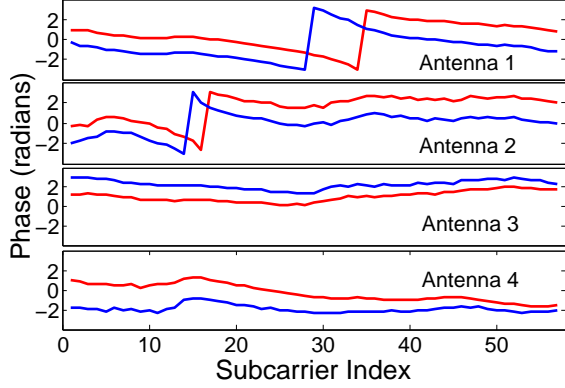
**CSI sanitization:** Our measurements show that CSIs reported by commodity APs can be noisy. Such



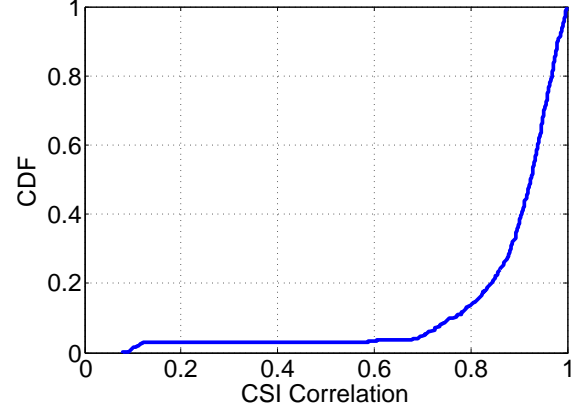
(a) Robust LOWESS filter on CSI samples.



(b) Implicit SINR vs. muSINR in multiple settings.



(c) Phase shift for 2 back-to-back frames.



(d) CSI correlation for back-to-back frames.

Figure 6.5. MAPS' CSI profiling.

noise is attributed to transmission power changes, rate adaptation, internal CSI reference level changes [107]. For example, Figure 6.5(a) shows that noise spikes can exceed 10 dB. MAPS applies a robust *LOWESS* (Locally Weighted Scatterplot Smoothing) filter [108], which performs local regression with weighted least squares to smoothen outliers. Non-parametric smoothers like LOWESS are appropriate for CSIs, since they do not assume that the data fit some distribution shape. Figure 6.5(a) shows that such filter removes noise from CSIs.

The smoothed CSI is used to estimate the SINR of a client  $k$  operating in an MU-MIMO group of  $K$  clients as [100]:

$$SINR = \frac{\underbrace{\frac{1}{K} \|D_k\|^2}_{signal\_power}}{\underbrace{\underbrace{\sum_{j=1}^N \|D_j\|^2}_{noise\_floor} + \underbrace{\frac{1}{K} \|D_k\|^2 \sum_{j \neq k} \|V_k^H V_j\|^2}_{interference}}_{interference}} \quad (6.2)$$

MAPS estimates  $V$  and  $D$  by applying SVD on CSI (cf. Sec. 6.2.2). It computes the noise  $N$  using EVM (Error Vector Magnitude) feedback, provided by AP's firmware, for every received frame across all subcarriers. Finally, it calibrates  $D_k$  to account for the transmit power difference between the client and AP. Specifically, it multiplies the factor  $\|D_k\|^2$  with  $10^{\frac{P_{AP}-P_{client}}{10}}$ , which is the transmit power difference (dBm) at AP and client sides.  $P_{client}$  is available at the AP through 802.11 Event Report frames. Notice that the SINR metric can be estimated per OFDM subcarrier. MAPS computes an *effective SINR* across all subcarriers using the approach proposed in [109], which has been shown to be robust in frequency-selective fading environment.

**SINR accuracy:** We evaluate our SINR metric's accuracy, by comparing it with muSINR [100], which uses explicit, receiver-side  $V$  and  $D$  feedback (CBF). Figure 6.5(b) shows the distribution of the absolute difference between the two SINR metrics, from multiple experimental settings. We observe that for 70% of the cases, the SINR estimation error is less than 2 dB. This error will not lead to erroneous PHY rate estimation most of the times (cf. Tab. 22-25 in [103]), and hence it does not affect MAPS' ability to infer client's throughput. Since MAPS' SINR estimation is not used for core functions such as rate adaptation, estimation error outliers will not significantly impact MAPS' performance, as shown by our evaluation results (cf. Sec. 6.6).

#### 6.4.1.2 Identifying Dominant Multipaths

MAPS' operations are triggered at coarser time scales (sec.) compared to other CSI-based algorithms, such as MU-MIMO grouping (msec.), to avoid excessive handoffs. Hence, instead of simply maintaining the latest CSI, MAPS needs to construct a CSI profile which captures both persistent and transient multipath characteristics of the environment.

Constructing a CSI profile is a challenging task. First, storing and processing all the measured CSIs (collected at msec. scales) is a big overhead even for a Wi-Fi controller. Hence, MAPS needs to consider only CSIs that capture multipath changes. However, capturing such dynamics is not trivial. Even if the multipath characteristics of the environment remain the same, the phase of back-to-back CSI samples may vary due to Wi-Fi RF hardware characteristics [106, 107]. A CSI profiler should be robust to such variations and capture only significant multipath changes.

Interestingly, different from related studies [106], our experiments show that such phase variations are not random. For example, Figure 6.5(c) shows the phase curves of two back-to-back frames, in a controlled environment with no object movement. We observe an almost constant phase shift for all subcarriers (y-axis), and a small shift in phase curve across frequency domain (x-axis), for antennas 1,

2. However, we observe similar shapes of phase curves. Since the hardware-triggered phase shifts do not change the shape of the phase curves of back-to-back frames, we expect that their correlation will be high. Figure 6.5(d) shows the distribution of the correlation factor  $\rho$  (eq. (6.1)) for CSIs, collected from multiple settings in a time window of 0.5 msecs, of stable multipath environment<sup>2</sup>. We observe that for 80% of the cases,  $\rho$  is equal or greater than 0.85 ( $\rho = 1$  for same CSI samples).

While CSI correlation metric is robust to hardware-triggered phase shifts, it can also capture changes in multipath environment. We illustrate our point by studying the spatial distribution of CSIs (in polar coordinate system) in cases of stable (Fig. 6.6(a)) and dynamic (Fig. 6.6(b)) multipath environments. For stable multipath, back-to-back CSIs overlap in space, which is reflected in their CSI correlation. For dynamic multipath, the CSIs' main lobes do not overlap (cf. Fig. 6.6(b)), as indicated by their lower correlation.

MAPS leverages the CSI correlation metric to maintain  $L$  dominant multipaths (i.e., CSIs). For each new CSI  $i$ , MAPS estimates its correlation  $\rho(i, j)$  with each CSI  $j$ , of current CSI profile. If the maximum correlation with a CSI  $j$  is greater than a threshold ( $\max_{j \in L} \{\rho(i, j)\} > R$ ), then MAPS replaces CSI  $j$ , with  $i$  and increases a counter  $csi_j$  ( $j$  is an index of the CSI profile)<sup>3</sup>. Otherwise, the new CSI is stored in a new entry of the profile. If the CSI profile is full (with  $|L|$  CSIs), MAPS will either replace an existing CSI  $j$  with the new CSI, if  $csi_j = 1$ , or it will discard  $i$ . MAPS periodically resets CSI profiles to allow for new multipaths.

MAPS needs to estimate clients' SINRs for all the MU-MIMO group assignments, to select the best AP (cf. Sec. 6.4.3). However, a client's SINR will change for each CSI in its profile. Processing all CSIs for all groups, results in significant processing overhead. MAPS amortizes such overhead, using the counter  $csi_i$ , which reflects the "dominance" of a multipath. It selects as client's dominant multipath, its CSI  $i$  with a probability  $P_{csi_i} = csi_i / \sum_{j=1}^{|L|} csi_j$ . Then, it uses the dominant CSI for computing the SINR. Client's SINR along with its bandwidth and traffic profiles are used for estimating client's throughput at an AP, as we discuss next.

#### 6.4.2 Client and AP Profiling

MU-MIMO grouping opportunities depend on clients' bandwidth configuration (cf. Sec. 6.3.3) and traffic profiles.

**Bandwidth profile:** MAPS monitors the interference profile of each AP and client, and connects ho-

---

<sup>2</sup>We compute  $\rho$  by using CSI  $H$  instead of  $V$  in eq. (6.1).

<sup>3</sup> $R$  can be set to 0.85, from our experiments in Fig. 6.5(d).

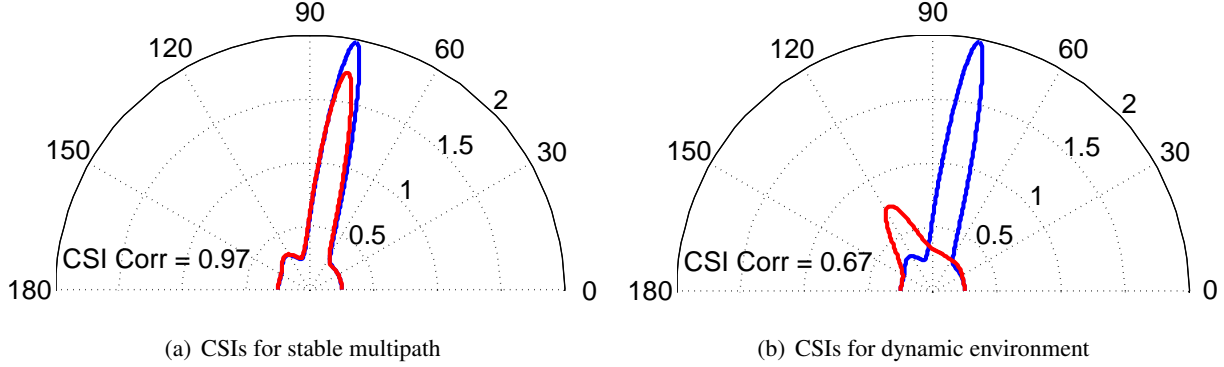


Figure 6.6. Signal spatial distribution for stable and dynamic channels.

mogenous bandwidth clients to the same AP. Particularly, it maintains for each device, the number of transmissions or receptions that could use the bandwidth option  $bw \in \{20, 40, 80, 160\}$ . MAPS estimates  $bw$ , by monitoring which 20 MHz sub-channels are occupied through the RTS/CTS handshake process. Since, a device's interference profile (and hence bandwidth) may change at runtime, MAPS selects  $bw_k$  for a device  $k$ , to be the bandwidth option with the highest probability. The probability of a bandwidth  $i$  is estimated as:

$$P_{bw^i} = \frac{\# \text{Packets}_{bw^i}}{\sum_{j \in \{20, 40, 80, 160\}} \# \text{Packets}_{bw^j}} \quad (6.3)$$

MAPS maintains different bandwidth profiles for different channels that APs may operate on. It periodically resets bandwidth profiles, to account for new interference dynamics. Finally, it computes the bandwidth configuration of a client  $k$  at an AP  $\alpha$  as:  $bw_{k,\alpha} = \min\{bw_k, bw_\alpha\}$ .

**Traffic profile:** MAPS monitors the size of 802.11ac aggregated frames (i.e., A-MPDU) to capture traffic dynamics. It maintains a moving average of a client's A-MPDU size as:

$$\bar{S}_{ampdu} = (1 - \beta) \cdot \bar{S}_{ampdu} + \beta \cdot S_{ampdu} \quad (6.4)$$

where  $\beta = 1/8$  in our implementation. It periodically ages the traffic profile as:  $\bar{S}_{ampdu} = (1 - \beta) \cdot \bar{S}_{ampdu}$ , to consider client's idle time. Typically, small  $\bar{S}_{ampdu}$  implies low traffic.

MAPS also maintains the wireless channel utilization  $u_\alpha$  and the number of clients connected to each AP  $\alpha$ . It captures the AP's channel busy time with a factor  $u_\alpha \in [0, 1]$ , which is the fraction of free transmission cycle opportunities within the last 10 beacon intervals. We next show how such profiles are used to estimate clients' throughput.

### 6.4.3 AP Selection Model

MAPS introduces a novel client assignment model, which can boost MU-MIMO gains. It first leverages clients' profiles to estimate the effective throughput performance of a client, at each AP. Then, it selects the AP which can maximize a client's throughput. We next elaborate on our model.

#### 6.4.3.1 Throughput Model

MAPS estimates the throughput of a client  $k$  at an AP  $\alpha$ , considering: (1) client's PHY rate  $r_{k,\alpha}$ , when it operates in an MU-MIMO group at  $\alpha$ , (2) client's traffic  $\bar{S}_{ampdu,k}$ , (3) 802.11 protocol overheads ( $t_o$ ), (4) channel busy time  $u_\alpha$ , and (5) airtime allocated to client  $w_{k,\alpha}$ . Specifically, it is:

$$Thr_{k,\alpha} = w_{k,\alpha} \cdot u_\alpha \cdot \frac{\bar{S}_{ampdu,k}}{t_d + t_o} \quad (6.5)$$

The factor  $u_\alpha \in [0, 1]$  captures the WiFi channel busy time. The amount of client's data  $\bar{S}_{ampdu,k}$  is computed based on equation (6.4). The time consumed by 802.11 protocol overheads (e.g., sounding, ACK) is  $t_o$ . Finally, the data transmission time is modeled as  $t_d = t_{plcp} + \bar{S}_{ampdu,k}/r_{k,\alpha}$ , where  $t_{plcp}$  is the PLCP preamble transmission time, and  $\bar{S}_{ampdu,k}/r_{k,\alpha}$  is the frame transmission time, where  $r_{k,\alpha}$  is the PHY rate.

PHY rate  $r_{k,\alpha}$ : For a given MU-MIMO group, MAPS first estimates client's SINR from equation (6.2). Then, it uses the 802.11ac rate tables [103] to map the SINR to a PHY rate  $r_{k,\alpha}$  (i.e., MCS, spatial streams). However, a client can form multiple different MU-MIMO groups at each AP. These groups may change in time, depending on clients' channel correlation characteristics, bandwidth and traffic profiles. Hence, to estimate  $r_{k,\alpha}$ , MAPS first needs to estimate which are likely going to be  $k$ 's MU-MIMO groups at AP  $\alpha$ .

In practice, only the best-throughput MU-MIMO groups of traffic active clients are used for transmission. To this end, MAPS considers only the active clients (i.e.,  $\bar{S}_{ampdu} > 0$ ) as candidates for grouping. Then, it computes the set of MU-MIMO groups  $G_\alpha$  that can be formed by the active clients associated to an AP  $\alpha$ , subject to the bandwidth constraint. Here, a group  $g \in G_\alpha$  is a set of clients of cardinality of at least one ( $|g| \geq 1$ ). From all the possible MU-MIMO group combinations  $G_\alpha$ , an AP serves only the best-throughput MU-MIMO groups, while ensuring that all clients will be fairly served. Given a set of clients  $K_\alpha$  at AP  $\alpha$ , a fair allocation will assign  $k$  at least  $1/|K_\alpha|$  of the airtime. MAPS satisfies the above constraints, by first ordering the set  $G_\alpha$ , in decreasing MU-MIMO group throughput order<sup>4</sup>.

---

<sup>4</sup>Group throughput is estimated from eq. (6.5), by considering the group's total transmitted data and transmission time.

Then, starting from the highest throughput group  $g \in G_\alpha$ , MAPS adds  $g$  to a new set  $G'_\alpha$ , subject to two constraints:

- (a) Group  $g$  cannot be a proper subset (or superset) of existing groups in  $G'_\alpha$ :  $\forall g_i, g_j \in G'_\alpha$  then  $g_i \not\subseteq g_j$ .
- (b) Every client associated to the AP  $\alpha$  must belong to at least one group in  $G'_\alpha$ :  $\forall k \in K_\alpha$  then  $k \in g$  for  $g \in G'_\alpha$ .

The above algorithm selects the best-throughput sets, while ensuring that all clients will be served at least once. Hence, the set  $G'_\alpha \subset G_\alpha$  includes the MU-MIMO groups which will be likely served by the AP. Note that MAPS can leverage any of the techniques proposed in the literature [100, 102] to identify  $G'_\alpha$ , at low computational cost.

Now, let's assume that  $G'_{k,\alpha} \subseteq G'_\alpha$  is the subset of groups which include client  $k$ . Then, we estimate  $r_{k,\alpha}$  as the average client's PHY rate when it is part of the groups  $g \in G'_{k,\alpha}$ :  $r_{k,\alpha} = \frac{1}{|G'_{k,\alpha}|} \cdot \sum_{g \in G'_{k,\alpha}} r_{k,\alpha}^g$ . Allocated airtime  $w_{k,\alpha}$ : MAPS uses a weight  $w_{k,\alpha}$  to capture the airtime to be allocated to client  $k$ , at AP  $\alpha$ . Factor  $w_{k,\alpha}$  depends on number of groups which are likely to be served by AP  $\alpha$  (i.e.,  $|G'_\alpha|$ ), or by other APs in  $\alpha$ 's vicinity, operating on the same channel. Specifically, the airtime to be allocated to a client  $k$  at  $\alpha$  is the cardinality of subset of groups that include  $k$  ( $G'_{k,\alpha} \subset G'_\alpha$ ), to the total number of groups. Hence, we set  $w_{k,\alpha}$  to be equal to  $|G'_{k,\alpha}|/|G'_\alpha|$ . For example, in the case study scenario of Figure 6.2,  $G'_{AP1} = \{\{C1, C2, C3\}\}$ ,  $G'_{AP2} = \{\{C4\}\}$  when C3 connects to AP1, and  $G'_{AP1} = \{\{C1, C2\}\}$ ,  $G'_{AP2} = \{\{C3\}, \{C4\}\}$  when C3 connects to AP2. Hence, C3 will get more airtime at AP1 ( $w_{C3,AP1} = 1$ ), compared to AP2 ( $w_{C3,AP2} = 1/2$ ). Note that, if a set of APs  $A$  in the same vicinity with  $\alpha$  operate on the same channel, then  $w_{k,\alpha} = |G'_{k,\alpha}| / \sum_{a' \in A} |G'_{a'}|$ .

In conclusion, MAPS' throughput model can capture inter-client interference and client's bandwidth profile with the rate factor  $r_k$ . It captures Wi-Fi channel utilization  $u_\alpha$ , and prevents client assignment to APs with congested channels. Finally, it captures the "load"  $w_\alpha$  at each AP (or APs in range, on the same channel), which is required for *load balancing*. Our AP platform maintains all the per-client state, which is required for throughput estimation.

#### 6.4.3.2 Client Assignment Model

MAPS' objective is to determine the proper client-AP association set  $K_\alpha$ ,  $\forall \alpha \in A$ , such that the sum-throughput of all clients can be maximized. This optimization problem can be formulated as:

$$\begin{aligned}
I^* = \operatorname{argmax}_I & \sum_{k \in K} \sum_{\alpha \in A} I_{k,\alpha} Th_{k,\alpha} \quad \text{subject to} \\
& \sum_{\alpha \in A} I_{k,\alpha} \leq 1, \forall k \in K \\
& I_{k,\alpha} \in \{0, 1\}, \forall k \in K, \forall \alpha \in A
\end{aligned} \tag{6.6}$$

where the binary variable  $I_{k,\alpha}$  indicates whether a client  $k$  associates with an AP  $\alpha, \forall \alpha \in A$ . Such constraint ensures that each client associates with at most one AP.

We prove that our problem is *NP-Hard*, by reducing a simple instance of it, to the maximum independent set problem. We describe the reduction in our technical report [110]. Hence, we propose a heuristic algorithm that seeks to maximize the aggregate clients' throughput (eq. (6.6)), while satisfying all the constraints. The algorithm operates as follows.

**Profiling:** MAPS periodically updates each client's and AP's profile. CSI profiles are updated every 100 ms, upon NULL frame transmission. Bandwidth profiles are updated upon RTS/CTS handshake, while traffic activity is updated on per A-MPDU basis.

**Handoff trigger:** MAPS associates a timer with each client  $k \in K$ . It triggers AP selection for  $k$ , when its timer expires, or when a special event occurs. Since handoff process lasts approximately for 1.5 seconds in our testbed, MAPS sets client's timer in the order of tens of seconds. It freezes the timer for very low traffic clients (i.e.,  $\bar{S}_{ampdu} \approx 0$ ), to prevent frequent handoffs. It also defers handoff process, when delay-sensitive traffic (e.g., VoIP) is in progress. Client assignment is also triggered upon client's mobility. MAPS detects mobility through SNR variations. By using both timers and events for handoff trigger, MAPS remains adaptive to channel dynamics, without triggering excessive handoffs.

**Group formation:** Upon triggering handoff for client  $k$ , MAPS will identify the set of APs in its range. To reduce the MU-MIMO group formation computational overheads, MAPS excludes in advance APs with very low RSSI, since they will likely be sub-optimal in terms of throughput. Then, it calculates the set of groups  $G'_\alpha$  (and  $G'_{k,\alpha}$ ) for APs in  $k$ 's range, using the greedy search approach proposed in [100]. In summary, it first sorts in descending order, the clients based on their SU-MIMO throughput, and iteratively goes through the list, to group the clients that provide the highest aggregate throughput with the already selected clients. The search terminates when the group is complete, or when adding more clients to a group results in lower throughput than serving them in SU-MIMO mode. Finally, MAPS computes  $k$ 's throughput at AP  $\alpha$  from equation 6.5. It assigns  $k$  to the AP which maximizes its throughput.

Our experimental results show that MAPS heuristic algorithm performs very close to the optimal AP

selection.

#### 6.4.4 Discussion

**Downlink throughput:** MAPS seeks to improve downlink network throughput. This is because 802.11ac MU-MIMO is only supported in downlink direction, which dominates the uplink, in Wi-Fi networks [111]. However, improving downlink throughput, allows for more airtime (and hence better throughput) in uplink transmissions as well.

**Co-existence with existing AP functions:** MAPS can work in concert with existing AP core functionalities, such as MU-MIMO grouping and rate adaptation algorithms. MAPS' SINR estimation could be also used for even improving such algorithms. We leave such extensions for future work.

**Legacy clients:** MAPS seeks to optimize the assignment of IEEE 802.11ac MU-MIMO-capable clients to APs. Legacy 802.11a/b/g/n clients are assigned to APs, based on legacy algorithms. However, MAPS' throughput model still considers the load offered by legacy clients connected to an AP.

### 6.5 Implementation

Our AP's firmware has access to only 960 KB on chip memory, whose 98% is already occupied by various functions. Given that one decompressed CSI sample requires 3.6 KB memory space, storing multiple CSIs for all connected clients in AP's firmware is not feasible. Constructing CSI profiles in the more powerful AP's "host" board, which runs on a dual core 1.4 GHz CPU with a 512 MB DDR3 memory may overload the AP. Instead, MAPS constructs clients' CSI profiles at the controller, considering that all data packets are going through the controller and CSI communication overhead is small. However, due to their low memory requirements, we still implement clients' bandwidth and traffic profiles, and maintain channel busy time statistics, in AP's firmware. The rest of MAPS' functionality is implemented (using MATLAB) at the controller, as shown in Figure 6.4. Our controller is a laptop with 8GB DDR3 memory and 4 Intel core i7-3520M CPU. Note that our implementation does not include the MLME module and hence does not support real time handoff. To this end, upon estimating the best AP-client assignments, we manually assign clients to these APs, and then evaluate the network's performance.

### 6.6 Evaluation

In this section, we evaluate MAPS, using testbed experiments and trace-driven simulations. We compare MAPS with DenseAP [99], which is representative of legacy AP selection designs proposed by research studies, and deployed by AP vendors. DenseAP uses an available capacity metric, which estimates the throughput as a function of PHY rate (calculated from RSSI) and Wi-Fi channel busy time. It seeks to

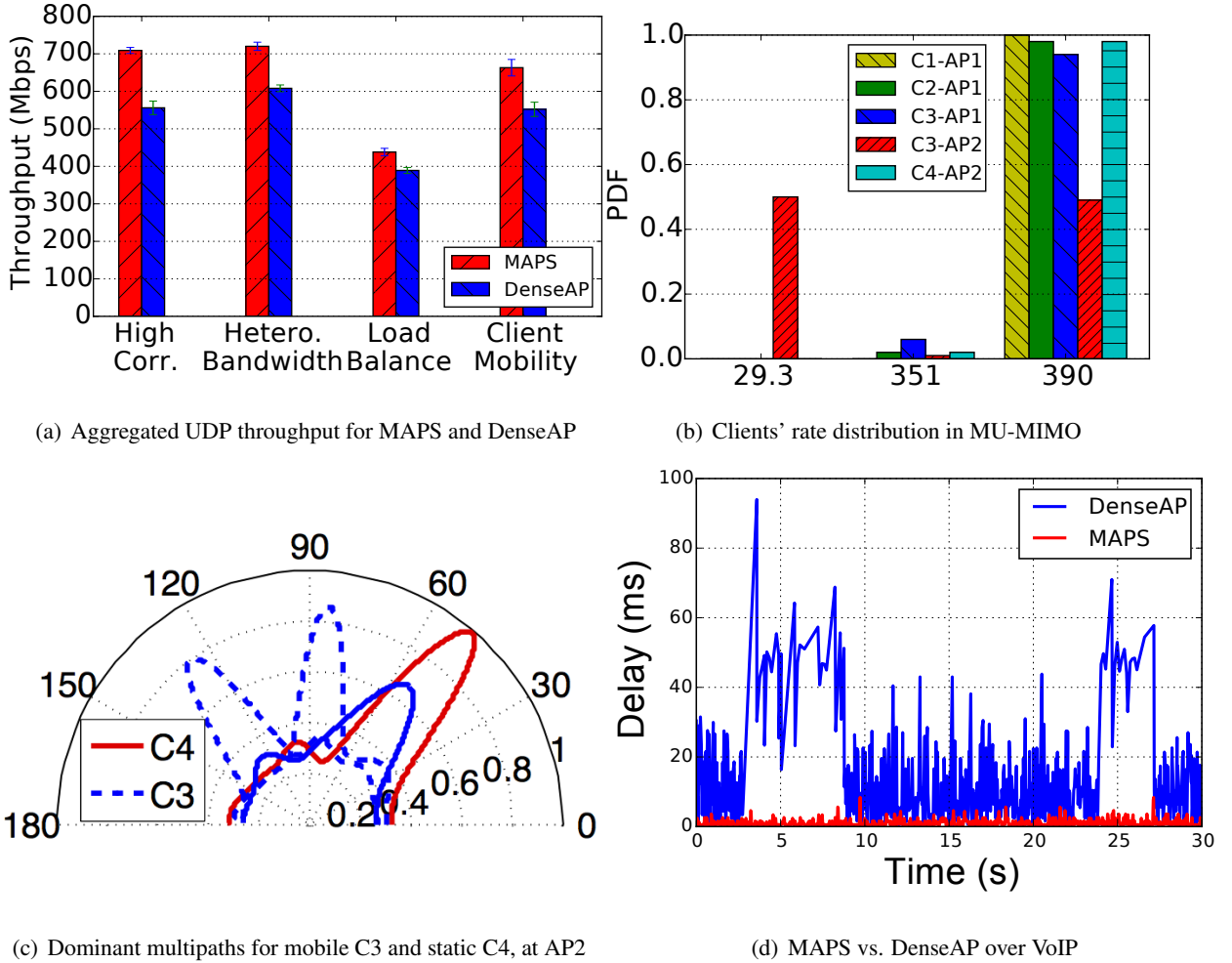


Figure 6.7. MAPS and DenseAP performance in representative settings. MAPS performs similar to Oracle.

balance the load by assigning clients to less loaded APs<sup>5</sup>. We also compare MAPS with an “Oracle”, which is the best-throughput (optimal) client assignment. Oracle finds the best setting through exhaustive search. Our experimental setup consists of the 802.11ac APs and phones described in Section 6.3.1. We evaluate multiple topologies, under various traffic scenarios (UDP, TCP, VoIP).

### 6.6.1 Performance in Representative Settings

We first evaluate MAPS’ performance in four representative settings, which capture different aspects of dynamics in 802.11ac networks. We consider that APs generate saturated downlink UDP traffic to clients, and that they operate on orthogonal channels, unless it is explicitly mentioned.

**Correlated channels:** We first evaluate MAPS in our case study setting of Figure 6.2. Similar to Oracle,

<sup>5</sup>DenseAP performs transmit power control, which is out of the scope of this work.

Table 6.3. CSI correlation for case study setting.

Setting	C1-C2	C1-C3	C2-C3	C3-C4
CSI Corr	0.42	0.51	0.48	0.72

MAPS can identify the best-throughput client assignment, and achieves 153 Mbps (or 27.5%) aggregated throughput gain compared to DenseAP, as shown in Figure 6.7(a). Specifically, MAPS can identify the high correlation of C3, C4's wireless channels at AP2, by computing their CSI correlation and SINR values. The correlation factor  $\rho(C3, C4)$  is 41% and 50% higher compared to  $\rho(C1, C3)$  and  $\rho(C2, C3)$ , as shown in Table 6.3. Such high correlation does not allow for MU-MIMO operation at AP2. Hence, MAPS will assign C3 to AP1.

DenseAP will falsely assign C3 to the highest RSSI AP2. Although the SU-MIMO is the best mode for such assignment (cf. Tab. 6.1), we observed that the AP's MU-MIMO client grouping algorithm will periodically try to evaluate the performance of the group  $\{C3, C4\}$ . However, this will result in high inter-client interference and high PER (cf. Fig. 6.3(b)). When C3, C4 are grouped together, AP's PHY rate adaptation switches to low PHY rates to cope with such interference. This is shown in the rate distribution Figure 6.7(b), where the AP2 often uses the lowest available 802.11ac rate (29.3 Mbps) to transmit to C3. However, when MAPS assigns C3 to the lower RSSI AP1, the selected PHY rate is mostly 390 Mbps, which results in higher throughputs.

**Heterogeneous bandwidths:** We next evaluate MAPS with heterogeneous bandwidth clients. We deploy two APs and five clients. C1 and C2 are connected to AP1 operating at 80 MHz. C4 and C5 are connected to AP2. Due to interferences, C4 and C5 operate at 40 MHz. A new client C3 has a stronger RSSI with AP2, than AP1. Hence, DenseAP will assign C3 to AP2 without considering that, C3 cannot form an 80 MHz MU-MIMO group at AP2. C3's throughput is 79 Mbps at AP2, while the total network throughput is 608 Mbps (cf. Fig. 6.7(a)). However, MAPS can identify the opportunity of a high throughput MU-MIMO group  $\{C1, C2, C3\}$  at 80 MHz, and assigns C3 to AP1. Associating with AP1, C3 achieves 156 Mbps throughput, with a total network throughput of 720 Mbps. Leveraging client's bandwidth profile, MAPS can almost double C3's throughput. It also boosts total network throughput by 112 Mbps (18.4%) compared to DenseAP. MAPS performs the same as Oracle.

**Mobility:** We next study MAPS' responsiveness to mobility. We deploy two APs, three static and one mobile client. Static clients C1, C2 are associated with AP1, and C4 with AP2. C3 is moving with pedestrian speed around AP2. Our traces show that the highest RSSI AP for C3 is always AP2.

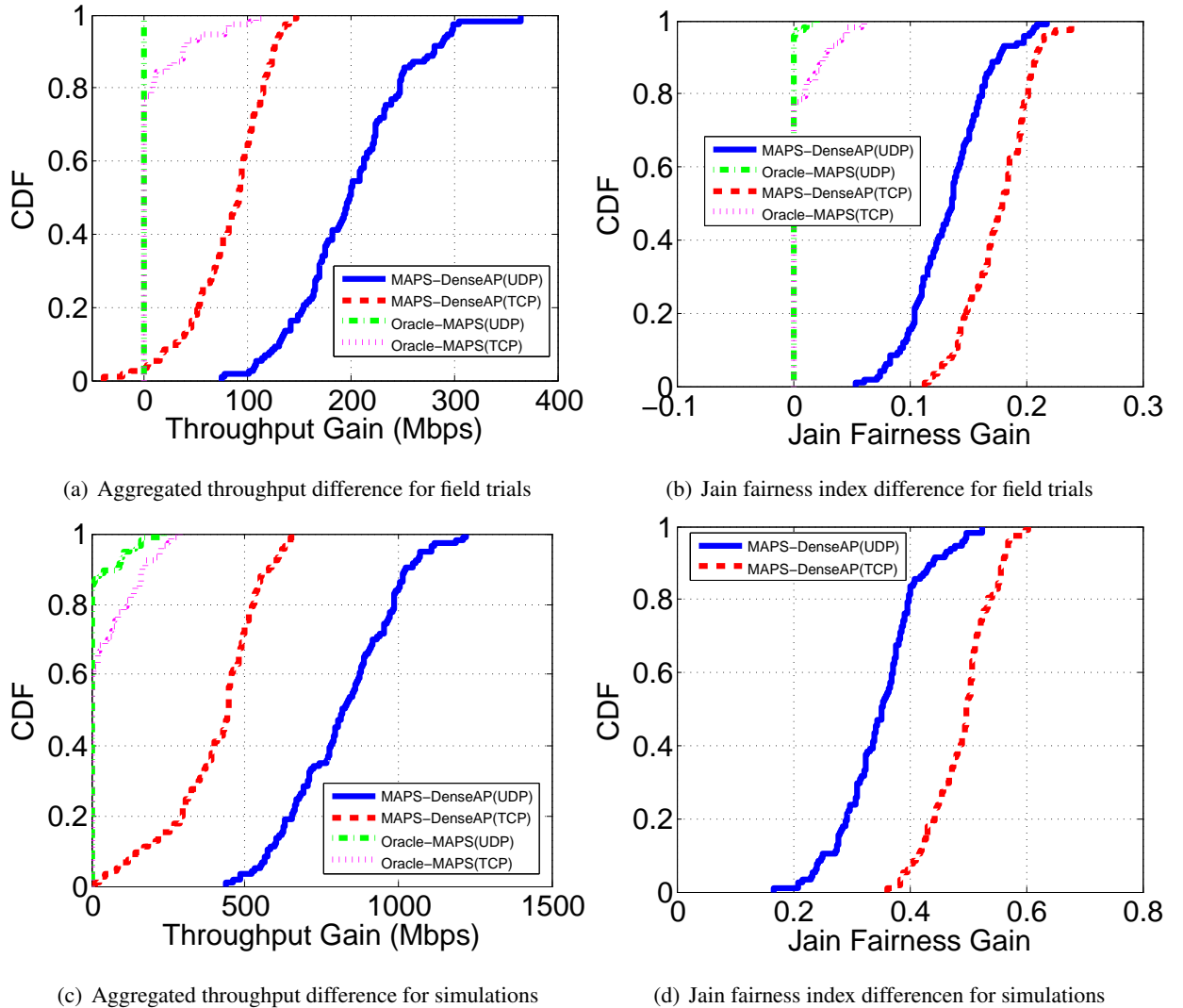


Figure 6.8. Throughput and fairness comparison of MAPS, Oracle and DenseAP.

Hence, DenseAP assigns C3 to AP2. This results in 65 Mbps throughput for C3 and 552 Mbps network throughput.

MAPS monitors the channel dynamics of the mobile client C3, and constructs a CSI profile for AP2 with three dominant multipaths, as shown in Figure 6.7(c). The most dominant path among the three is represented with the solid line. Interestingly, C3 and C4 channels overlap in space at AP2 (cf. Fig. 6.7(c)), which implies correlated channels and high inter-client interference. To avoid client groups with correlated channels, MAPS will assign C3 to AP1. C3 achieves 91 Mbps throughput at AP1, and the aggregated network throughput is 663 Mbps (cf. Fig. 6.7(a)). This corresponds to a throughput gain of 40% for C3, compared to DenseAP. Network throughput is also increased by 20.1%.

**Unbalanced traffic:** Different from the previous experiments, we next evaluate a setting where two APs

operating on the same channel, have unbalanced loads. Specifically, clients C1 and C2 are connected to AP1, while AP2 does not serve any client. Let's now consider a new client C3 in the network, with similar RSSI from AP1 and AP2. DenseAP will assign C3 to AP2, to balance the load across APs. Such assignment results in 75 Mbps and 389 Mbps throughput for C3 and for the network, respectively. On the other hand, MAPS will estimate factor  $w_{C3,AP1}$  to be equal to 1, and  $w_{C3,AP2}$  to be 1/2. Hence, given a negligible inter-client interference among C1, C2, C3 at AP1, MAPS will assign C3 to AP1. Such assignment almost doubles C3's throughput. It also increases the network throughput by 50 Mbps.

**Delay-sensitive traffic:** We finally evaluate MAPS over delay-sensitive traffic, such as VoIP. In our setting, clients C1, C2 are connected to AP1, and C4, C5 to AP2. Both APs generate saturated downlink UDP traffic to clients. DenseAP assigns a new client C3 to the highest-RSSI AP1, while MAPS connects C3 to AP2, which maximizes MU-MIMO gains. Then, C3 initiates a VoIP call to another device connected to the AP through Ethernet. Figure 6.7(d) shows the one-way network delay for VoIP traffic over a 30-second time window, for C3 at AP1 (DenseAP), and C3 at AP2 (MAPS). We observe that the average and peak delays are only 1.1 ms and 8.4 ms, when C3 connects to AP2. This is because MAPS' assignment allows for C3, C4, C5 to form a low interference MU-MIMO group. However, DenseAP assignment results in 11.4× higher average delay (12.4 ms) compared to MAPS. For 7% of the samples, the delay for DenseAP exceeds 30ms, which is above the delay requirements of VoIP applications [112]. This is because C3 mainly operates in SU-MIMO mode at AP1, due to high inter-client interference with C1 and C2. Interestingly, Figure 6.7(d) shows high delay variations for DenseAP assignment, with delay peaks up to 94ms. We observe that such peaks (at [2.7, 8.8] sec. and [23.8, 27.2] sec.) appear, when the MU-MIMO grouping algorithm tries to group C1, C2, C3 together. Such grouping creates high PER and low throughput.

### 6.6.2 Larger Scale Field Trials

We further experimentally evaluate MAPS in multiple larger scale topologies with 6 APs and 20 clients. We present the experimental floorplan in our technical report [110]. Apart from our APs, we detect 22 more BSSIDs at 5 GHz, to operate in various channels, in the same RF coverage zone. We run each experiment for 5 minutes at different times of day considering both static and mobile clients, and we report experiments from multiple runs. For each run, we compare MAPS, DenseAP and Oracle, for saturated downlink UDP and single-flow TCP traffic. Figure 6.8(a) shows the aggregated (over all APs and clients) network throughput gains of MAPS over DenseAP. Each point of the distribution reflects a different setting. We observe that MAPS performs similar or better than DenseAP in more than 90% of

the settings. For UDP, the gain is at least 149 Mbps in 50% of the settings, and it can go up to 365 Mbps (which corresponds to a 52.3% gain). Throughput gains for TCP are smaller (23.6%). This is because UDP traffic is always saturated compared to TCP. The highest gains for MAPS are observed in static client settings, when clients' channels are highly correlated. The smallest gains (or even loss) for MAPS are observed in highly dynamic environments, where MAPS' CSI profile may not capture the channel dynamics, and may assign clients to lower RSSI APs, which happen to be the lower throughput APs. In such settings, DenseAP outperforms MAPS by up to 95 Mbps (cf. Fig. 6.8(a)).

MAPS mostly performs similar to Oracle. Specifically, Figure 6.8(a) shows that MAPS throughput is the same with Oracle in 94% of the settings for UDP, and 75% of the settings for TCP. Oracle outperforms MAPS in a few scenarios of highly dynamic environments, as we discussed above.

Interestingly, MAPS can also improve the throughput fairness among clients connected to APs in the same vicinity. We illustrate our finding in Figure 6.8(b), which plots the difference of Jain Fairness Index between MAPS and DenseAP, and between Oracle and MAPS, for UDP and TCP. MAPS has always equal or larger Jain index compared to DenseAP. The difference exceeds 0.2, which is a significant gain, if we consider that an index of 1 implies perfect fairness. Since MAPS limits inter-client interferences (and hence PER), it does not negatively affects certain clients' TCP windows. This results in better TCP fairness gains (compared to UDP) over DenseAP (cf. Fig. 6.8(b)). MAPS achieves the same fairness as Oracle in the vast majority of the settings.

### 6.6.3 Trace Driven Simulations

We next conduct trace-driven simulations to evaluate MAPS in larger scale network topologies. For our simulation, we have collected wireless link performance traces (e.g., CSI, throughput, PER) from multiple settings. We have also collected per-client traffic load statistics from 82 APs of an enterprise Wi-Fi network, to simulate realistic traffic scenarios. We then combine these traces to simulate larger networks. We simulate scenarios where 20 APs and 108 (static and mobile) clients are placed in a building floor. The number of clients per AP varies from 1 to 54.

In Figure 6.8(c), we present the aggregated (over all APs and clients) network throughput gains of MAPS over DenseAP. We observe that MAPS always performs similar or better than DenseAP. Specifically, it achieves up to 1.2 Gbps (or 28.6%) and 663.8 Mbps (or 17.5%) throughput gain over UDP and TCP, respectively. Figure 6.8(c), further shows that MAPS performs the same as Oracle, for 85% and 60% of the settings, for UDP and TCP, respectively.

Interestingly, our results show that MAPS' gains over DenseAP do not necessarily drop when the

Table 6.4. Average throughput for varying number of clients.

Total clients	12	36	60	84	108
MAPS Thr. (Mbps)	$313 \pm 5$	$314 \pm 2$	$333 \pm 1$	$341 \pm 1$	$346 \pm 1$
MAPS clients AP1/AP2	6/6	19/17	31/29	40/44	52/56
DenseAP Thr. (Mbps)	$223 \pm 5$	$223 \pm 2$	$250 \pm 1$	$242 \pm 2$	$237 \pm 1$
DenseAP clients AP1/AP2	6/6	18/18	32/32	42/42	54/54
Oracle Thr. (Mbps)	$360 \pm 3$	$361 \pm 2$	$360 \pm 2$	$362 \pm 1$	$362 \pm 1$
Oracle clients AP1/AP2	6/6	19/17	31/29	40/44	52/56

number of clients connected to an AP increases. For example, Table 6.4 shows the average throughput for MAPS, DenseAP and Oracle, when the number of clients in two APs' vicinity varies from 12 to 108. We observe MAPS' gains over DenseAP range from 33% to 45%, with the maximum gain to be achieved for 108 clients. This is because, the higher number of clients connected to an AP does not necessarily increase the MU-MIMO grouping opportunities. Specifically, we observe that the number of candidate clients for grouping at each transmit opportunity (TXOP) is limited by: a) the active clients, b) the fair scheduler implemented in our AP, which will not reschedule the clients served in the previous TXOPs, c) the clients' correlated channels and channel bandwidth configurations. Particularly, we observe that the MU-MIMO groups' size for DenseAP is typically less than maximum supported size of 3 clients, or it often operates in SU-MIMO.

Finally, our simulations verify that MAPS can improve the fairness among clients, as shown in Figure 6.8(d). In conclusion, our experiments show that MAPS can significantly boost the performance for large Wi-Fi networks.

## 6.7 Related Work

There are several studies related to our work.

**AP selection:** AP selection algorithms can be classified in centralized [98,99] and distributed [113–115]. Similar to MAPS, in centralized solutions, APs exchange RSSI, traffic load, interference feedback with a controller, which decides the network-wide optimal client assignment. In distributed algorithms, it is the client which selects the best AP. However, all the above systems have been designed for legacy 802.11a/b/g/n networks and are oblivious to MU-MIMO feature. Hence, they can limit the MU-MIMO grouping opportunities, as shown by our experiments. AP selection designs proposed by AP vendors [96,

97], are also RSSI-based and have the same limitations in MU-MIMO settings.

The theoretical study in [116] jointly solves the problems of MU-MIMO AP selection and client grouping. It seeks to assign clients with uncorrelated channels to the same AP. However, such proposal has two key limitations. First, it is oblivious to clients' bandwidth configurations, and it does not consider the impact of AP load and channel utilization to throughput performance. Hence, it performs poorly in the scenarios described in Sections 6.3.3, 6.3.4. Second, our results have shown that MU-MIMO grouping and AP selection happen at different time scales (msec. and sec. scales, respectively). Thus, triggering AP selection at msec. granularity can cause excessive handoff overheads. Different from [116], MAPS decouples these two functions, and considers clients' heterogeneity and AP load, when assigning clients to APs.

**MU-MIMO grouping and scheduling:** There have been several MU-MIMO client grouping and scheduling proposals [100, 102, 117, 118]. Such designs can only achieve high MU-MIMO gains, if clients with uncorrelated channels have been assigned to an AP. Thus, they can realize their full potential, only by working in concert with designs like MAPS. Moreover, MU-MIMO grouping designs leverage explicit beamforming feedback to identify uncorrelated channels. Such approach requires excessive clients' handoffs (cf. Sec. 6.4.1), and it is not efficient for AP selection. Hence, MAPS uses implicit CSI feedback to assign clients to APs.

**Network MU-MIMO:** MAPS assigns clients with orthogonal channels to APs, to allow for MU-MIMO groups with no inter-client interference. For a given client assignment, recent designs [101, 119–121] enable APs and clients in interfering cells to coordinate cancel the inter-cell interference, using their antennas for beamforming and interference cancellation. Such solutions typically require client-side modifications and are not 802.11-compliant. On the other hand, we implement MAPS in 802.11-ac-compliant commodity APs and controllers. Note that, MAPS could also work in concert with network MU-MIMO, to further improve performance.

## 6.8 Summary

In this work, we have studied the AP selection problem in MU-MIMO Wi-Fi networks, using commodity 802.11ac testbeds. Our experimental results show that legacy AP selection designs assign clients with correlated channels and heterogeneous bandwidths to the same AP, limiting the MU-MIMO grouping opportunities. Their approach to load balancing is also MU-MIMO oblivious and can decrease the MU-MIMO gains. To this end, we propose a new Mu-mimo-Aware AP Selection (MAPS) design, which can identify the best-throughput client assignment, at low overhead. Our results show that MAPS signifi-

cantly outperforms legacy designs. We believe that MAPS can be a key building block for designing the future MU-MIMO 802.11ax and 5G networks.

# **Chapter 7**

## **Enabling Sensing Application through 60 GHz-based WLANs**

### **7.1 Introduction**

Sensing, tracking and monitoring human activities are of great interest for applications ranging from ubiquitous computing, healthcare to enabling smart homes/offices. Monitoring vital signs such as breathing rate and heart rate can provide crucial insights in human's well-being and can detect a wide range of medical problems. Compared to wearable-based approach which requires users to carry/wear a sensing device, sensing approaches based on RF (Radio Frequency) can enable device-free and contactless human tracking, activity monitoring and even vital signs monitoring. RF-based sensing has been utilized in device-free human localization and even in determining fine-grained human motion for gesture recognition [70]. In the RF-based vital sign monitoring solutions proposed in [122–125], WiFi signal reflected from the human body is used to estimate the breathing and heart rates. Although these papers have solved important challenges in designing contactless sensing applications, they have many practical limitations. Most of the existing work leverages 2.4/5 GHz bands for designing RF sensing techniques. These techniques have shown to have the limitations of rich signal multi-path, low accuracy, complex signal processing methods and necessity to maintain a controlled environment. The 2.4/5 GHz WiFi signal can also reflect from many indoor objects, and complex signal processing is necessary to extract the human reflected signal in multi-path rich indoor environment. This makes it difficult to determine the tiny motion of heartbeats from the reflected signal and hence [123–125] are primarily limited to measuring only the breathing rate. Although previous work can track human body by sweeping a very large bandwidth of 1.7 GHz in 6 GHz band [69], it is very difficult to conduct human activity analysis while tracking a person. Existing works either require a person to stay stationary and detect the person's ac-

tivities [70, 104] or purely track and localize a moving person [69]. Such systems have limited practical usage scenarios, since many applications require conducting activity analysis while a person is moving. Another design challenge remaining in existing research is the complex training and calibration process. It is required to train the system properly in order to conduct the analysis. Such training procedure has to be repeated for different locations and users, and there is a lack of an existing technique that allows activity monitoring in a deterministic and unsupervised way.

To overcome the limitations of existing RF-based sensing techniques, we seek to design a solution that can track a moving person and analyze her activities at the same time. Further more, we also investigate the use of 60 GHz millimeter-wave signal (mmWave) for ubiquitous and non-invasive vital sign monitoring. Such a technique is useful in applications like mobile interaction in smart homes/offices, gesture recognition and contactless health monitoring. To track and analyze the activities of a moving person is challenging to achieve purely based on wireless signals. Current techniques rely on signal phase/strength variation or Doppler patterns to detect human activities, however, the location changes introduce complex variations for 2.4/5 GHz signals, which makes it difficult to track and monitor at the same time. The 60 GHz mmWave frequency band provides over 7 GHz (57 - 64 GHz) of unlicensed spectrum. With the development of IEEE 802.11ad [126], the mmWave band is shown to enable high-speed (up to 7 Gbps) indoor wireless local/personal area networks. Its suitability for applications such as point-to-point video streaming has resulted in rapid commercialization with the development of WiFi+60 GHz wireless access points [127], smartphone chipsets etc. With this momentum, the 60 GHz mmWave is likely to be an omni-present technology of indoor WLANs/WPANs in homes and offices in the coming years. We demonstrate that the 60 GHz mmWave signal can provide human finding and activity monitoring as well as highly accurate and reliable vital sign monitoring. Due to high attenuation loss of 60 GHz signal, directional beamforming is employed using phased array or horn antenna to concentrate the signal in one direction. We show that mmWave signals reflected off a human body can accurately represent minute chest motion necessary to estimate human's breathing and heart rate. Due to the directional nature, the signal is not affected by any other motion outside the transmitter (Tx) and receiver (Rx) beams. Even more importantly, the directional beams reduce the signal footprint of monitoring each human, which allows higher spatial reuse where multiple human subjects can be monitored in parallel within a room.

In this work, we propose a system to locate and track a person, conduct activity analysis and monitor vital signs using 60 GHz mmWave radios. With rapid proliferation of 60 GHz-based devices, we reuse

the existing devices for the purpose of human tracking and activity monitoring. We can measure human's breathing rate and heart rate in different positions (standing, sitting, sleeping etc.) without requiring any proactive actions from the human. It is robust to different distances and incident angles of the impinging signal as humans can change their locations anywhere in the room. Although recent work [128] has shown to use 60 GHz mmWave for tracking small objects with high-precision, our objective is to track and analyze human activity with unique challenges. Comparing to conventional 2.4/5 GHz bands, 60 GHz mmWave signal exhibits higher path-loss, requiring the use of directional antennas (horn or phased array). Due to a shorter wavelength, it allows us to design small phased-array antenna with dozens of elements. Such phased-array antenna creates highly-directional beams with fast electronically steerable functionality. The beamforming results in reduced multi-path and a more tractable measurement and analysis of reflections, which in turns increases the accuracy of tracking and activity monitoring.

## 7.2 Related Work

**2.4/5 GHz based sensing and vital signs monitoring:** The authors in [124] proposed to use WiFi RSS for respiratory monitoring. However, it requires the person to hold a device or stand in the line-of-sight path between TX and RX nodes for accurate monitoring. Liu et. al. [122] leveraged fine-grained Channel State Information (CSI) of WiFi to track vital signs. The primary focus of the work to measure the vital signs when a person is sleeping and the approach is applicable to monitoring single person in a controlled environment. Also, the proposed solution can only monitor multiple humans when their vital signs are sufficiently distinct. However, in practical scenarios, individual's vital signs can vary substantially in a short time period. A similar work [125] studied a natural setting in the home with both LOS and NLOS cases to estimate a single person's respiration rate using customized WiFi hardware. The work is limited to measuring breathing rate (not heart rate) and can only monitor multiple humans breathing rate when they are sufficiently different. A wireless sensor system using 802.15.4 devices was proposed to monitor vital signs in [123] which requires deployment of many sensor nodes/links for accurate monitoring of a single human. Adib et. al. [129] proposed to use Frequency Modulated Continuous Radio (FMCR) radar for breathing and heart rates estimation. The proposed work can monitor multiple human subjects in parallel. However, it utilizes a customized dedicated hardware with a large bandwidth of 1.8 GHz (between 5-7 GHz). In contrast, our system can reuse the IEEE 802.11ad commercial networking hardware for the purpose of vital sign monitoring. Although we use customized mmWave platform (due to the unavailability of off-the-shelf hardware), our techniques simply rely on RSS and can be easily implemented on low-cost future commercial 60 GHz WLAN

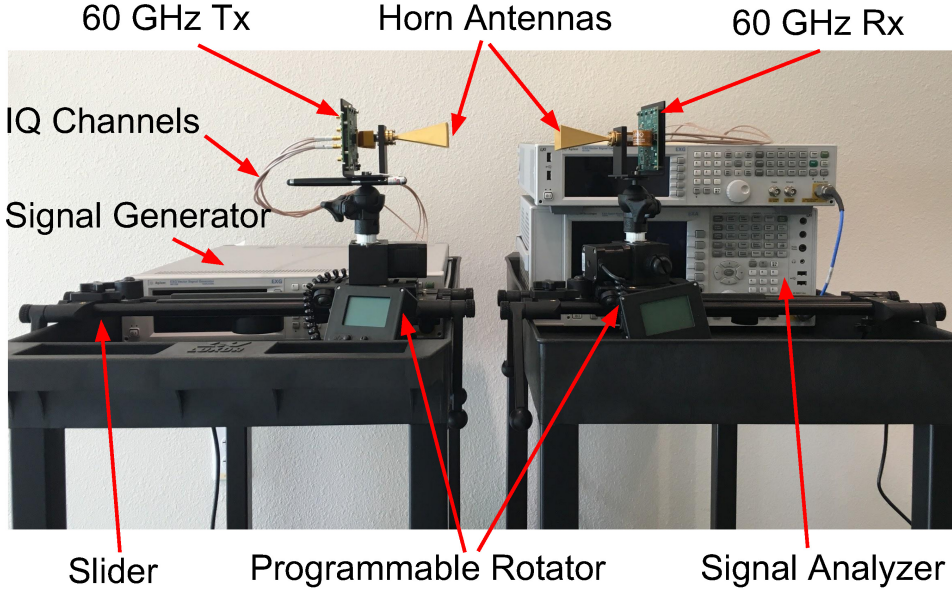


Figure 7.1. 60 GHz transmitter and receiver system setup

devices.

**mmWave sensing and networking:** Previous works have also studied vital signs detection using mmWave signal in different frequencies, such as 228 GHz [130], 94 GHz [131, 132] and 60 GHz [133, 134]. The primary focus of these papers has been to demonstrate the feasibility of vital sign monitoring with mmWave. They assume simple controlled settings with one human subject at a close distance from the transmitter and receiver. In addition, [132] and [134] focused on the mmWave sensor and hardware/chip design for vital signs detection. In our work, we focus on solving practical challenges such as finding the human's location in a room and realizing the true potential of directional beams by sensing multiple humans concurrently. Our system is designed to be operational in realistic indoor environments like offices, homes etc. as shown in our evaluation. 60GHz millimeter wave sensing has been studied in literature for other applications like target tracking and activity monitoring [135]. In a recent work, [136] proposed high-precision tracking of objects (writing with pen) using mmWave beam scanning. The reflection characteristics of different objects for mmWave signals have been studied in [137]. Authors in [138] provides a link level measurement of blockage and reflection in an indoor environment, and our reflection measurements closely match their results due to similarity of 60 GHz transmitter and receiver system. 60 GHz communication has been studied for outdoor picocells [139] with its reflection and absorption characteristics, for wireless links in data center networks [140] and for WLANs with beamforming assisted via out-of-band 2.4/5 GHz WiFi [141] or via client sensors [142].

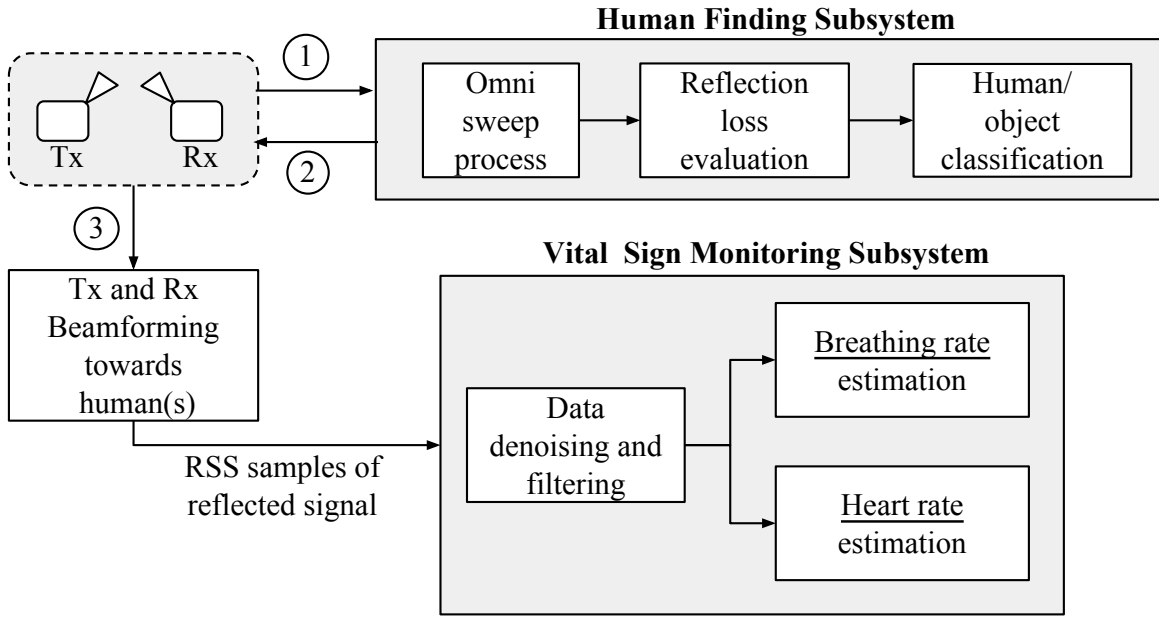


Figure 7.2. 60 GHz transmitter and receiver system setup

The reflection, blockage and beam-steering characteristics studied in these works are in agreement with our work.

### 7.3 System Design

We build a system to locate and track a person, monitor her activity while moving and further monitor her vital signs. We now describe our 60 GHz communication platform and provide an overview of our proposed system.

#### 7.3.1 60GHz Communication Platform

Our system is implemented using 60 GHz transmitter and receiver which use a mmWave development platform provided by Vubiq [143]. The mmWave platform provides a 60 GHz RF front-end and a waveguide module as shown in Fig. 7.1. On the transmitter side, we use a signal generator (Keysight EXG N5172B) that produces a 10 MHz baseband signal that is input to the Vubiq transmitter module. On the receiver side, the 60 GHz receiver module is connected to a spectrum analyzer (Keysight EXA N9010A) that allows us to analyze the received baseband signal. We calculate the Received Signal Strength (RSS) using the power spectral density distribution provided by the spectrum analyzer. The RSS values are available at an average of 62 samples per second in experiment setup, which is sufficient for monitoring

breathing and heart rates. Due to the unavailability of any reconfigurable phased array, we use a horn antenna with 3-dB beamwidth of  $12^\circ$  (estimated first null beamwidth (FNBW) of  $24^\circ$ ) and 24 dBi gain on the transmitter and receiver. A fine-resolution programmable rotator is used to form the beams in different directions and scan the surroundings for reflections.

### 7.3.2 System Overview

Various components of our proposed system are shown in a block diagram in Fig. 7.2. At a high level, our system contains two subsystems - (i) Human finding subsystem and (ii) Vital sign monitoring subsystem. The goal of the former subsystem is to find the human in a room (or an indoor space) so that Tx can direct its signal towards the human and Rx can receive the reflection. After finding the initial location of the human, we can start tracking the movement of her by rotating Tx and Rx directions. For accomplishing this efficiently, our system utilizes an omni-sweep procedure that profiles the indoor environment in terms of its reflections and tracks any changes to it. When new reflections are detected, the reflection loss is evaluated to classify if they are from movable objects (e.g., chairs, laptops etc.) or a human. Our system leverages the diversity in material permittivity to accurately identify human reflections. Once the Tx and Rx beamforming angles towards the human are determined, the second subsystem performs the vital sign monitoring. Here, the signal reflected by the human body are analyzed through RSS samples to estimate the vital signs. The RSS samples first undergo data denoising procedure where a sliding window-based moving average filter is applied to remove the high-frequency noise. Apart from that, we also apply a bandpass frequency filter with cutoff of 0.1-20 Hz in order to remove the impact of slow moving DC component as well as moderate to high frequency human movements [144] (e.g., shaking of body parts). The breathing rate and heart rate modules further apply their custom filters and peak detection algorithms for estimation.

## 7.4 60 GHz-based Human Finding and Activity Analysis

A major challenge in the design of our system is that it is required to determine where the human is before it can start monitoring her activities and vital signs. In home, office or a similar indoor place where human can freely move from one place to another, our system should be able to *find* the human and point the transmitted signal towards her body. In this section, we introduce a *human finding* procedure that can be used to determine precise Tx and Rx angle to transmit the signal to human body and receive the reflection respectively. The challenge of human finding is further complicated by the fact that 60 GHz signal is reflected by many different objects in an indoor environment. Such objects include walls, metal objects

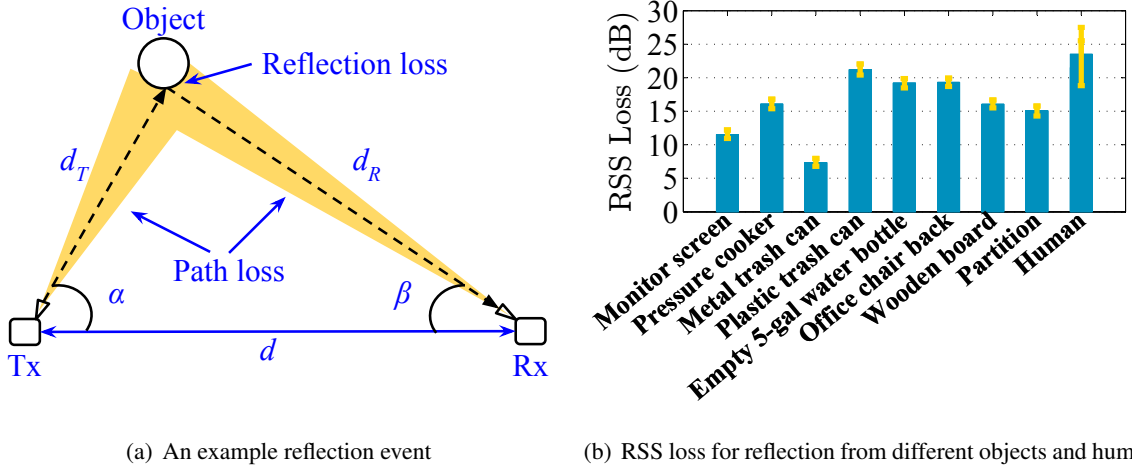


Figure 7.3. Reflection loss for different types of objects

such as cupboards, monitors, microwave, trash-cans etc. In the presence of many possible reflections, it is difficult for the Tx and Rx to know which reflection is indeed coming from a human.

our system utilizes a novel approach to distinguish human from objects based on reflective loss as it is known to be different for different objects [137]. The permittivity dictates the amount of signal that penetrates the object and reflects from it. Apart from penetration and reflection, the signal is also absorbed by the objects and scattered from its surface. However, absorption and scattering effects are difficult to measure in our system. Instead, we leverage the difference in reflection loss due to different permittivity to distinguish the objects from human.

In order to measure the reflection loss, it is first necessary to remove the effect of distance dependent path loss. Fig. 7.3(a) shows an example reflection event from an object. If the transmission power is  $P_T$ , transmit antenna gain is  $G_T$ , received power is  $P_R$ , and receiver antenna gain is  $G_R$ , the total loss  $L = (P_T + G_T + G_R) - P_R$  is as follows

$$L = L_P(d_T) + L_P(d_R) + L_R(\epsilon_o) \quad (7.1)$$

where  $L_R(\epsilon_o)$  is reflection loss from object with permittivity of  $\epsilon_o$ ,  $d_T$  and  $d_R$  are the distances of the object from the Tx and Rx respectively. The reflection loss can be calculated as shown in Section 7.5.2. The path loss  $L_P(D)$  at distance  $d$  can be calculated using Friis model of free-space attenuation as

$$L_P(D) = 20 \log_{10}\left(\frac{4\pi D}{\lambda}\right) \quad (7.2)$$

where  $\lambda$  is the signal wavelength. The Tx and Rx have the knowledge of  $P_T$  and  $P_R$ , and the distance between them ( $d$ ). As shown in Fig. 7.3(a),  $d_T$  and  $d_R$  can be calculated using the angle of transmission

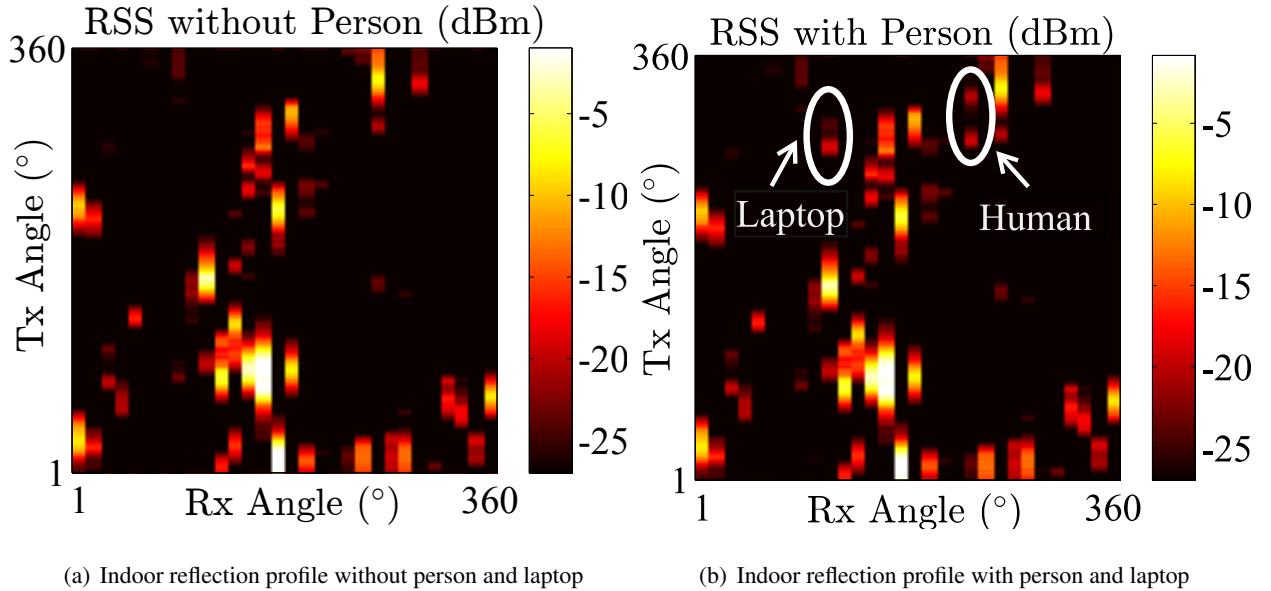


Figure 7.4. Reflection profile of a room

( $\alpha$ ) and reception ( $\beta$ ) to derive  $L_P(d_T)$  and  $L_P(d_R)$ . Using Eq. 7.1 and 7.2, they can calculate the reflection loss  $L_R(\epsilon_o)$ . The reflection loss can then be used to distinguish if the reflection is coming from a human or an object.

To evaluate the feasibility of object/human classification based on reflection loss, we test a variety of reflective objects and place them at one fixed location (fixed path loss) one by one. The observed RSS values for the objects and human are shown in Fig. 7.3(b). We can observe that different objects and human, depending on their material permittivity, reflects different amount of signal. Hence, we use regression on the reflection loss to identify if it is from an object or a human. In our experiments, we observe that the human/object classification can be done using even a single RSS sample based on the reflection loss, making the human finding procedure very efficient. With the use of more RSS samples, the confidence of classification can be further improved since the RSS for human reflected signal varies more due to heartbeat and breathing motion compared to the objects.

Before the classification can be applied, our system is required to find the reflection profile of the indoor environment. The reflection profile can be found by a brute-force omni-directional sweeping of Tx and Rx beams. The procedure is formally described in Algorithm 1. For each Rx angle (in steps from  $0^{\circ}$  to  $360^{\circ}$ ), the Tx scans the entire  $360^{\circ}$  to determine all reflections. Note that although the omni-sweep procedure is brute-force, it can be completed in a short time with digital beamforming where beam switching can be performed at much smaller time scales. Also, the procedure is only required to be

---

**Algorithm 2 Human Finding Procedure**

---

**Require:** Tx power ( $P_T$ ), RSS variation tolerance threshold ( $\kappa$ ), Beam sweep step size ( $s^\circ$ ), number of previous RSS samples ( $k$ ), Human/object classifier ( $\Psi(\cdot)$ ), distance between Tx and Rx ( $d$ )

**Ensure:** Tx and Rx angles towards human

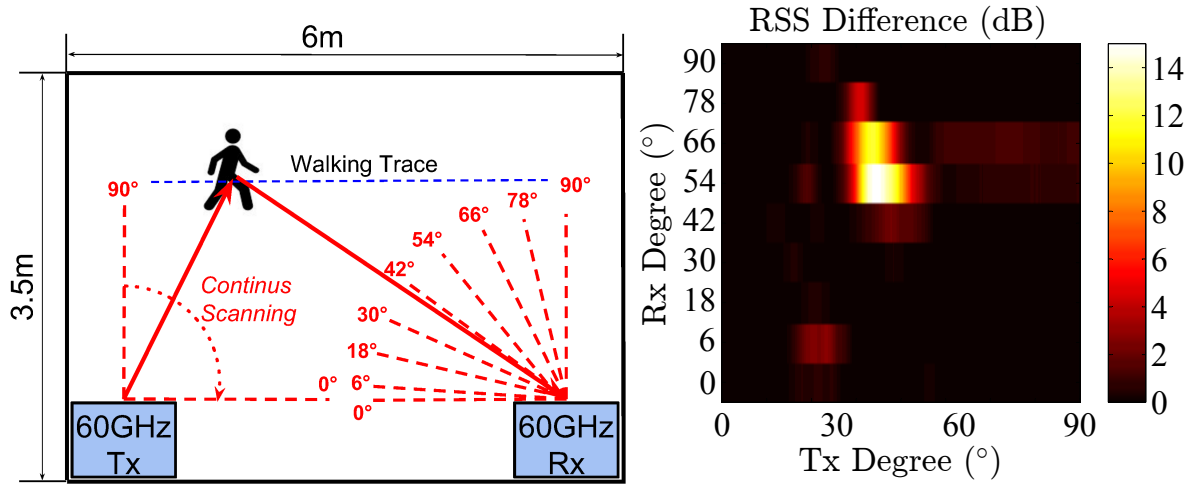
**Procedure:**

```
1: for  $\alpha : 0^\circ \rightarrow 360^\circ$  do {{#Omni-sweep procedure}}  
2:   for  $\beta : 0^\circ \rightarrow 360^\circ$  do  
3:      $R_{(\alpha,\beta)}^t = RSS(\alpha, \beta)$   
4:      $\Delta_{(\alpha,\beta)}^t = |R_{(\alpha,\beta)}^{t-1} - R_{(\alpha,\beta)}^t|$   
5:     if  $\Delta_{(\alpha,\beta)}^t > \kappa$  then {{#Change in reflection}}  
6:       Calculate  $d_T$  and  $d_R$  using  $\alpha, \beta$  and  $d$   
7:       for  $i : t - k \rightarrow t$  do {{#Analyze last k samples}}  
8:          $L_{(\alpha,\beta)}^i = P_T - R_{(\alpha,\beta)}^i - L_P(d_T) - L_P(d_R)$   
9:          $\Gamma_{(\alpha,\beta)} = \Gamma_{(\alpha,\beta)} \cup L_{(\alpha,\beta)}^i$   
10:      end for  
11:      if  $\Psi(\Gamma_{(\alpha,\beta)}) = \text{"Human"}$  then {{#Human-object}}  
12:        return  $\alpha, \beta$  {{#classification}}  
13:      end if  
14:    end if  
15:     $\beta = \beta + s^\circ$   
16:  end for  
17:   $\alpha = \alpha + s^\circ$   
18: end for
```

---

performed when human's vital signs can no longer be monitored and human finding procedure has to be initiated. Also, both Tx and Rx can use discrete steps for angle increment for generating non-overlapped beams (similar to sectors in 802.11ad) to reduce the time complexity.

To demonstrate the omni-sweep procedure, we use our testbed to build the reflection profile of a room. Due to our horn antenna 3-dB beamwidth of  $12^\circ$ , the Rx scans all directions in increments of  $12^\circ$ . For each Rx angle, Tx scans the entire  $360^\circ$  with continuous rotation. The reflection profile in the absence of any human is shown in Fig. 7.4(a). As we can see, a typical room has many different reflections from wall and other objects. In our system, the profile can be built in the absence of a human



(a) The layout of the experiment for human finding and walking    (b) Heatmap profile for initial human finding process analysis

Figure 7.5. The experiment layout and human finding analysis

and then only the changes in reflections need to be monitored to find human. Note that a change in reflection can occur due to the presence of a human (increase if new reflection and possible decrease if existing reflection blocked) as well as movement of any existing object (e.g., moving a chair or laptop). Fig. 7.4(b) shows the reflection profile with a human and a laptop (with metal enclosure) in the room. Both laptop and human reflect the signal, which can be tagged as the change in the reflections. As in Algorithm 1, each change in reflection is inspected using the reflection-loss based classifier to identify if the change is due to a human or an object. As we observe from Fig. 7.4(b), in some cases, the existing reflections exhibit minor difference in RSS at different times. This can be due to the changes in object temperature. In order to ignore such minor variations, we utilize a RSS variation tolerance threshold ( $\kappa$ ). Whenever a change in RSS is within the threshold, our system does not consider the reflection for object-human classification. Lastly, for the changed reflections, the Tx and Rx angles are used to determine the path loss, and calculate the reflection loss as Eq. 7.1. This reflection loss is input to the object-human classifier, and if the reflection loss is classified as “human”, the Tx and Rx angles of the reflections are used to start monitoring the human for her vital signs.

#### 7.4.1 Activity Analysis

Before we start activity monitoring, we need to first determine the initial location of the person. Considering a typical indoor space, Fig. 7.5(a) shows our experiment layout. Instead of conducting 360° scanning, we put 60 GHz Tx and Rx at the corners of the room and perform 90° scanning of the entire

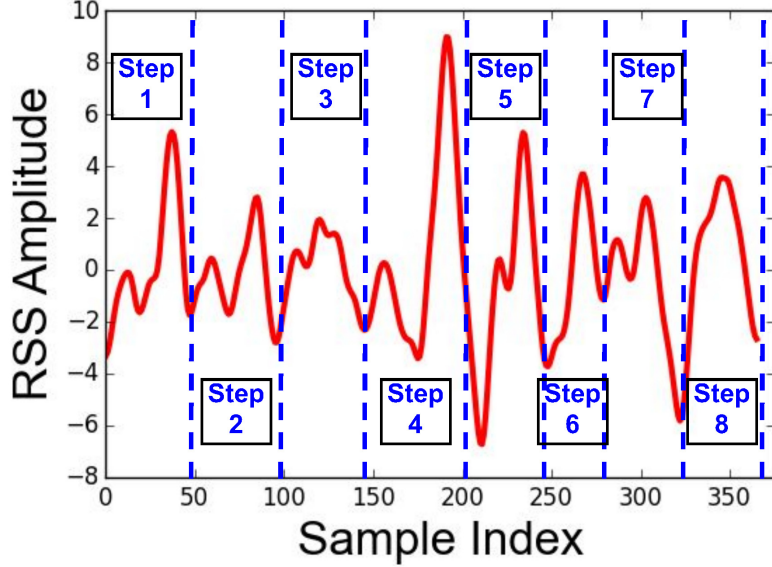


Figure 7.6. RSS profile for walking activity analysis

room. The Tx performs a continuous scanning with a fine-grained resolution of  $0.03^\circ$  from  $90^\circ$  to  $0^\circ$ . To reduce the finding time, the Rx scans in a discrete manner with an angular resolution of  $12^\circ$ . Note that the reason of choosing  $12^\circ$  is because the 3-dB beamwidth of the horn antenna is  $12^\circ$ . For each angle of the Rx, the Tx performs  $12^\circ$  continuous scanning and record the RSS values on the Rx side. Assuming that the distance between Tx and Rx is known, the location of the person can be calculated by determining Tx angle and Rx angle. We first do a brute-force  $12^\circ$  scanning for both Tx and Rx, constructing the RSS profile when there is no person presented in the room. Next, when there is a person in the room, we repeat the same procedure again and construct the RSS profile. We calculate the RSS difference between the two profiles. Fig. 7.5(b) shows the heatmap of the absolute RSS difference values. Due to the reflection changes introduced by the person, we observe that the points with highest density represent the initial location of the person. In our ongoing work, we are extending the human finding procedure to tracking, where the Tx and Rx beams follow the user by continuously monitoring the RSS change around the initial location of the user.

Due to the highly-directional beams of 60 GHz mmWave, we need to rotate the Tx and Rx in order to maintain the signal always being reflected from the person we are trying to track. Assuming we can track the moving person accurately, the next step is to conduct activity analysis. Here we use walking activity as an example to show our initial results on activity monitoring. Fig. 7.6 shows the RSS profile when a person is walking along the walking trace shown in Fig. 7.5(a). We collected the raw RSS data

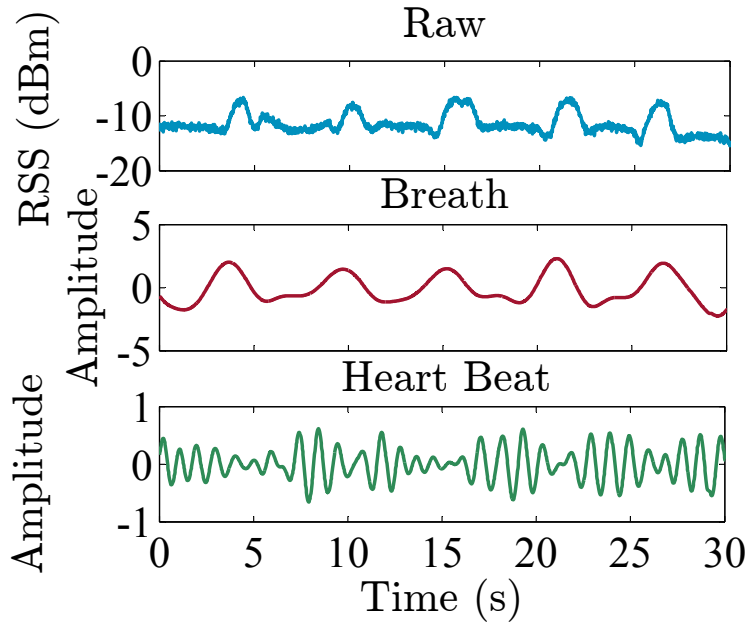


Figure 7.7. Raw RSS of the reflected signal and extracted breathing and heart beats

from the Rx and then process it with a band-pass filter (0.8 Hz to 4 Hz) to remove the DC component as well as high frequency noise. We can observe repeated RSS variation patterns indicating individual step as labeled in Fig. 7.6. Since each location has different incident angle of reflecting the signal, the actual reflected RSS value will be different. We can see that step 4 has the best incident angle for the reflection, so we observe more signal being reflected (higher RSS amplitude). By analyzing the RSS profile, we can track the person and count the steps of walking activity.

## 7.5 60GHz-based Vital Signs Monitoring

This section describes the main modules of vital sign monitoring subsystem.

### 7.5.1 Breathing and Heart Rates

In order to estimate the breathing rate, we transform the filtered RSS data to frequency domain. We observe that the RSS signal is very sensitive to periodic movement of human breathing, which results in a peak (dominant frequency) in the frequency domain. The frequency of the peak represents the breathing rate at a coarse-grain. However, simply selecting the highest peak is not always accurate due to variations introduced by noise and motion. To achieve a better accuracy, we select the highest magnitude peak as well as the frequency of the two adjacent bins, and create a custom narrow band-pass filter. We apply the filter on the RSS data and perform an Inverse FFT (IFFT) to yield the filtered time-series data. We then use a simple peak detection algorithm for precisely counting the breathing rate in Bpm.

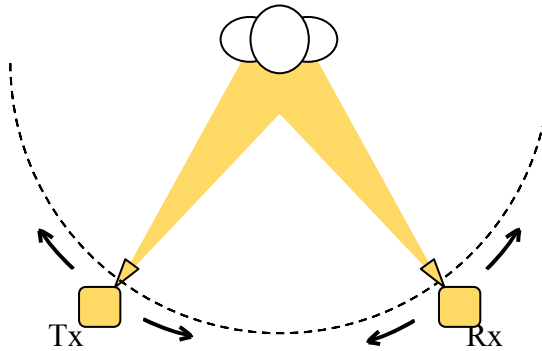


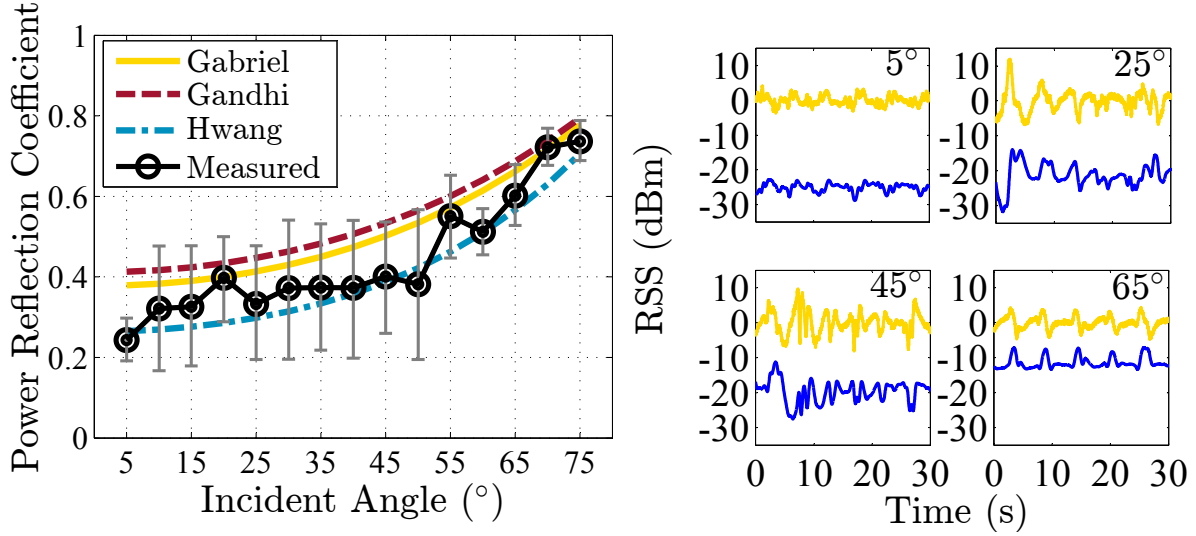
Figure 7.8. Experiment setup of evaluating different incident angles

The normal heart rate of an adult is known to be in the range of 60-100 [145] bpm. However, during high-intensity activities like exercising, the heart rate can exceed 170 bpm [145]. For such activities and to detect any other abnormal conditions, we select the heart rate range to be 50-220 bpm. Similar to the breathing rate estimation, we apply an FFT on the RSS time-series data and determine the dominant frequency. In this case, we select the highest magnitude peak along with four adjacent bins of frequency to create the custom band-pass filter because the heart beat motion is smaller compared to the breathing motion and can exhibit larger variations. We apply the filter, perform IFFT and use the peak detection for estimating heart rate.

Fig. 7.7 shows an example of raw RSS samples along with filtered breathing and heart beat samples. We offset the RSS values by the transmission power to present the RSS and RSS loss on the same scale. After applying the customized filters, we apply peak detection algorithm for accurate counting. We note that our system estimates the vital signs in real-time using a sliding window of 30 seconds offset by approximately 100ms (every 6 RSS samples in our testbed).

### 7.5.2 Impact of Incident Angle

Because a human can be anywhere within the Tx and Rx vicinity while being monitored for her vital signs, the transmitted signal can impinge on the human body at any angle (referred as incident angle). We now investigate the impact of incident angle on the reflected signal, and the robustness of breathing rate and heart rate estimation. The amount of energy reflected from an object can be quantified using *power reflection coefficient* which can be derived from reflection coefficient. The reflection coefficient is the ratio of the complex amplitude of the reflected electromagnetic wave to that of the incident wave. The coefficient depends on factors such as the permittivity (a complex value) of the object material and



(a) Impact of incident angle on reflected power (theoretical and measured)  
(b) Raw and filtered RSS for  $5^\circ$ ,  $25^\circ$ ,  $45^\circ$  and  $65^\circ$  incident angles

Figure 7.9. Impact of incident angle

the signal incident angle. The reflection coefficient ( $r$ ) can be calculated [146] as

$$r = \frac{1 - e^{-j2\omega}}{1 - r_i^2 e^{-j2\omega}} r_i, \quad \text{for } i \in \{\perp, \parallel\} \quad (7.3)$$

where  $\omega = \frac{2\pi l}{\lambda} \sqrt{\epsilon_2/\epsilon_1 - \sin^2 \gamma}$ ,  $l$  denotes the thickness of the reflecting source;  $\lambda$  denotes the signal wavelength;  $\gamma$  is the incident angle;  $\epsilon_1$  and  $\epsilon_2$  are the permittivities of the first medium and the second medium, respectively. In a simplified single layer model, the first medium can be assumed as air which has the permittivity of 1.  $r_\perp$  and  $r_\parallel$  are the Fresnel's reflection coefficients when the electric field is perpendicular and parallel to the incidence plane, respectively. The coefficients can be calculated as

$$r_\perp = \frac{\cos \gamma - \sqrt{\epsilon_2/\epsilon_1 - \sin^2 \gamma}}{\cos \gamma + \sqrt{\epsilon_2/\epsilon_1 - \sin^2 \gamma}}. \quad (7.4)$$

$$r_\parallel = \frac{\epsilon_2 \cos \gamma - \sqrt{\epsilon_2 \epsilon_1 - \epsilon_1^2 \sin^2 \gamma}}{\epsilon_2 \cos \gamma + \sqrt{\epsilon_2 \epsilon_1 - \epsilon_1^2 \sin^2 \gamma}}. \quad (7.5)$$

The reflection coefficient ( $r$ ) can be used to estimate the power loss due to reflection (or power reflection coefficient) as  $L_R = \frac{P_O}{P_I} = |r|^2$  where  $P_O$  and  $P_I$  are the values of reflected (after reflection) and incident (before reflection) power respectively.

We empirically evaluate the impact of incident angle on the reflection power loss as shown in Fig. 7.8. In the experiments, the Tx and Rx move symmetrically on a circle of 3 meter radius. The human sits

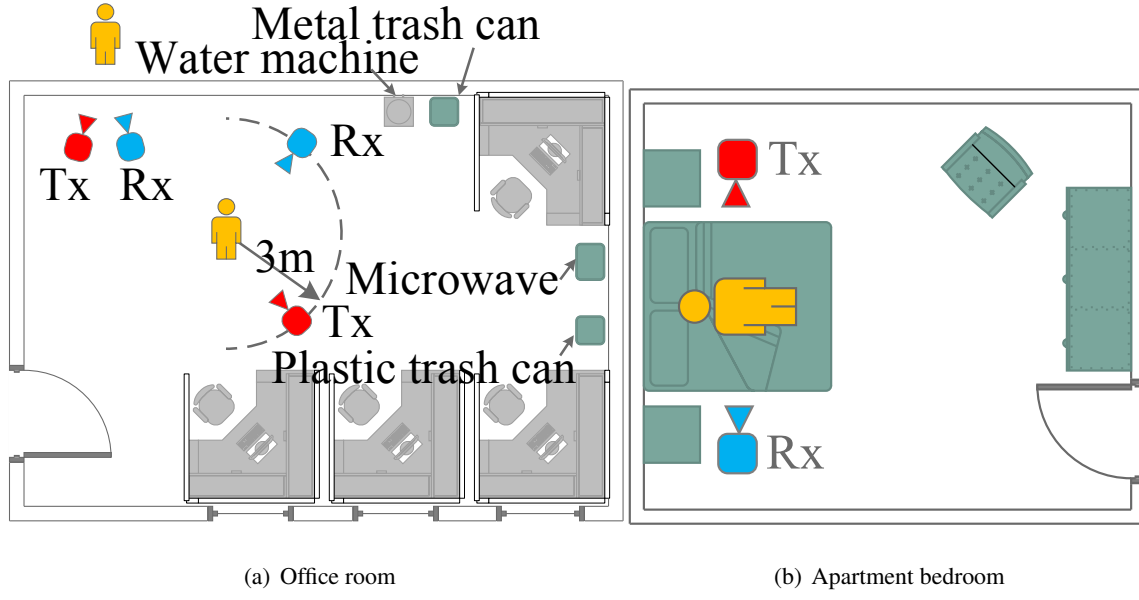


Figure 7.10. Experiment setup in office and home

at the center of the circle, and both Tx and Rx point their horn antennas to the human. Since the  $P_I$  is unknown, we first use an aluminum plate at each incident angle in the place of the human and measure the received power. As an aluminum plate is regarded as a perfect reflector (reflection loss nearly 0 dB), and we use its received power as a reference for human measurements. Fig. 7.9(a) shows the reflection loss ( $L_R$ ) for incident angles from  $5^\circ$  to  $75^\circ$ . It also compares the theoretical value of reflection loss calculated using Eq. 7.3 and 7.4 (perpendicular). For the calculations, three different values of human body/skin permittivity are considered based on previous work from Gabriel et al. [147], Gandhi et al. [148] and Hwang et al. [149]. These values are  $7.89 - j10.90$ ,  $8.89 - j13.15$  and  $8.05 - j4.13$  at 60 GHz, respectively [150]. We observe that our measurements are in agreement with permittivity models of [147] and [149]. Higher variations observed in the measurements are due to human's breathing motion. Examples of the reflected RSS (raw and filtered) at different incident angles are shown in Fig. 7.9(b). It can be seen that as the incident angle increases, the RSS samples becomes less and less noisy mostly due to decrease in the reflection loss. The main observation in Fig. 7.9(b) is that the reflected RSS is representative of the breathing motion at all incident angles. Hence, our system is robust to human changing location relative to Tx and Rx. Also, if our system is used to monitor humans when they do not change location (e.g., sleeping in bedroom or hospital bed), it is advisable to deploy the Tx and the Rx at larger incident angles to increase the estimation accuracy.

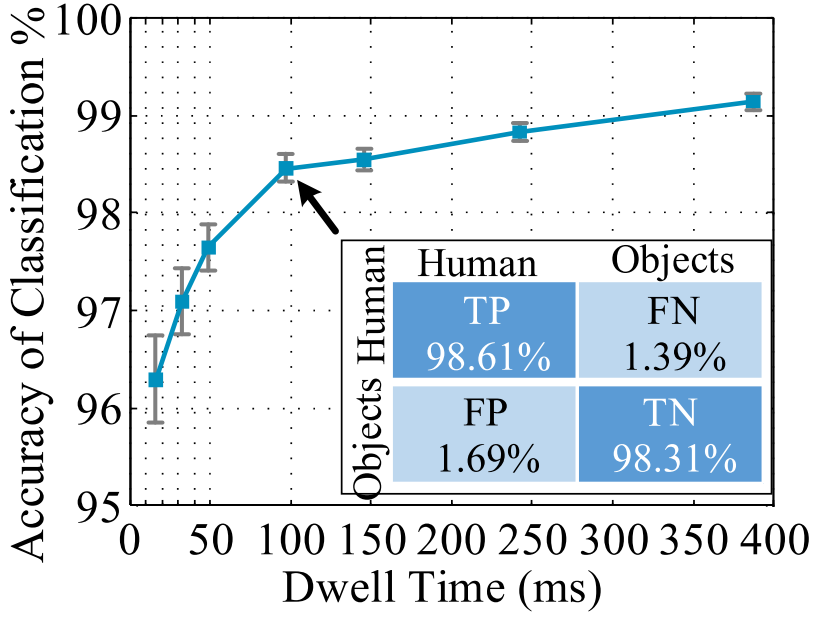


Figure 7.11. Accuracy of object/human classification with varying dwell time (number of RSS samples)

## 7.6 Evaluation

We perform an extensive evaluation of our system in two different indoor scenarios as shown in Fig. 7.10. First room is a laboratory room (size:  $6m \times 9m$ ) in a university building with objects such as cubicle partitions, white boards, metal cupboard, computers etc. The second room is an apartment bedroom of size  $4.5m \times 6m$  with a bed in the center and other furniture on the sides. Fig. 7.10 shows the positions of Tx and Rx. We enroll 7 participants over a period of two weeks to monitor their vital signs. Out of the 7 subjects, 6 subjects had a Body Mass Index (BMI) of  $19\text{-}25 \text{ kg/m}^2$  and one subject (Subject #6) had the BMI of  $29 \text{ kg/m}^2$ . The BMI is correlated with breathing rate and other cardiovascular parameters [151]. The ground truth is established using a finger pulse oximeter [152] (for heart rate) and Neulog chest-strap respiration monitor [153].

### 7.6.1 Reflection Loss based Human Finding

The human finding procedure described in Algorithm 1 is evaluated in the laboratory room scenario. We create 20 different scenarios where 8 objects (laptop, metal utensil, plastic trash can, metal trash can, empty 5 gal. water bottle, chair, wooden board, partition board) and a human subject are randomly re-located inside the room. Similarly, Tx and Rx are also moved to randomly chosen points in the room. The movement of objects, human and Tx-Rx ensures that a wide variety of distances and incident angles are evaluated for moving as well as non-moving objects (walls, tables etc.). For each of 20 the scenar-

ios, we find the reflection profile to determine the reflection from moved objects and the human. The reflection loss based classification is then applied to the RSS values of changed reflections as described in Section 7.4. The results of the classification are presented in Fig. 7.11. We vary the time interval for which RSS samples are collected (dwell time) at each angle before performing the classification. It can be observed that as the dwell time increases, the accuracy of human-object classification increases. A reflection is from a human or an object can be determined with average accuracy of 96.2% only with one RSS sample (available after 16 ms). With 100 ms of dwell time, the accuracy increases to 98.4% with false positive rate of < 2%. This means that the human finding procedure is highly robust to environment changes and can accurately determine the Tx and Rx angles for monitoring.

## 7.6.2 Accuracy of Vital Sign Monitoring

### 7.6.2.1 Breathing and Heart Rate Estimation Accuracy

For evaluating the breathing and heart rates of participants, we use three different incident angles in the university room. Figs. 7.12(a) and 7.12(b) show the mean estimation error with (95% confidence intervals) for breathing rate (Bpm) and heart rate (bpm) for the 7 participants at 3 different incident angles ( $70^\circ$ ,  $50^\circ$ ,  $30^\circ$ ). The accuracy is calculated for 3 experiment runs of 10 minutes for each of the participants. For the incident angle of  $70^\circ$ , the mean estimation error in breathing rate and heart rate estimation is less than 0.5 Bpm and 2.5 bpm respectively for all 7 participants. This shows that 60 GHz vital sign monitoring can provide highly reliable estimate of breathing and heart rates. The estimation error increases with the decrease in the incident angles, which proves the relationship between the reflection loss and incident angle discussed in Section 7.5.2. At higher incident angles, the reflection loss decreases as well as the reflected RSS is observed to be less noisy. Both these factors increase the vital sign estimation accuracy. We observe that the breathing and heart rate estimation errors are slightly higher for Subject #6 which is likely due to higher BMI. Since these experiments were performed with the participants either standing or sitting, the estimation error is likely to be even lower when they are sleeping on bed as breathing rate is substantially more stable when human is sleeping.

### 7.6.2.2 Robustness to Distance and Posture

We also evaluate the impact of human's distance from Tx and Rx on the observed RSS and the accuracy of vital sign monitoring. The estimation accuracy is defined as the difference between the ground truth and the estimated vital sign divided by the ground truth. We fix the incident angle to be  $45^\circ$  and the location of the human subject, while moving the Tx and Rx away from the human in steps of 1 meter. We evaluate the RSS and breathing rate estimation accuracy while varying the Tx-human (and Rx-human)

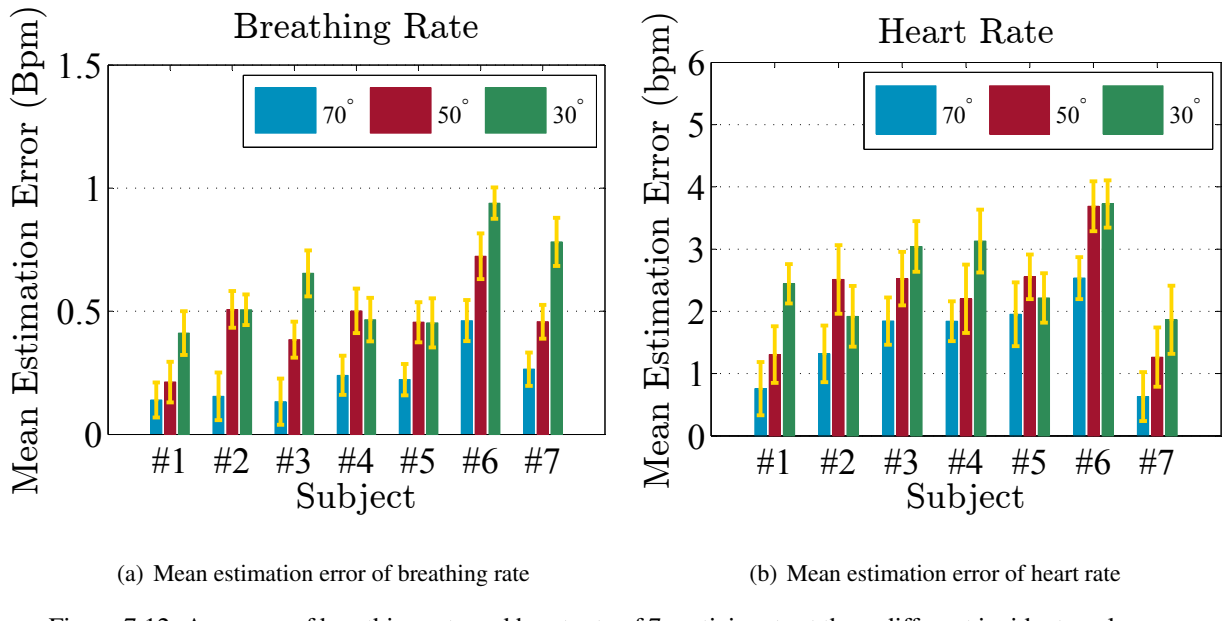
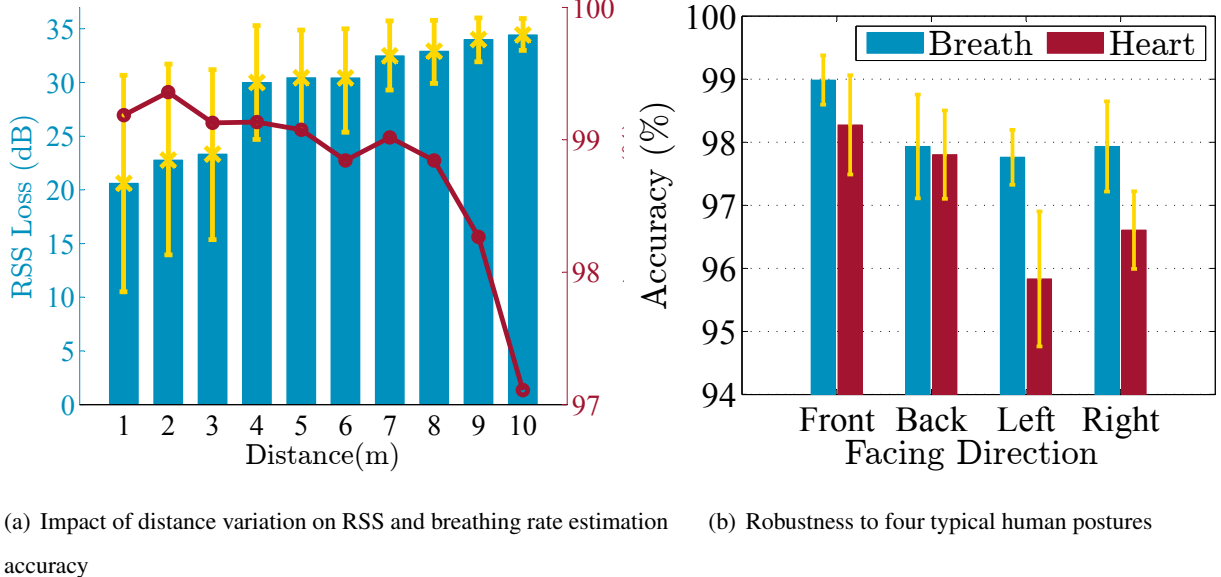


Figure 7.12. Accuracy of breathing rate and heart rate of 7 participants at three different incident angles



(a) Impact of distance variation on RSS and breathing rate estimation accuracy      (b) Robustness to four typical human postures

distance from 1 meter to 10 meters. Fig. 7.13(a) shows RSS loss and breathing rate estimation accuracy for varying distance. Note that distance in Fig. 7.13(a) indicates the Tx to human (or human to Rx) distance, so the total signal propagation distance (Tx to human and human to Rx) is actually double. As expected, the RSS loss increases and estimation accuracy decreases with increase in distance. The confidence intervals on RSS loss indicates that sufficient variations in the signal is observed even at a

larger distances (upto Tx-human distance of 8 meters). Recall that this signal variation is useful in finding the human and distinguishing its reflection from other objects (Section 7.4). For distances lower than 8 meters, the mean breathing rate estimation error is less than 0.42 Bpm (mean accuracy is 98.8%), and beyond 8 meters the mean estimation error drops close to 1.07 Bpm, (mean accuracy is 97%). This shows vital sign estimation of our system is robust to distances common in rooms of typical indoor spaces like offices and homes.

Since the signal can impinge anywhere on the human body depending on the human's orientation relative to the Tx and Rx, we evaluate the impact of human's facing direction (or posture) on breathing and heart rate estimation accuracy. In this experiment, 5 participants are asked to sleep on the bed in the apartment bedroom (Fig. 7.10(b)) for 3 minutes (repeated 10 times) in four different postures - sleeping on back (Front), sleeping on stomach (Back), facing left (Left) or facing right (Right). The results of breathing rate and heart rate estimation accuracy are shown in Fig. 7.13(b). We observe that highest breathing rate estimation accuracy is observed for the front posture in which the signal directly strikes and reflects from human's chest area which exhibits the maximum breathing motion. However, for the other three postures also breathing rate estimation accuracy remains close to 98%. In terms of heart rate estimation, front posture also provides highest accuracy, followed by the back posture. In both front and back postures, reflected signal better captures the heart beat motion compared to left and right postures. When the human is facing right, her heart is towards the incoming signal from the Tx compared to when she is facing left, resulting in a better heart rate estimation accuracy for the right posture. In all cases, we observe that our system achieves high vital sign monitoring accuracy even when human is in different postures.

#### 7.6.2.3 Behind the Wall Estimation

The breathing rate estimation accuracy is evaluated for behind-the-wall case shown in Fig. 7.10(a). Here, a human stands on the other side of the wall from the Tx-Rx pair. Because penetration loss and reflection loss change depending on the incident angle, two incident angles ( $10^\circ$ ,  $20^\circ$ ) are evaluated. The mean estimation error of breathing rate is observed to be 0.58 Bpm and 0.93 Bpm for  $10^\circ$  and  $20^\circ$ , respectively. In contrast to line-of-sight cases, increase in incident angle increases the estimation error in behind-the-wall cases. This is because at higher incident angles, more signal is reflected and lesser signal penetrates through the wall to strike human body. The RSS reflected also undergoes the same phenomenon and the received RSS carries a weaker signature of breathing motion. It is worth noting that if the application does not require behind-the-wall monitoring, the transmission power can be reduced or larger incident

angles can be used (more reflection, less penetration) to contain the 60 GHz signal within the room.

## 7.7 Summary

In this work, we enabled human sensing using 60 GHz networks and presented a vital sign monitoring system utilizing mmWave signal reflected from human body. Our system is shown to be accurate in monitoring breathing and heart rates. We also proposed a novel human finding procedure that can locate human body before vital sign monitoring using reflection loss characteristics. We evaluated our system using state-of-the-art 60 GHz testbed and 7 participants, and showed that it can provide accurate and robust (to incident angles and distances) vital sign monitoring.

# Chapter 8

## Conclusions

With the increasing popularity of WLANs, we have witnessed that WLANs brought connectivity to every aspect of our life. However, based on existing infrastructure, traditional WLANs lack of variability in providing different functions or services beyond the Internet access. We have presented various ways to enrich the functionality of WLANs mainly using advanced sensing techniques and smart networking applications. We bring the context and human activity sensing capability to traditional WLANs infrastructure.

We start from characterizing the latest WLANs to motivate our problem. We presented a performance characterization of 802.11ac standard. We identified what is the impact of utilising larger channel width on energy efficiency and interference. We showed that 80-MHz channel width yields substantial throughput improvement, but the improvements come at the cost of higher power consumption. We also showed that increasing the number of spatial streams is more energy efficient compared with increasing the channel width in achieving the same percentage increase in throughput. Also, our interference characterization showed that unplanned selection of primary channels and channel widths can severely degrade the throughput of links operating at larger channel widths. Through this work, we find that current throughput performance can meet most traditional usage requirements for WLANs applications, however diversifying and enriching WLANs services are needed.

We then studied the advanced sensing methodology using an example of estimating energy expenditure using wearable devices. We proposed usage of the accelerometer and barometer body sensors of smartphones for accurate energy expenditure estimation in ambulatory settings. We collected accelerometer and barometer sensors readings at 2Hz only and then used these values to obtain FVs and fit an ANN which can yield up to 89% correlation and RMSE of 1.07 with minimal computational overhead. Inspired by this work, we then enabled human activity sensing through 2.4/5 GHz-based WLANs

by presenting fine-grained device motion recognition and shopper’s behavior analysis through WiFi signals. We showed that CSI data could be used to determine client’s fine-grained motion at the AP. We also presented a novel physical analytic approach which leverages CSI from WiFi network to infer shopper’s behavior. Our proposed system is a non-intrusive, device-free, low-cost and privacy-preserving way to perform physical analytic. It can achieve around 90% accuracy to classify different states of the shopper during a typical in-store visit.

After enabling 2.4/5 GHz-based sensing, we enriched the functionality of WLANs with WiWho, which is a framework for identifying a person using the gait information detected via 2.4/5 GHz WiFi signal. WiWho enables a device-free, effortless, low-cost and pervasive solution for person identification in smart homes and offices. We showed the feasibility of gait identification through CSI and discussed the necessary characteristics of CSI based gait that can identify a person. WiWho achieves an identification accuracy of 92% to 80% for a group size of 2 to 6 respectively, and only 2-3 meters walking length is necessary. The limitations and potential of WiFi-based person identification system are also discussed.

To enrich WLANs with smart networking application, we studied the AP selection problem in MU-MIMO Wi-Fi networks, using commodity 802.11ac testbeds. Our experimental results show that legacy AP selection designs assign clients with correlated channels and heterogeneous bandwidths to the same AP, limiting the MU-MIMO grouping opportunities. Their approach to load balancing is also MU-MIMO oblivious and can decrease the MU-MIMO gains. To this end, we propose a new MU-MIMO-MIMO-Aware AP Selection (MAPS) design, which can identify the best-throughput client assignment, at low overhead. Our results show that MAPS significantly outperforms legacy designs. We believe that MAPS can be a key building block for designing the future MU-MIMO 802.11ax and 5G networks.

In the end, we extended existing 2.4/5 GHz-based sensing applications to 60 GHz-based WLANs. We presented a human activity and vital sign monitoring system utilizing mmWave signal reflected from human body. Our system is shown to be accurate in monitoring breathing and heart rates. We also proposed a novel human finding procedure that can locate human body before using reflection loss characteristics. We evaluated our system using state-of-the-art 60 GHz testbed and 7 participants and showed that it could provide accurate and robust (to incident angles and distances) vital sign monitoring.

## BIBLIOGRAPHY

- [1] “IEEE 802.11ac - Enhancements for Very High Throughput for operation in bands below 6GHz,” *IEEE P802.11ac/D5.0*, 2013.
- [2] M. Park, “Ieee 802.11 ac: Dynamic bandwidth channel access,” in *Proceedings of IEEE ICC*, 2011, pp. 1–5.
- [3] “802.11ac: The Fifth Generation of Wi-Fi,” [http://www.cisco.com/en/US/prod/collateral/wireless/ps5678/ps11983/white\\_paper\\_c11-713103.html](http://www.cisco.com/en/US/prod/collateral/wireless/ps5678/ps11983/white_paper_c11-713103.html), August 2012.
- [4] “802.11ac Technology Introduction,” [http://www.rohde-schwarz.com/en/solutions/wireless-communications/wlan-wifi/in-focus/technology-introduction\\_106713.html](http://www.rohde-schwarz.com/en/solutions/wireless-communications/wlan-wifi/in-focus/technology-introduction_106713.html), March 2012.
- [5] “Samsung Galaxy S4,” <http://www.samsung.com/global/microsite/galaxys4>.
- [6] “Samsung Galaxy S4,” <http://www.samsung.com/global/microsite/galaxys5>.
- [7] “Apple MacBook Air,” <http://www.apple.com/macbook-air/>.
- [8] “Apple MacBook Air,” <http://www.apple.com/macbook-pro/>.
- [9] “HTC One,” <http://www.htc.com/www/smartphones/htc-one/>.
- [10] “Asus RT-AC66U Wireless Router,” <https://www.asus.com/Networking/RTAC66U>.
- [11] “Asus PCE-AC66,” <https://www.asus.com/Networking/PCEAC66>.
- [12] “WLE900V5-18 NIC,” <http://www.compex.com.sg/productdetailinfo.asp?model=WLE900V5-18&acc1Panel=1>.
- [13] “Monsoon Power Monitor,” <http://www.msoon.com/LabEquipment/PowerMonitor/>.
- [14] A. Garcia-Saavedra, P. Serrano, A. Banchs, and G. Bianchi, “Energy consumption anatomy of 802.11 devices and its implication on modeling and design,” in *Proceedings of ACM CoNEXT*, 2012, pp. 169–180.
- [15] D. Halperin, B. Greenstein, A. Sheth, and D. Wetherall, “Demystifying 802.11n power consumption,” in *Proceedings of HotPower’10*.
- [16] I. Pefkianakis, Y. Hu, S. H. Wong, H. Yang, and S. Lu, “Mimo rate adaptation in 802.11 n wireless networks,” in *Proceedings of ACM Mobicom*, 2010, pp. 257–268.
- [17] A. Gudipati and S. Katti, “Strider: Automatic rate adaptation and collision handling,” in *ACM SIGCOMM*, vol. 41, no. 4, 2011, pp. 158–169.
- [18] M. Vutukuru, H. Balakrishnan, and K. Jamieson, “Cross-layer wireless bit rate adaptation,” in *ACM SIGCOMM*, vol. 39, no. 4, 2009, pp. 3–14.
- [19] S. H. Wong, H. Yang, S. Lu, and V. Bharghavan, “Robust rate adaptation for 802.11 wireless networks,” in *Proceedings of ACM Mobicom*, 2006, pp. 146–157.

- [20] C.-Y. Li, C. Peng, S. Lu, and X. Wang, “Energy-based rate adaptation for 802.11 n,” in *Proceedings of ACM Mobicom*, 2012, pp. 341–352.
- [21] M. O. Khan, V. Dave, Y.-C. Chen, O. Jensen, L. Qiu, A. Bhartia, and S. Rallapalli, “Model-driven energy-aware rate adaptation,” in *Proceedings of ACM MobiHoc*, 2013, pp. 217–226.
- [22] Y. Xiao, “Ieee 802.11 n: enhancements for higher throughput in wireless lans,” *IEEE Wireless Communications*, vol. 12, no. 6, pp. 82–91, 2005.
- [23] T. Paul and T. Ogunfunmi, “Wireless lan comes of age: Understanding the ieee 802.11 n amendment,” *IEEE Circuits and Systems Magazine*, vol. 8, no. 1, pp. 28–54, 2008.
- [24] D. Skordoulis, Q. Ni, H.-H. Chen, A. P. Stephens, C. Liu, and A. Jamalipour, “Ieee 802.11 n mac frame aggregation mechanisms for next-generation high-throughput wlans,” *IEEE Wireless Communications*, vol. 15, no. 1, pp. 40–47, 2008.
- [25] V. Shrivastava, S. Rayanchu, J. Yoonj, and S. Banerjee, “802.11 n under the microscope,” in *Proceedings of ACM IMC*, 2008, pp. 105–110.
- [26] K. Pelechrinis, T. Salonidis, H. Lundgren, and N. Vaidya, “Experimental characterization of 802.11 n link quality at high rates,” in *Proceedings of ACM WiNTech*, 2010, pp. 39–46.
- [27] L. Kriara, M. K. Marina, and A. Farshad, “Characterization of 802.11 n wireless lan performance via testbed measurements and statistical analysis.”
- [28] Y. Wang, M. A. Beydoun, L. Liang, B. Caballero, and S. K. Kumanyika, “Will all americans become overweight or obese? estimating the progression and cost of the us obesity epidemic,” *Obesity*, vol. 16, no. 10, pp. 2323–2330, 2008.
- [29] N. Khanna, C. J. Boushey, D. Kerr, M. Okos, D. S. Ebert, and E. J. Delp, “An overview of the technology assisted dietary assessment project at purdue university,” in *IEEE International Symposium on Multimedia (ISM)*,. IEEE, 2010, pp. 290–295.
- [30] H. C. Pinnington, P. Wong, J. Tay, D. Green, and B. Dawson, “The level of accuracy and agreement in measures of feo<sub>2</sub>, {FECO<sub>2</sub>} and v̄l̄Ge between the cosmed {K4b2} portable, respiratory gas analysis system and a metabolic cart,” *Journal of Science and Medicine in Sport*, vol. 4, no. 3, pp. 324 – 335, 2001. [Online]. Available: <http://www.sciencedirect.com/science/article/pii/S1440244001800414>
- [31] E. Munguia Tapia, “Using machine learning for real-time activity recognition and estimation of energy expenditure,” Ph.D. dissertation, Massachusetts Institute of Technology, 2008.
- [32] K. L. Dannecker, S. A. Petro, E. L. Melanson, and R. C. Browning, “Accuracy of fitbit activity monitor to predict energy expenditure with and without classification of activities,” *Medicine & Science in Sports & Exercise*, vol. 43, no. 5, p. 62, 2011.
- [33] S. Bosch, M. Marin-Perianu, R. Marin-Perianu, P. Havinga, and H. Hermens, “Keep on moving! activity monitoring and stimulation using wireless sensor networks,” in *Smart Sensing and Context*. Springer, 2009, pp. 11–23.

- [34] M. Altini, J. Penders, and O. Amft, “Energy expenditure estimation using wearable sensors: A new methodology for activity-specific models,” in *ACM Wireless Health*, 2012.
- [35] P. Yan, I. Lin, M. Roy, E. Seto, C. Wang, and R. Bajcsy, “Wave and calfitâ„¢towards social interaction in mobile body sensor networks,” in *The 5th Annual ICST Wireless Internet Conference (WICON)*. IEEE, 2010, pp. 1–2.
- [36] K. Y. Chen and M. Sun, “Improving energy expenditure estimation by using a triaxial accelerometer,” *Journal of applied Physiology*, vol. 83, no. 6, pp. 2112–2122, 1997.
- [37] A. Zhan, M. Chang, Y. Chen, and A. Terzis, “Accurate caloric expenditure of bicyclists using cellphones,” in *Proceedings of the 10th ACM Conference on Embedded Network Sensor Systems*, ser. SenSys ’12. New York, NY, USA: ACM, 2012, pp. 71–84. [Online]. Available: <http://doi.acm.org/10.1145/2426656.2426664>
- [38] Y. Ohtaki, M. Susumago, A. Suzuki, K. Sagawa, R. Nagatomi, and H. Inooka, “Automatic classification of ambulatory movements and evaluation of energy consumptions utilizing accelerometers and a barometer,” *Microsystem technologies*, vol. 11, no. 8-10, pp. 1034–1040, 2005.
- [39] J. Yin, Q. Yang, and J. J. Pan, “Sensor-based abnormal human-activity detection,” *IEEE Transactions on Knowledge and Data Engineering*, vol. 20, no. 8, pp. 1082–1090, 2008.
- [40] C. V. Bouten, K. T. Koekkoek, M. Verduin, R. Kodde, and J. D. Janssen, “A triaxial accelerometer and portable data processing unit for the assessment of daily physical activity,” *Biomedical Engineering, IEEE Transactions on*, vol. 44, no. 3, pp. 136–147, 1997.
- [41] P. S. Freedson, E. Melanson, J. Sirard *et al.*, “Calibration of the computer science and applications, inc. accelerometer.” *Medicine & science in sports & exercise*, vol. 30, no. 5, p. 777, 1998.
- [42] Y. Jang, M. Jung, J. Kang, and H. C. Kim, “An wearable energy expenditure analysis system based on the 15-channel whole-body segment acceleration measurement,” in *27th Annual International Conference of the Engineering in Medicine and Biology Society*. IEEE, 2005, pp. 3834–3836.
- [43] M. Sun, G. Reed, and J. Hill, “Modification of a whole room indirect calorimeter for measurement of rapid changes in energy expenditure,” *Journal of Applied Physiology*, vol. 76, no. 6, pp. 2686–2691, 1994.
- [44] J. McLaughlin, G. King, E. Howley, D. Bassett Jr, and B. Ainsworth, “Validation of the cosmed k4 b2 portable metabolic system,” *International Journal of Sports Medicine*, vol. 22, no. 04, pp. 280–284, 2001.
- [45] K. Gopalakrishnan, A. Agrawal, H. Ceylan, S. Kim, and A. Choudhary, “Knowledge discovery and data mining in pavement inverse analysis,” *Transport*, vol. 28, no. 1, pp. 1–10, 2013.
- [46] A. Agrawal, S. Misra, R. Narayanan, L. Polepeddi, and A. Choudhary, “Lung cancer survival prediction using ensemble data mining on seer data,” *Scientific Programming*, vol. 20, no. 1, pp. 29–42, 2012.
- [47] M. Hagan, H. Demuth, M. Beale *et al.*, *Neural network design*. Thomson Learning Stamford, CT, 1996.

- [48] M. Hall, E. Frank, G. Holmes, B. Pfahringer, P. Reutemann, and I. H. Witten, “The weka data mining software: an update,” *ACM SIGKDD Explorations Newsletter*, vol. 11, no. 1, pp. 10–18, 2009.
- [49] M. Youssef, M. Mah, and A. Agrawala, “Challenges: device-free passive localization for wireless environments,” in *Proceedings of ACM Mobicom*, 2007.
- [50] Y. Wang, J. Yang, Y. Chen, H. Liu, M. Gruteser, and R. P. Martin, “Tracking human queues using single-point signal monitoring,” in *Proceedings of ACM MobiSys*, 2014.
- [51] K. Wu, J. Xiao, Y. Yi, D. Chen, X. Luo, and L. M. Ni, “Csi-based indoor localization,” *IEEE Transactions on Parallel and Distributed Systems*, vol. 24, no. 7, pp. 1300–1309, 2013.
- [52] Z. Zhou, Z. Yang, C. Wu, L. Shangguan, and Y. Liu, “Towards omnidirectional passive human detection,” in *Proceedings IEEE INFOCOM*, 2013.
- [53] J. Xiao, K. Wu, Y. Yi, L. Wang, and L. M. Ni, “Fimd: Fine-grained device-free motion detection.” in *Proceedings of IEEE ICPADS*, 2012.
- [54] Q. Pu, S. Gupta, S. Gollakota, and S. Patel, “Whole-home gesture recognition using wireless signals,” in *Proceedings of ACM Mobicom*, 2013.
- [55] D. Halperin, W. Hu, A. Sheth, and D. Wetherall, “Tool release: Gathering 802.11n traces with channel state information,” *ACM SIGCOMM CCR*, vol. 41, no. 1, p. 53, Jan. 2011.
- [56] <http://www.shimmersensing.com>.
- [57] S. Rallapalli, A. Ganesan, K. Chintalapudi, V. N. Padmanabhan, and L. Qiu, “Enabling physical analytics in retail stores using smart glasses,” in *ACM MobiCom*, 2014.
- [58] S. Sen, D. Chakraborty, V. Subbaraju, D. Banerjee, A. Misra, N. Banerjee, and S. Mittal, “Accommodating user diversity for in-store shopping behavior recognition,” in *ACM ISWC*, 2014.
- [59] K. Chintalapudi, A. Padmanabha Iyer, and V. N. Padmanabhan, “Indoor localization without the pain,” in *ACM MobiCom*, 2010.
- [60] Z. Yang, C. Wu, and Y. Liu, “Locating in fingerprint space: wireless indoor localization with little human intervention,” in *ACM MobiCom*, 2012.
- [61] S. Sen, J. Lee, K.-H. Kim, and P. Congdon, “Avoiding multipath to revive inbuilding wifi localization,” in *ACM MobiSys*, 2013.
- [62] P. Hu, L. Li, C. Peng, G. Shen, and F. Zhao, “Pharos: Enable physical analytics through visible light based indoor localization,” in *ACM Hotnets*, 2013.
- [63] E. Munguia Tapia, “Using machine learning for real-time activity recognition and estimation of energy expenditure,” Ph.D. dissertation, Massachusetts Institute of Technology, 2008.
- [64] Y. Zeng, P. H. Pathak, C. Xu, and P. Mohapatra, “Your ap knows how you move: fine-grained device motion recognition through wifi,” in *ACM HotWireless*, 2014.

- [65] P. Melgarejo, X. Zhang, P. Ramanathan, and D. Chu, “Leveraging directional antenna capabilities for fine-grained gesture recognition,” in *ACM Ubicomp*, 2014.
- [66] Y. Wang, J. Liu, Y. Chen, M. Gruteser, J. Yang, and H. Liu, “E-eyes: device-free location-oriented activity identification using fine-grained wifi signatures,” in *ACM MobiCom*, 2014.
- [67] G. Wang, Y. Zou, Z. Zhou, K. Wu, and L. M. Ni, “We can hear you with wi-fi!” in *ACM MobiCom*, 2014.
- [68] Y. Wang, J. Liu, Y. Chen, M. Gruteser, J. Yang, and H. Liu, “E-eyes: device-free location-oriented activity identification using fine-grained wifi signatures,” in *ACM MobiCom*, 2014.
- [69] F. Adib, Z. Kabelac, D. Katabi, and R. C. Miller, “3d tracking via body radio reflections,” in *Usenix NSDI*, 2014.
- [70] Q. Pu, S. Gupta, S. Gollakota, and S. Patel, “Whole-home gesture recognition using wireless signals,” in *ACM MobiCom*, 2013.
- [71] J. Unar, W. C. Seng, and A. Abbasi, “A review of biometric technology along with trends and prospects,” *Pattern recognition*, vol. 47, no. 8, pp. 2673–2688, 2014.
- [72] T. T. Ngo, Y. Makihara, H. Nagahara, Y. Mukaigawa, and Y. Yagi, “The largest inertial sensor-based gait database and performance evaluation of gait-based personal authentication,” *Pattern Recognition*, vol. 47, no. 1, pp. 228–237, 2014.
- [73] F. Adib and D. Katabi, “See through walls with wi-fi!” 2013.
- [74] P. Melgarejo, X. Zhang, P. Ramanathan, and D. Chu, “Leveraging directional antenna capabilities for fine-grained gesture recognition,” in *ACM UbiComp*, 2014.
- [75] W. Xi, J. Zhao, X.-Y. Li, K. Zhao, S. Tang, X. Liu, and Z. Jiang, “Electronic frog eye: Counting crowd using wifi,” in *IEEE INFOCOM*, 2014.
- [76] Y. Wang, J. Yang, Y. Chen, H. Liu, M. Gruteser, and R. P. Martin, “Tracking human queues using single-point signal monitoring,” in *ACM MobiSys*, 2014.
- [77] C. Han, K. Wu, Y. Wang, and L. M. Ni, “Wifall: Device-free fall detection by wireless networks,” in *IEEE INFOCOM*, 2014.
- [78] X. Liu, J. Cao, S. Tang, and J. Wen, “Wi-sleep: Contactless sleep monitoring via wifi signals,” in *IEEE RTSS*, 2014.
- [79] T. Teixeira, D. Jung, G. Dublon, and A. Savvides, “Pem-id: Identifying people by gait-matching using cameras and wearable accelerometers,” in *IEEE ICDSC*, 2009.
- [80] I. Bouchrika, M. Goffredo, J. Carter, and M. Nixon, “On using gait in forensic biometrics,” *Journal of forensic sciences*, vol. 56, no. 4, pp. 882–889, 2011.
- [81] J. Jenkins and C. Ellis, “Using ground reaction forces from gait analysis: body mass as a weak biometric,” in *Pervasive Computing*. Springer, 2007, pp. 251–267.

- [82] S. Mondal, A. Nandy, P. Chakraborty, and G. Nandi, “Gait based personal identification system using rotation sensor,” *Journal of Emerging Trends in Computing and Information Sciences*, vol. 3, no. 2, pp. 395–402, 2012.
- [83] Y. Ren, Y. Chen, M. C. Chuah, and J. Yang, “Smartphone based user verification leveraging gait recognition for mobile healthcare systems,” in *IEEE SECON*, 2013.
- [84] Y. Zhang, G. Pan, K. Jia, M. Lu, Y. Wang, and Z. Wu, “Accelerometer-based gait recognition by sparse representation of signature points with clusters.” *IEEE trans. on cybernetics*, 2014.
- [85] D. Gafurov, K. Helkala, and T. Søndrol, “Biometric gait authentication using accelerometer sensor,” *Journal of computers*, vol. 1, no. 7, pp. 51–59, 2006.
- [86] S. Pan, N. Wang, Y. Qian, I. Velibeyoglu, H. Y. Noh, and P. Zhang, “Indoor person identification through footstep induced structural vibration,” in *ACM HotMobile*, 2015.
- [87] S. Bamberg, A. Benbasat, D. Scarborough, D. Krebs, and J. Paradiso, “Gait analysis using a shoe-integrated wireless sensor system,” *IEEE Trans. on Information Technology in Biomedicine*, vol. 12, no. 4, pp. 413–423, July 2008.
- [88] Y. Jin, W.-S. Soh, and W.-C. Wong, “Indoor localization with channel impulse response based fingerprint and nonparametric regression,” *IEEE Trans. on Wireless Communications*, vol. 9, no. 3, pp. 1120–1127, March 2010.
- [89] N. Ravi, N. Dandekar, P. Mysore, and M. L. Littman, “Activity recognition from accelerometer data,” in *AAAI*, vol. 5, 2005, pp. 1541–1546.
- [90] R. Schneider, “Survey of peaks/valleys identification in time series,” 2011.
- [91] C. BenAbdelkader, R. Cutler, and L. Davis, “Stride and cadence as a biometric in automatic person identification and verification,” in *IEEE FG2002*.
- [92] C. Lukaszewski, “Very high-density 802.11ac networks, planning guide,” in *White Paper, Aruba Networks*, 2014.
- [93] “Virtual cells: The only scalable multi-channel deployment,” in *Meru Networks White Paper*, 2005.
- [94] M. X. Gong, B. Hart, and S. Mao, “Advanced Wireless LAN Technologies: IEEE 802.11ac and Beyond,” in *ACM GetMobile: Mobile Comp. and Comm.*, 2015.
- [95] “Ericsson 5G field trial gear achieves peak downlink throughput over 25 Gbps with MU-MIMO,” in *Ericsson press release*, 2016.
- [96] “Clientmatch technology: Wi-fi client optimization,” in *Aruba Networks White Paper*, 2015.
- [97] S.-w. Han and M. Ram, “Distributed client steering algorithm to a best-serving access point,” in *USA Patent, US9078198, Meru Networks*, 2015.
- [98] Y. Zhu, Q. Ma, C. Bisikian, and C. Ying, “A user-centric network management framework for high-density wireless lans,” in *IFIP/IEEE IM’09*.

- [99] R. Murty, J. Padhye, R. Chandra, A. Wolman, and B. Zill, “Designing high performance enterprise wi-fi networks.” in *USENIX NSDI’08*.
- [100] S. Sur, I. Pefkianakis, Z. Xinyu, and K.-H. Kim, “Practical mu-mimo user selection on 802.11ac commodity networks,” in *ACM MobiCom’16*.
- [101] H. Yu, O. Bejarano, and L. Zhong, “Combating inter-cell interference in 802.11ac-based multi-user mimo networks,” in *ACM MobiCom’14*.
- [102] W.-L. Shen, K. C.-J. Lin, M.-S. Chen, and T. Kun, “SIEVE: Scalable User Grouping for Large MU-MIMO Systems,” in *IEEE INFOCOM’15*.
- [103] IEEE Standards Association, “IEEE Standards 802.11ac-2013: Enhancements for Very High Throughput for Operation in Bands below 6 GHz,” 2013.
- [104] Y. Zeng, P. H. Pathak, and P. Mohapatra, “A first look at 802.11 ac in action: Energy efficiency and interference characterization,” in *IFIP Networking’14*.
- [105] R. Jain, D.-M. Chiu, and W. R. Hawe, *A quantitative measure of fairness and discrimination for resource allocation in shared computer system*. DEC TR, 1984.
- [106] C. Shepard, H. Yu, N. Anand, E. Li, T. Marzetta, R. Yang, and L. Zhong, “Argos: Practical many-antenna base stations,” in *ACM MobiCom’12*.
- [107] W. Wang, A. X. Liu, M. Shahzad, K. Ling, and S. Lu, “Understanding and modeling of wifi signal based human activity recognition,” in *ACM MobiCom’15*.
- [108] W. S. Cleveland, “Robust locally weighted regression and smoothing scatterplots,” in *Journal of the ASA*, vol. 74, no. 368, 1979, pp. 829–836.
- [109] D. Halperin, W. Hu, A. Sheth, and D. Wetherall, “Predictable 802.11 packet delivery from wireless channel measurements,” in *ACM SIGCOMM’10*.
- [110] Y. Zeng, I. Pefkianakis, K.-H. Kim, and P. Mohapatra, “Maps: Mu-mimo-aware ap selection for 802.11ac networks,” in <http://spirit.cs.ucdavis.edu/pubs/tr/MAPS-TR.pdf>.
- [111] I. Pefkianakis and et al., “Characterizing home wireless performance: The gateway view,” in *IEEE INFOCOM’15*.
- [112] Microsoft, “Media quality and network connectivity performance in skype for business online,” in <https://support.office.com>.
- [113] H. Lee, S. Kim, O. Lee, S. Choi, and S.-J. Lee, “Available bandwidth-based association in ieee 802.11 wireless lans,” in *ACM MSWiM’08*.
- [114] S. Xu, F. Ren, Y. Xu, C. Lin, and M. Yao, “Selecting a preferable access point with more available bandwidth,” in *IEEE ICC’13*.
- [115] T. Iwami, Y. Takaki, K. Yamori, C. Ohta, and H. Tamaki, “Distributed association control considering user utility and user guidance in ieee 802. 11 networks,” in *IEEE PIMRC’13*.

- [116] Y.-C. Hsu, K. C.-J. Lin, and W.-T. Chen, “Client-ap association for multiuser mimo networks,” in *IEEE ICC’15*.
- [117] X. Xie and X. Zhang, “Scalable user selection for MU-MIMO networks,” in *IEEE INFOCOM’14*.
- [118] G. Zois, A. Michaloliakos, K. Psounis, V. Vassalos, and I. Mourtos, “Non-asymptotic performance bounds for downlink mu-mimo scheduling,” in *IEEE/IFIP WONS’16*.
- [119] K. C.-J. Lin, S. Gollakota, and D. Katabi, “Random access heterogeneous mimo networks,” in *ACM SIGCOMM’11*.
- [120] H. V. Balan, R. Rogalin, A. Michaloliakos, K. Psounis, and G. Caire, “Achieving high data rates in a distributed mimo system,” in *ACM MobiCom’12*.
- [121] X. Xie, X. Zhang, and E. Chai, “Cross-cell dof distribution: Combating channel hardening effect in multi-cell mu-mimo networks,” in *ACM MobiHoc’15*.
- [122] J. Liu, Y. Wang, Y. Chen, J. Yang, X. Chen, and J. Cheng, “Tracking vital signs during sleep leveraging off-the-shelf wifi,” in *MobiHoc ’15*.
- [123] N. Patwari, L. Brewer, Q. Tate, O. Kaltiokallio, and M. Bocca, “Breathfinding: A wireless network that monitors and locates breathing in a home,” *Selected Topics in Signal Proc., IEEE Journal of*, 2014.
- [124] H. Abdelnasser, K. A. Harras, and M. Youssef, “Ubibreathe: A ubiquitous non-invasive wifi-based breathing estimator,” in *MobiHoc ’15*.
- [125] R. Ravichandran, E. Saba11, K.-Y. Chen, M. Goel, S. Gupta, and S. N. Patel, “WiBreathe: Estimating Respiration Rate Using Wireless Signals in Natural Settings in the Home,” in *Percom*. IEEE, 2015.
- [126] IEEE P802.11adTM/D4.0, “Part 11: Wireless lan medium access control (mac) and physical layer (phy) specifications amendment 3: Enhancements for very high throughput in 60 ghz,” *IEEE Computer Society*.
- [127] Q. Incorporated. Joint 802.11ac and 802.11ad chipset. [Online]. Available: <http://www.qualcomm.com/media/releases/2013/01/08/qualcomm-and-wilocity-launch-industrys-first-tri-band-reference-design>
- [128] T. Wei and X. Zhang, “mtrack: High-precision passive tracking using millimeter wave radios,” in *ACM Mobicom*, 2015.
- [129] F. Adib, H. Mao, Z. Kabelac, D. Katabi, and R. C. Miller, “Smart homes that monitor breathing and heart rate,” in *CHI*. ACM, 2015.
- [130] D. T. Petkie, C. Benton, and E. Bryan, “Millimeter-wave radar for vital signs sensing.” International Society for Optics and Photonics, 2009.
- [131] I. V. Mikhelson, P. Lee, S. Bakhtiari, T. W. Elmer, A. K. Katsaggelos, and A. V. Sahakian, “Non-contact millimeter-wave real-time detection and tracking of heart rate on an ambulatory subject,” *Information Technology in Biomedicine, IEEE Transactions on*, 2012.

- [132] S. Bakhtiari, T. Elmer, N. Cox, N. Gopalsami, A. Raptis, S. Liao, I. Mikhelson, and A. Sahakian, “Compact Millimeter-Wave Sensor for Remote Monitoring of Vital Signs,” *Instrumentation and Measurement, IEEE Transactions on*, vol. 61, no. 3, pp. 830–841, March 2012.
- [133] T.-Y. J. Kao and J. Lin, “Vital sign detection using 60-GHz Doppler radar system,” in *Wireless Symposium (IWS), 2013 IEEE International*. IEEE, 2013, pp. 1–4.
- [134] H.-R. Chuang, H.-C. Kuo, F.-L. Lin, T.-H. Huang, C.-S. Kuo, and Y.-W. Ou, “60-GHz millimeter-wave life detection system (MLDS) for noncontact human vital-signal monitoring,” *Sensors Journal, IEEE*, vol. 12, no. 3, pp. 602–609, 2012.
- [135] Y. Zeng, P. H. Pathak, Z. Yang, and P. Mohapatra, “Human tracking and activity monitoring using 60 ghz mmwave,” in *2016 15th ACM/IEEE International Conference on Information Processing in Sensor Networks (IPSN)*. IEEE, 2016, pp. 1–2.
- [136] T. Wei and X. Zhang, “mtrack: High-precision passive tracking using millimeter wave radios,” in *MobiCom ’15*. New York, NY, USA: ACM.
- [137] B. Langen, G. Lober, and W. Herzig, “Reflection and transmission behaviour of building materials at 60 ghz,” in *PIMRC*. IEEE, 1994.
- [138] S. Sur, V. Venkateswaran, X. Zhang, and P. Ramanathan, “60 ghz indoor networking through flexible beams: A link-level profiling,” in *Sigmetrics ’15*. ACM.
- [139] Y. Zhu, Z. Zhang, Z. Marzi, C. Nelson, U. Madhow, B. Zhao, and H. Zheng, “Demystifying 60ghz outdoor picocells,” in *MobiCom ’14*.
- [140] X. Zhou, Z. Zhang, Y. Zhu, Y. Li, S. Kumar, A. Vahdat, B. Y. Zhao, and H. Zheng, “Mirror mirror on the ceiling: Flexible wireless links for data centers,” in *ACM SIGCOMM ’12*.
- [141] T. Nitsche, A. B. Flores, E. W. Knightly, and J. Widmer, “Steering with eyes closed: mm-wave beam steering without in-band measurement,” in *IEEE INFOCOM 2015*.
- [142] Z. Yang, P. H. Pathak, Y. Zeng, and P. Mohapatra, “Sensor-assisted codebook-based beamforming for mobility management in 60 ghz wlans,” in *Mobile Ad Hoc and Sensor Systems (MASS), 2015 IEEE 12th International Conference on*, Oct 2015, pp. 333–341.
- [143] Pasternack. Pasternack. [Online]. Available: <http://www.pasternack.com/60-ghz-test-development-system-pem003-kit-p.aspx>
- [144] E. M. Tapia, “Using machine learning for real-time activity recognition and estimation of energy expenditure,” Ph.D. dissertation, MIT, 2008.
- [145] W. F. Ganong and K. E. Barrett, *Review of medical physiology*. McGraw-Hill Medical ^ eNew York New York, 2005, vol. 21.
- [146] J. Ahmadi-Shokouh, S. Noghanian, E. Hossain, M. Ostadrahimi, and J. Dietrich, “Reflection coefficient measurement for house flooring materials at 57-64 ghz,” in *IEEE GLOBECOM 2009*.
- [147] S. Gabriel, R. Lau, and C. Gabriel, “The dielectric properties of biological tissues: II. measurements in the frequency range 10 hz to 20 ghz,” *Physics in medicine and biology*, vol. 41, 1996.

- [148] O. P. Gandhi and A. Riazi, "Absorption of millimeter waves by human beings and its biological implications," *Microwave Theory and Techniques, IEEE Transactions on*, vol. 34, no. 2, pp. 228–235, 1986.
- [149] H. Hwang, J. Yim, J.-W. Cho, C. Cheon, and Y. Kwon, "110 ghz broadband measurement of permittivity on human epidermis using 1 mm coaxial probe," in *Microwave Symposium Digest, 2003*. IEEE.
- [150] M. Zhadobov, N. Chahat, R. Sauleau, C. Le Quement, and Y. Le Drean, "Millimeter-wave interactions with the human body: state of knowledge and recent advances," *Inter. Journal of Microwave Technologies*, 2011.
- [151] BMI and Respiratory Function. [Online]. Available: <http://www.livestrong.com/article/84685-bmi-respiratory-function/>
- [152] NeuLog Sensors. [Online]. Available: <https://neulog.com/>
- [153] Gurin. Finger Pulse Oximeters. [Online]. Available: <http://gurinproducts.com/products/oximeters/>